Svein-Erik Måsøy

Estimation and correction of aberration in medical ultrasound imaging

Doktor ingeniør thesis

Department of Engineering Cybernetics
Norwegian University of Science and Technology
Trondheim
Norway

ISBN 82-471-6544-9 (printed version)
ISBN 82-471-6543-0 (electronic version)

Abstract

The work presented in this thesis is devoted to studying aberration in ultrasound medical imaging, and to provide methods for correcting aberration of ultrasound signals in order to obtain optimum image quality. The thesis is composed of five chapters. All chapters may be read individually. The presented results are generated from simulations.

Chapter 1 presents a description of the aberration phenomenon, and a brief discussion of its medical and practical implications. A mathematical description of aberration is introduced by modelling the Green's function for propagation in a heterogeneous medium.

In Ch. 2, aberration from a point scatterer in the focus of an array is studied. Aberration is generated by two body wall models, generating weak and strong aberration, emulating the human abdominal wall. The results show that if correctly estimated, aberration can be close to ideally characterized by arrival time and amplitude fluctuations measured across the receive array. Using the arrival time and amplitude fluctuations in a time-delay and amplitude transmit aberration correction filter, produce close to ideal correction of the retransmitted beam. A point source represents a situation which is rarely found in medical ultrasound imaging.

A method for estimating aberration from random scatterers is developed in Ch. 3. The method is based on a cross-correlation analysis, and may in general estimate aberration at each frequency component of the received ultrasound signal. Due to the results from Ch. 2, the method is only investigated for a time-delay and amplitude estimate at the center frequency of the signal. The same aberrators as in Ch. 2 are used. The results show that the method does not produce satisfactory estimates of the arrival time and amplitude fluctuations for both aberrators.

The backscatter in ultrasound imaging is determined by the width of the focused transmit beam used to obtain the image. Aberration widens the transmit beam, and the back-scattering region may become quite large. Since the human body wall has a certain thickness, the body wall itself generates interference of the signals propagating from different scatterers to the array. This smoothens aberration parameters such as arrival time and amplitude fluctuations, making proper estimation of these unfeasible.

Aberration correction is performed as a filter process prior to transmit of the ultrasound beam. This means that aberration estimation/correction methods model aberration as a filter, that is, all effects of aberration are assumed to be fully described in an infinitely thin layer at the array surface. For a point source, this assumption is fulfilled since the signal received on different array elements originates from the same spatial point. For a large scattering region this is generally not true, and the aberration described on a specific array element is dependent of the sum of aberrations generated along different propagation paths from each contributing scatterer. It is then impossible to obtain ideal aberration correction for a specific point in space (usually the focus of the array).

A solution to this problem may be sought by iteration of transmit-beam aberration correction (transmit-beam iteration). Transmit-beam iteration is described as a process where an uncorrected transmit-beam is used for an initial estimate of aberration parameters. A new beam with correction is then transmitted, generating a new estimate of the parameters. This process is repeated until some convergence criterion is met. The goal of this process is to reduce the width of the transmit beam, in order for the aberration on a specific receive element to be independent of the scatterers spatial position.

Transmit-beam iteration is studied in Ch. 4. Now, eight different aberrators are used, all

emulating the human abdominal wall. Here, the estimator developed in Ch. 3 is compared with a similar type of estimator. New insight into the equalities and differences between the estimation methods are provided through transmit-beam iteration considerations. The results show that using a time-delay and amplitude aberration correction filter, both algorithms provide close to ideal aberration correction after two to three transmit-beam iterations for all aberrators. In addition, an earlier developed focus criterion proves to give accurate description of the point of convergence, and the accuracy of the correction.

The aberration estimation method described in Ch. 3, was developed in the frequency domain. In Ch. 5, a time domain implementation is introduced. Necessary assumptions made in the time domain implementation makes the algorithm different from the frequency domain implementation.

Since the receive signal in ultrasound imaging is a stochastic variable, estimation of arrival time-delays and amplitudes at the array, is connected with uncertainty. A variance analysis of both the time and frequency domain implementations is performed.

There exists only minor differences between the two implementations with respect to variance. The variance in the estimates proved to be highly dependent upon the aberrator. Results also indicate that a transmit-beam iteration process converges, even if the variance in the initial estimate for the iteration process is very high.

In appendix A, a brief discussion of aberration as a function of frequency is provided.

Preface

This thesis is submitted in partial fulfillment of the requirements for the degree "Doktor Ingeniør" at the Norwegian University of Science and Technology (NTNU).

The work was carried out at the Department of Circulation and Imaging at the Faculty of Medicine, and was supervised by Professor Bjørn A. Angelsen. Formally, I was affiliated to the Department of Engineering Cybernetics.

The research was funded by the Research Council of Norway (NFR).

Acknowledgments

Many people have contributed to this thesis in some way or another. First of all, I am very grateful for the guidance provided by Professor Angelsen. He has always been very interested and involved in my work. In periods of doubt and despair, he has encouraged me, and above all believed in me. These are important qualities for a supervisor, and gave me the spirit to continue and finish my work.

I am also very thankful for having had the opportunity to work with my colleague Trond Varslot. His involvement in the project greatly improved my work, and our co-operation has turned out to be very fruitful. He is also a good friend, and has been my travel companion to several conferences.

Tonni F. Johansen took care of me when I started to work with ultrasound. I have a background in fluid mechanics and did really not know anything about imaging, signal processing or acoustics. He taught me all the basics, and has remained a reference and mentor throughout the remainder of my thesis work.

I have shared office with Rune Hansen. We have had many discussions about basic theory which has been really clarifying, at least from my point of view. He has also suffered from my frustration outburst and complaints whenever I had *e.g.* computer problems etc. His patience is unmatched as far as I have experienced.

Finally I have to thank the rest of the research group at the department. Together we have formed an interesting team. Also I need to thank all my stipendiat colleagues, students and department employees who have provided a warm and friendly working environment.

Trondheim, October 2004
Svein-Erik Måsøy

Contents

1 Introduction **9**
- I Soft tissue factors determining image quality in ultrasound imaging . . . 10
- II Examples of aberration . . . 11
- III Clinical aspects of aberration correction . . . 12
  - III.A Diagnosis of breast cancer . . . 13
  - III.B HIFU treatment of cancer . . . 13
- IV Practical aspects of aberration correction . . . 14
  - IV.A Ultrasound arrays . . . 14
  - IV.B Frequency . . . 15
  - IV.C Computational requirements . . . 15
- V Basic theory . . . 16
  - V.A The homogeneous wave equation and Green's function . . . 16
  - V.B The heterogeneous wave equation and Green's function . . . 17
  - V.C Modeling of the heterogeneous Green's function - the concept of the screen 20
  - V.D The receive signal model: Scatterer independent aberration . . . 21
  - V.E The Van Cittert-Zernike theorem . . . 23
  - V.F Aberration as a function of frequency . . . 23
- VI Assumptions for the work presented in this thesis . . . 23
- VII Overview of thesis . . . 24

2 Correction of ultrasonic wave aberration with a time-delay and amplitude filter **29**
- I Introduction . . . 29
- II Theory and method . . . 31
  - II.A Simulation setup . . . 31
  - II.B Body wall modelling . . . 31
  - II.C Linear angular spectrum propagation operator . . . 33
  - II.D Correction filters and the generalized frequency-dependent screen . . . 33
- III Simulation parameters and data processing . . . 34
- IV Results . . . 37
- V Discussion . . . 43
- VI Conclusions . . . 47

3 Estimation of ultrasound wave aberration with signals from random scatterers **51**
- I Introduction . . . 51
- II Theory . . . 53

II.A The generalized frequency-dependent screen and the time-delay and amplitude correction filter . . . 53
II.B Aberration estimation . . . 54
III Method . . . 58
III.A Modeling of aberration . . . 58
III.B Simulations . . . 58
IV Simulation parameters and data processing . . . 60
V Results . . . 61
VI Discussion . . . 68
VII Conclusions . . . 71

4 Iteration of transmit-beam aberration correction in medical ultrasound imaging 75
I Introduction . . . 75
II Theory . . . 77
II.A Signal and aberration correction modeling . . . 77
II.B Scatterer-independent aberration and the van Cittert-Zernike theorem . . 77
III Estimators . . . 78
IV Simulations . . . 83
IV.A Simulation parameters and data processing . . . 83
V Results . . . 85
VI Discussion . . . 88
VII Conclusion . . . 95

5 Variance analysis of arrival time and amplitude fluctuation estimates from random speckle signal 99
I Introduction . . . 99
II Theory . . . 102
II.A Time domain implementation of the MBFO algorithm . . . 102
II.B Comparison of frequency and time domain implementation . . . 105
III Simulations . . . 106
III.A Simulation parameters and data processing . . . 106
IV Results . . . 108
V Discussion . . . 112
VI Conclusions . . . 118

Appendix 122

A Aberration as a function of frequency 123

B The MBFO estimator in the frequency and time domain: A comparison 131

Chapter 1

Introduction

S. Måsøy
Department of Circulation and Imaging, NTNU.

Ultrasound imaging has been the largest growing medical imaging modality the last 15 years. Reasons for this are that many disorders can be diagnosed efficiently with ultrasound, the equipment has relatively low cost, and do not require special building adaptations. One can even see portable ultrasound imaging equipment being introduced in the market. Ultrasound imaging is also widely used for guidance of tissue biopsies and other minimally invasive procedures. However, ultrasound images are for many individuals severely degraded in quality due to the spatial variations of the acoustic propagation parameters in the tissue (spatial tissue heterogeneity). This phenomenon is called aberration, and reduces the clinical value of the images. The image degradation also limits the use of ultrasound for guidance of procedures. Hence, improving the image quality and resolution in the ultrasound images will greatly increase the clinical potential of ultrasound imaging in many applications. An example is screening of selected groups of the population for early detection of tumors. Early detection of cancers may increase the survival rate, and simple detection methods hence opens for screening of selected groups of the population with ultrasound imaging. The low cost and portability of ultrasound equipment makes such screening easier, compared to using more heavy and expensive X-ray and MR equipment.

The benefits of aberration correction may be summarized as follows:

- sharper images will be obtained over a wide group of patients, facilitating a more accurate diagnosis of diseases for all categories of patients and illnesses
- improved diagnosis of cancer tumors
- improved focusing quality of ultrasound minimally invasive surgery tools (High Intensity Focused Ultrasound - HIFU) for treatment of localized cancer tumors
- provide better detection of blood flow, improving contrast agent imaging methods as well as Doppler methods

Aim of thesis:
The work presented in this thesis is devoted to studying the aberration phenomenon, and to provide methods for correcting ultrasound signals in order to obtain optimum image quality.

I Soft tissue factors determining image quality in ultrasound imaging

The quality of the ultrasound image is described by the spatial resolution determined by the beam focusing, and the contrast resolution which is given by the side lobes in the beam. Soft tissue limits both the spatial and the contrast resolution that is obtained with current ultrasound imaging systems through the following three phenomena:

1. **Absorption** of ultrasound energy represents conversion of pressure waves to heat. For tissue, this effect increases with the ultrasound frequency, and limits the highest frequency f, and thereby the shortest wavelength $\lambda = c/f$ (c is the ultrasound propagation velocity), that can be used at a given depth. Assuming a rectangular aperture, the spatial resolution of ultrasound instruments is approximately $2\lambda F/D$. Here, F is the focal point of the array and D the array size. Aberration reduce the spatial resolution. By performing aberration correction the resolution can be improved. The wavelength can be reduced by improving the sensitivity so that higher ultrasound frequencies can be used. The sensitivity can be improved by increasing the aperture so that more of the scattered energy is collected, and also by reducing power losses in the ultrasound transducer and the signal transmission between the transducer and imaging instrument.

2. **Aberration** (also known as phasefront aberration) due to spatial variations in the ultrasound propagation velocity in tissue, destroys the focusing of the ultrasound beam and increases the sidelobe level. This leads to a reduction of both the spatial and contrast resolution, blurring the image. Aberration is mainly generated in the human body wall, which is composed of skin, fat, muscle and connective tissue. Typical velocities for tissue in the human body wall is 1448 m/s for fat, 1547 m/s for muscle, and 1613 m/s for skin and connective tissue.[1] These constitute the largest sound speed differences in the human body.

3. Strong spatial heterogeneity also creates acoustic noise through multiple scattering known as pulse **reverberations**. The reverberations produce a tail added to the propagating pulse, and is observed as additive noise in the image. This effect is strongest when imaging through the body wall, as this is composed of irregular mixtures of muscles, fat, and connective tissue. Note that the effect is also important with strongly heterogeneous objects like the breast and other fatty glands.

Aberration and reverberation may be viewed as acoustic noise or distortion introduced in the image by the inherent inhomogeneous structure of soft tissue. The absorption and acoustic noise effects are linked. The spatial heterogeneity limits the practical aperture in relation to the wavelength, as long as no corrections for the aberration are performed, and hence lowers sensitivity and the frequency. The effect of aberration also increases with frequency, because the propagation variations in the wave front is related to the wavelength of the transmitted signal. Pulse reverberations are currently reduced by using 2nd harmonic imaging, a method that has less sensitivity than 1st harmonic imaging, and hence requires use of lower imaging frequencies.

Efficient corrections of aberration and pulse reverberation improve the focusing of the ultrasound beam, hence improving both the spatial and contrast resolution. Further, aberration correction allow the use of larger apertures with improved sensitivity. Higher ultrasound frequencies may then be used, further improving the spatial resolution. There is therefore a large international research activity to study and provide methods for correction of aberration and pulse reverberations in medical ultrasound imaging.

Absorption and reverberations are *not* considered in the work presented here.

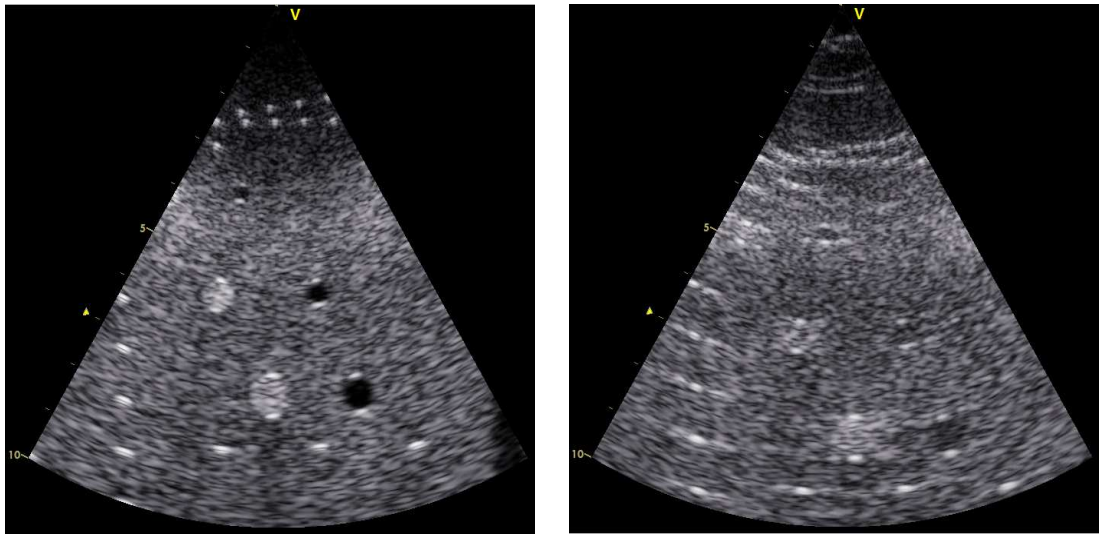

Figure 1.1: Ultrasound images of a tissue mimicking phantom. The left pane shows an image with no aberration. The right pane shows an image with phase aberration generated by a 5 mm thick silicon aberrator.

II Examples of aberration

Some examples of how aberration affects the ultrasound signal are provided here. The examples illustrate the possibilities for improvement by correcting aberration.

Ultrasound images of a tissue mimicking phantom containing objects of different sizes, are presented in Fig. 1.1. The phantom is imaged at 2.5 MHz, with a 2 cm cardiac probe focused at 7 cm. In the figure to the left, the phantom is imaged with no aberration of the signal. In the middle of the image, two anechoic regions of size 6 and 8 mm are visible together with two strong scattering regions (15 dB stronger than the background) of the same size. One millimeter sized point scatterers are also visible to the left, and below these regions.

The image to the right is of the same phantom, using a 5 mm thick silicon slab in front of the probe to generate aberration. The aberration is produced by slots which are milled out in the slab. Slots of different thickness across the array, generate propagation time-delay differences in the transmitted and received signals. The time-delays generated by the slab emulates the time-delay differences observed in the human abdominal wall.[2] Due to the thickness of the silicon slab, the objects in the phantom are not in the exact same location in the two images.

The aberrated image appears quite different compared to the unaberrated image. The contrast resolution is severely reduced, and it is difficult to observe the anechoic regions as well as the strong scattering regions. The strong point scatterers are smeared laterally, and the point scatterers visible in the near-field of the unaberrated image, are not visible in the aberrated image.

Figure 1.2 displays a grayscale image of an ultrasound beam as a function of range (depth), with and without aberration. The images are obtained from simulations using a 2 cm array with focus at 6 cm. The unaberrated beam has a well defined focal depth around the focus point. For the aberrated beam, the focal region is stretched in range, and the contrast resolution (determined by the sidelobe level) is strongly reduced.

Figure 1.3 display temporal grayscale pictures of the received waveforms from a point source

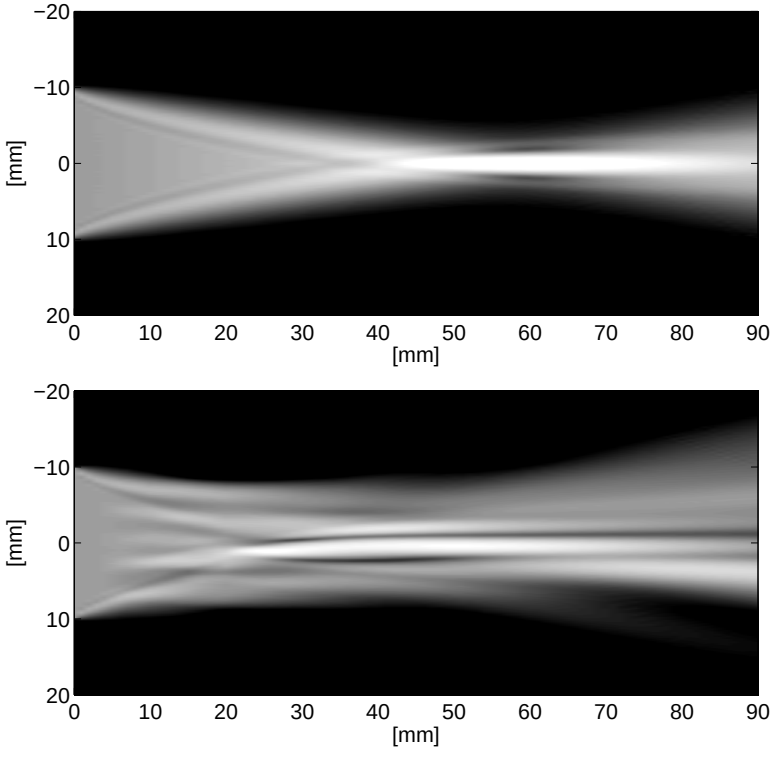

Figure 1.2: Beam profiles for a 2 cm ultrasound array with focus at range depth 6 cm. The vertical axis represents the array axis, and the horizontal axis represents range (depth). The top pane shows a beam with no aberration. The bottom pane shows a beam with aberration from a 2 cm thick body wall model, emulating the human abdominal wall. The center frequency of the pulse is 2.5 MHz. The images are plotted with a 20 dB dynamic scale.

in the focus of an array. Geometric focusing has been removed. The array size is 2 cm with a focus at 6 cm. A pulse with 2.5 MHz center frequency and 2.5 periods is used as the temporal signal. The left pane shows a signal without aberration, and the right pane shows a signal with aberration using the same aberrator as in Fig. 1.2. The phasefronts of the aberrated signal are distorted, and there also exists amplitude variations of close to 8 dB in the picture. These do not show properly since a dynamic scale of 40 dB is used. Beamforming in ultrasound imaging consists of summing the signals over the array to form a receive beam from a specific focusing direction. It is obvious from Fig. 1.3 that the receive beams from the unaberrated and aberrated signals will be very different.

III Clinical aspects of aberration correction

In this section, some clinical examples are presented where aberration correction can prove to become an important contribution for an improved diagnosis.

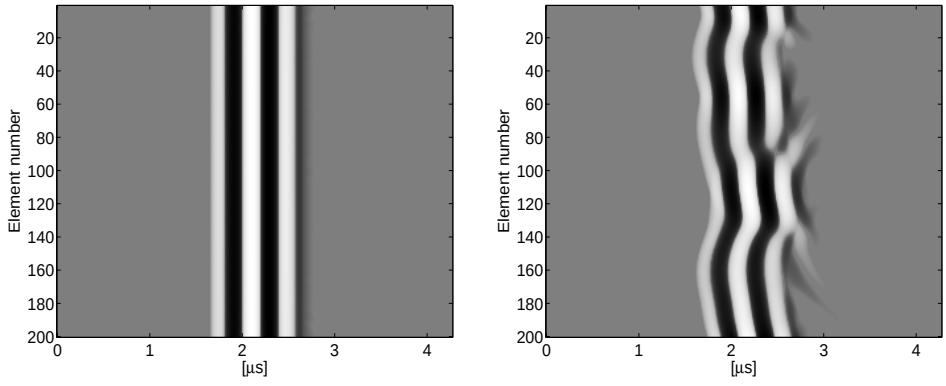

Figure 1.3: Receive signals from a point scatterer in the focus of an array. Geometric focusing is removed. The left pane shows a signal with no aberration. The right pane shows a signal with aberration from a 2 cm thick body wall model, emulating the human abdominal wall.

III.A Diagnosis of breast cancer

A very relevant example of the necessity of aberration correction methods, is screening of the female breast for tumors. The breast is a mixture of fat, glandular tissue, muscle tissue, and connective tissue and constitutes an object which is highly heterogeneous. Imaging of the breast is performed at relatively high frequencies (7-12 MHz) and is especially sensitive to aberration due to the short wavelength at these frequencies. In many western countries screening of the female population for breast cancer is normal, and in almost 40% of the cases of women between 40 and 50 years, a tumor is found.[3] When a tumor is detected from mammography screening, the follow-up investigation is often done by ultrasound imaging. Diagnosing a tumor as malignant or benign is associated with uncertainty, and leads to a number of unnecessary biopsies and surgical procedures. This means that a large portion of women who are treated for breast cancer today, may not need treatment because the diagnosed tumor will never develop to become malignant. In a recent study performed on the female population in Norway and Sweden, this portion is expected to be 30-50%.[4] Overcoming aberration problems in this situation could lead to a more certain diagnose of the malignancy of the tumor with ultrasound. It would also lead to a more precise definition of the biopsy hot-spot, improving the biopsy investigation and reducing the number of unnecessary surgical procedures and the trauma following diagnosed cancer. Different techniques could also be applied to improve the diagnosis, *e.g.* imaging of the vascularization of tumors using contrast agent.

III.B HIFU treatment of cancer

Ultrasound is not limited to imaging and diagnosis, but can also be used for treatment and non-invasive surgery. There is an intensive research activity going on in the field of High Intensity Focused Ultrasound (HIFU). When using ultrasound for imaging, a strong limit is set on the allowed intensity in order not to damage tissue. When increasing the intensity of the transmitted focused ultrasound beam, it can be used to create lesions in tissue. The application of HIFU induces tissue coagulation necrosis by a sharp temperature increase inside the tissue.[5] The formation of such lesions is widely described by Fry *et al.* in 1970, Frizzel *et al.* in 1988, ter Haar *et al.* in 1989, and Chapelon *et al.* in 1990.[5] The physical explanation of the creation of lesions is assumed to arise from two principal phenomena:

1. a thermal effect linked to absorption of ultrasound waves,
2. and cavitation, which is formation of bubbles which collapse.

The combination of these effects is responsible for the slightly conical form of the elementary lesions caused by each ultrasound shot.[5] Gelet *et al.*[5] has used HIFU to treat 102 patients with prostate cancer, and has shown an overall success rate of 66%, which is comparable to results from treatment with radio therapy. The benefit of using HIFU compared to radio therapy is that there is no maximum dose, and the treatment can thus be reapplied as many times as needed.

HIFU is not limited to treatment of prostate cancer but can also be used on the breast, the brain; in general everywhere ultrasound is used.

For breast treatment, aberration correction of the treatment beam becomes an important issue. HIFU treatment of cancer tumors is dependent on very narrow point like focused beams in order to know exactly where the treatment is being administered. As discussed in the previous section, the female breast is highly heterogeneous and offers strong challenges for detailed imaging, and thus also for HIFU treatment. If HIFU is successfully implemented for cancer treatment of the breast, a large part of small "uncertain" tumors can be treated with minimal side effects for the patients

At Laboratoire Ondes et Acoustiqe in Paris, France, experiments of aberration corrected HIFU treatment through sheep scull[6] has been successfully demonstrated without having to open the scull. In the future, this could become a very important area for treatment of tumors in the brain.

IV Practical aspects of aberration correction

Three basic practical aspects can be devised concerning implementation of aberration correction in an ultrasound scanner. These are:

- ultrasound arrays
- frequency
- computational requirements

All three points are somewhat connected.

IV.A Ultrasound arrays

For aberration correction to be properly estimated, 2D ultrasound matrix arrays with fully programmable elements are necessary. A 2D matrix phased array needs elements as small as $\lambda/2$ in order to avoid grating lobes when direction steering the beam. Such an array may contain 3000 elements for a 2.5 MHz probe used for cardiac imaging.

In order for a 2D array with 3000 elements to be tractable to the physician, the cable connecting the probe to the ultrasound scanner has to be of reasonable size. To overcome this problem, the 2D matrix arrays now on the market group elements together by beamforming, and normally reduce the number of cables to 256. This means that radio frequency data is only available for the 256 grouped elements, which may not be sufficient for aberration estimation. In general, estimation of aberration requires the elements to be smaller than the correlation length of the aberration parameters to be estimated. Usually, this requirement is much larger than standard beamforming requirements.

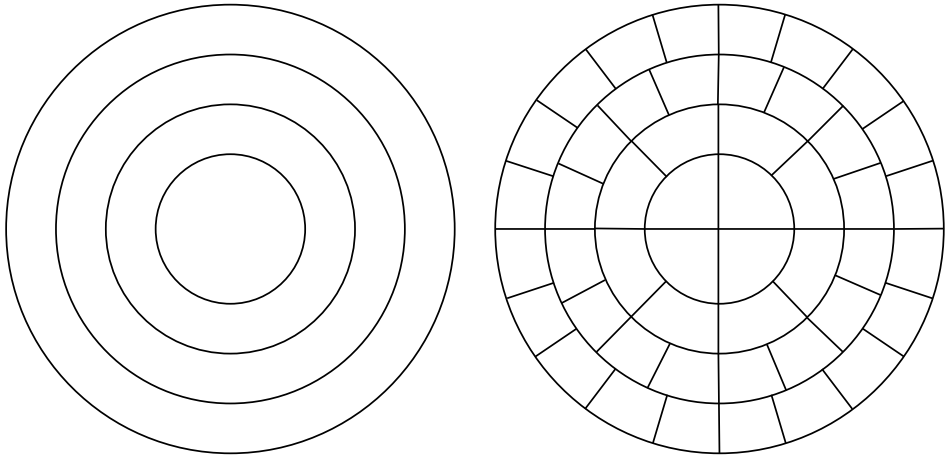

(a) Annular array (b) Sectioned annular array

Figure 1.4: Illustration of an annular array and a possible sectioning of such an array.

Based on the latter discussion, it is plausible to conclude that aberration correction should be performed in the probe, reducing the size of the cable. This generates a demand for development of small sized dedicated hardware.

Rigby *et al.*[7] used a 1.75D array for *in vivo* testing of an aberration correction scheme. Such an array has fewer elements, overcoming to some extent the problem discussed above, and allows for larger apertures in real time aberration correction.

IV.B Frequency

As described earlier, imaging of the female breast is performed at frequencies ranging from 7-12 MHz. Now, fulfilling the $\lambda/2$ requirement for direction steering of the beam becomes difficult as the number of elements increase to an unwieldy number. A solution to this could be to use annular arrays where the annular piezoelectric rings are sectioned into smaller elements (see Fig. 1.4). Such an array may be placed on a rotating motor, giving the desired direction steering of the beam. This remains a topic for future research.

IV.C Computational requirements

Aberration correction methods typically involve cross-correlation. Using the example above, cross-correlating a total of 3000 elements for each transmitted beam becomes an expensive computational task for a real time imaging system. This means that research must be performed on fast implementation of aberration estimation algorithms, in order to reduce computation time.

As an example, the aberration estimation algorithms presented in this thesis use an average of complex cross-correlations between a specific element, and a number of neighboring elements. This number, which varies with the strength of the aberration, could be in the order of 10. For a 2D array, this means that aberration estimation on a single element requires 100 complex multiplications. The total number of complex multiplications is then in the order of 300 000 for each transmitted beam.

V Basic theory

This section gives a brief introduction to basic wave equation analysis. It introduces a mathematical description of aberration through modeling the Green's function for a heterogeneous medium. A heterogeneous medium is defined by variable bulk compressibility and mass density, producing a spatial variable speed of sound. A homogeneous medium is given by a constant speed of sound.
The derivations in this section follows Angelsen.[8,9]

In the presented analysis of the wave equation, the medium is assumed to constitute a continuum. Shear waves are neglected, and a linear relation between relative volume compression and pressure is assumed via the bulk compressibility. Absorption and non-linear propagation effects are not included.

V.A The homogeneous wave equation and Green's function

Propagation of pressure waves in a homogeneous medium is described by the wave equation given as

$$\nabla^2 p(\mathbf{r},t) - \frac{1}{c^2}\frac{\partial^2 p(\mathbf{r},t)}{\partial t^2} = 0 \ , \tag{1.1}$$

where p denotes pressure, $\mathbf{r}$ represents a field-coordinate, and t time. Here, c denotes the speed of sound and is given as

$$c = \frac{1}{\sqrt{\rho\kappa}} \ , \tag{1.2}$$

where ρ is the mass density, and κ the bulk compressibility of the medium. The left side of Eq. (1.1) is often referred to as the d'Alembert operator.

Introducing a source $q(\mathbf{r},t)$, the nonhomogeneous[10] wave equation may be written as

$$\nabla^2 p(\mathbf{r},t) - \frac{1}{c^2}\frac{\partial^2 p(\mathbf{r},t)}{\partial t^2} = -q(\mathbf{r},t) \ , \tag{1.3}$$

A particular[10] solution of this equation can be found by considering a source limited to a small volume V, dwelling in infinite space. This solution can be found by the use of the Fourier transform of Eq. (1.3), and is given as

$$p(\mathbf{r},t) = \int_V \mathrm{d}r_0^3 \int_{-\infty}^{\infty} \mathrm{d}t_0 \ g_h(\mathbf{r}-\mathbf{r}_0, t-t_0) q(\mathbf{r}_0, t_0) \ , \tag{1.4}$$

where the integration is over the volume V, and $\mathbf{r}_0$ denotes the position of the source. The function g_h represents the Green's function for the homogeneous wave equation in infinite space and is given as

$$g_h(\mathbf{r},t) = \frac{\delta(t-r/c)}{4\pi r} \ , \tag{1.5}$$

where $r = |\mathbf{r}|$.

The homogeneous Green's function is the solution of the wave equation when the source term is given by an impulse in both space and time. It describes the propagation of a crest wave in a medium with constant speed of sound. Equation (1.4) thus describes the pressure at the point $\mathbf{r}$ in space and time t, which emanated from the source q at time t_0 (situated in $\mathbf{r}_0$).

In a heterogeneous medium, the speed of sound varies with the spatial coordinate, and the homogenous Green's function is no longer a particular solution of the wave equation. Still, the analogy is strong, and similar expressions as above may be adopted for the solution of the wave equation with a varying speed of sound; the heterogeneous wave equation.

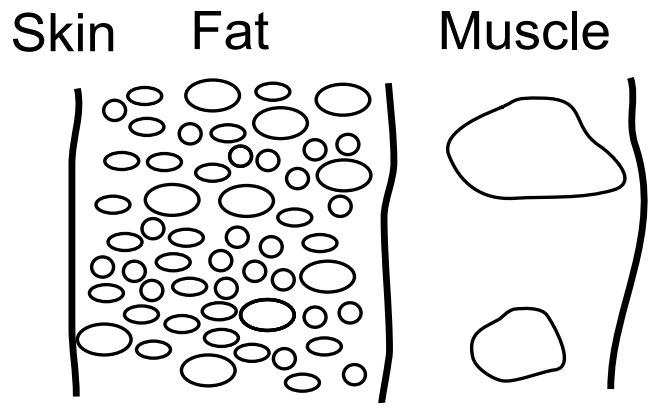

Figure 1.5: Schematic drawing of the body wall.

V.B The heterogeneous wave equation and Green's function

Heterogeneous tissue has a spatial fluctuating mass density ρ and bulk compressibility κ. As described earlier, aberration is mainly generated in the body wall while the organs produce little aberration. A schematic drawing of the human body wall is presented in Fig. 1.5. It is composed of the skin, a subcutaneous fat layer and a muscle layer.

In Ref. 11, it is shown that large tissue interfaces, approximately normal to the propagation direction, as *e.g.* between the subcutaneous fat layer and muscle layer, do not contribute significantly to overall distortion of the ultrasound signal. It is shown that large scale time-delay variations mainly are generated in the muscle layers. Rapid small scale fluctuations of both time-delays and amplitudes are generated in the subcutaneous fat layer.

The thickness of the subcutaneous fat layer in humans commonly varies from approximately 0.5-6 cm.[12] It is highly heterogeneous, and is composed of small ovoid or spherical lobules of fat of size ranging from 2.5-7.5 mm. They are held together by thin fibrous connective tissue. The speed of sound for fat is 1448 m/s, and for connective tissue 1613 m/s, constituting the largest difference in soft tissue. The muscle layer often contains large marmorized regions of fat (as illustrated in the figure). The muscle layer is also in many cases much thinner than the subcutaneous fat layer, especially for obese patients. The fatty regions introduce large scale time-delay differences in the propagating wave. A detailed description of body wall anatomy, and its implications on aberration is provided in Ref. 12.

Spatial variations in the mass density and compressibility may be modeled as

$$\begin{aligned} \rho(\mathbf{r}) &= \rho_a(\mathbf{r}) + \rho_f(\mathbf{r}) \\ \kappa(\mathbf{r}) &= \kappa_a(\mathbf{r}) + \kappa_f(\mathbf{r}) \ . \end{aligned} \tag{1.6}$$

Here, ρ_a and κ_a represents slow spatial variations around an average background with rapid fluctuations ρ_f and κ_f across tissue interfaces. The slow varying components typically represents scales of size larger than the wavelength, while the rapid fluctuations express scales less than the wavelength.

Writing the wave equation with variable mass density and compressibility gives

$$\nabla \left\{ \frac{1}{\rho(\mathbf{r})} \nabla p(\mathbf{r}, t) \right\} - \kappa(\mathbf{r}) \frac{\partial^2 p(\mathbf{r}, t)}{\partial t^2} = 0 \ . \tag{1.7}$$

Inserting Eq. (1.6) into Eq. (1.7), and rearranging terms, the heterogeneous wave equation may be written as

$$\nabla^2 p(\mathbf{r},t) - \frac{1}{c^2(\mathbf{r})}\frac{\partial^2 p(\mathbf{r},t)}{\partial t^2} = \frac{\beta(\mathbf{r})}{c^2(\mathbf{r})}\frac{\partial^2 p(\mathbf{r},t)}{\partial t^2} + \nabla\{\gamma(\mathbf{r})\nabla p(\mathbf{r},t)\} \ . \tag{1.8}$$

Now, the speed of sound is given as

$$c(\mathbf{r}) = \frac{1}{\sqrt{\rho_a(\mathbf{r})\kappa_a(\mathbf{r})}} \ , \tag{1.9}$$

and the parameters β and γ are defined as

$$\beta(\mathbf{r}) = \frac{\kappa_f(\mathbf{r})}{\kappa_a(\mathbf{r})} \ , \ \gamma(\mathbf{r}) = \frac{\rho_f(\mathbf{r})}{\rho(\mathbf{r})} \ . \tag{1.10}$$

To obtain Eq. (1.8), the assumption of $\nabla\rho_a(\mathbf{r}) \approx 0$ was used. Note that for β, it is κ_a which enters into the denominator, while for γ it is the total mass density ρ.

Equation (1.8) can be interpreted as a wave equation with a source term

$$\nabla^2 p(\mathbf{r},t) - \frac{1}{c^2(\mathbf{r})}\frac{\partial^2 p(\mathbf{r},t)}{\partial t^2} = -q(\mathbf{r},t) \ , \tag{1.11}$$

where

$$q(\mathbf{r},t) = -\frac{\beta(\mathbf{r})}{c^2(\mathbf{r})}\frac{\partial^2 p(\mathbf{r},t)}{\partial t^2} - \nabla\{\gamma(\mathbf{r})\nabla p(\mathbf{r},t)\} \ . \tag{1.12}$$

The heterogeneous wave equation in Eq. (1.11) is linear with derivatives of the pressure. This is also true for the source term. It can therefore be solved in the same manner as Eq. (1.3), *i.e.* the total field can be described by an integral solution involving a Green's function and the source term. This solution is conveniently found via the Helmholtz-Kirchoff's formula [Ref. 8 (Ch. 4.3)], again assuming a limited source volume dwelling in infinite space.

Due to the varying speed of sound, the Green's function is no longer only a function of the distance between the source position $\mathbf{r}_0$ and the field point $\mathbf{r}$.

In analogy with Eq. (1.4), a solution of Eq. (1.11) may be written as

$$p(\mathbf{r},t) = \int_V \mathrm{d}r_0^3 \int_{-\infty}^{\infty} \mathrm{d}t_0 \ g(\mathbf{r},\mathbf{r}_0,t-t_0)q(\mathbf{r}_0,t_0) \ , \tag{1.13}$$

where $g(\mathbf{r},\mathbf{r}_0,t)$ now represents the heterogeneous Green's function. Note that this Green's function is dependent on both the field-point and the source point, and satisfies the wave equation

$$\nabla^2 g(\mathbf{r},\mathbf{r}_0,t-t_0) - \frac{1}{c^2(\mathbf{r})}\frac{\partial^2 g(\mathbf{r},\mathbf{r}_0,t-t_0)}{\partial t^2} = -\delta(\mathbf{r}-\mathbf{r}_0)\ \delta(t-t_0) \ . \tag{1.14}$$

Fourier transforming Eq. (1.13) in time, produce the Helmholtz solution of the heterogeneous wave equation as

$$p(\mathbf{r};\omega) = \int_V \mathrm{d}r_0^3 \ g(\mathbf{r},\mathbf{r}_0;\omega)q(\mathbf{r}_0;\omega) \ , \tag{1.15}$$

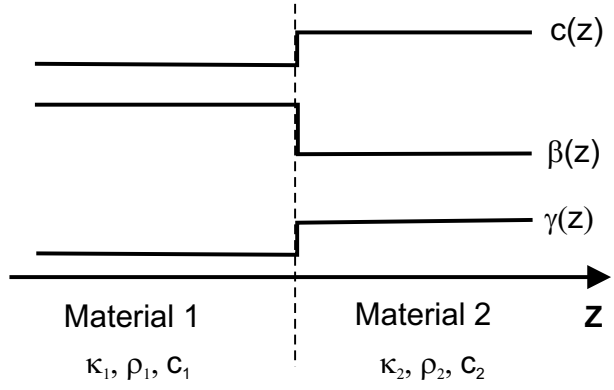

Figure 1.6: Plane wave analysis of two homogeneous materials with different mass density and compressibility.

Interpretation of the source term in the heterogeneous wave equation

The source term in Eq. (1.8) will produce both forward and back scattering of the propagating wave. This is due to the fluctuations in compressibility and mass density given by β and γ. For the purpose of analysis, assume a plane wave situation between two homogeneous materials with different mass density and compressibility as shown in Fig 1.6. Assume an incoming wave in Material 1 on the form $p_0(z,t) = p_0(t - z/c_1)$. In the Born approximation regime, it is shown in Ref. 9 (Ch. 7.3) that the first order scattered field p_1 from the interface may be written as

$$\begin{aligned} p_1(z,t) = \frac{1}{2}\frac{\partial p_0(t-z/c_1)}{\partial z}\int_{-\infty}^{z} \mathrm{d}z_0\ \nu_f(z_0) - \frac{\nu_b(z)}{4}p_0(t-z/c_1) \\ - \frac{1}{4}\int_{z}^{\infty} \mathrm{d}z_0\ p_0(t+z/c_1-2z_0/c_1)\frac{\partial \nu_b(z_0)}{\partial z_0}\ . \end{aligned} \tag{1.16}$$

The functions ν_f and ν_b are given as

$$\nu_f(z) = \beta(z) + \gamma(z)\ ,\ \nu_b(z) = \beta(z) - \gamma(z)\ , \tag{1.17}$$

and represents the forward and backscatter density.

The two first terms of Eq. (1.16) represents forward scattered waves which adds to the incoming transmitted wave. The last term is a backwards propagating wave and represents reflections at the interface. The total forward field after the interface is then

$$\begin{aligned} p_f(z,t) &= p_0(t-z/c_1) + \frac{1}{2}\frac{\partial p_0(t-z/c_1)}{\partial z}\int_{-\infty}^{z} \mathrm{d}z_0\ \nu_f(z_0) - \frac{\nu_b(z)}{4}p_0(t-z/c_1) \\ &= Tp_0(t-z/c_1) + \frac{1}{2}\frac{\partial p_0(t-z/c_1)}{\partial z}\int_{-\infty}^{z} \mathrm{d}z_0\ \nu_f(z_0)\ , \end{aligned} \tag{1.18}$$

where $T = 1 - \nu_b(z)/4$, and represents a transmission coefficient for the incoming field.

In Eq. (1.16), the back scattered field is dependent on the gradient of the backscatter density, while the forward scattered field is dependent on the integral of the forward scatter density. The modeling of ρ and κ in Eq. (1.6) allows for some flexibility in how to chose the variations of the slow and rapid changing functions.

An example for the compressibility is shown in Fig. 1.7. Here, κ_a has a slow and linear variation over a defined transition region of length L. The fluctuating term, represented by β,

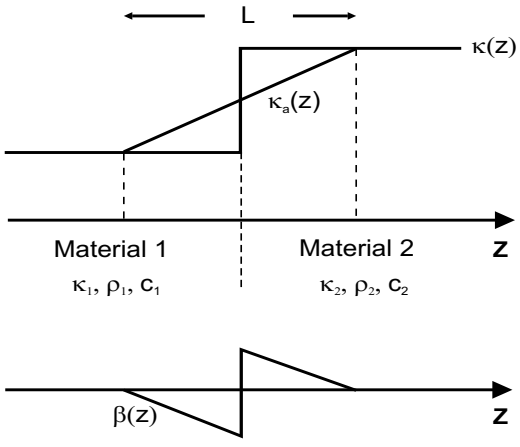

(a) Symmetric transit region

Figure 1.7: Slow and rapid variations of compressibility.

has in impulse like form over the transition region. The variation of the parameters in the transit region may be chosen to be symmetric in β and γ. For a symmetric transit region, the integral over the fluctuating term will be zero. This results in a transmitted wave p_0, but no forward scattering is generated. The backscatter is dependent on the gradient of the fluctuating terms and is not zero. Note that, in the Born approximation regime, this choice of parameters produce a small time-delay error in the back scattered field. Assuming a transit region of $L = 2\lambda$, it is shown in Ref. 9 (p. 7.22) that the error for the reflected wave between fat and muscle tissue, is only $\sim 4\%$ of the pulse period. This is highly acceptable.

The above discussion shows that the source term in the heterogeneous wave equation may be interpreted to only represent back scattering of an incoming wave. That is, choosing appropriate values for the slowly varying and rapid fluctuating parts of the mass density and bulk compressibility, no forward scattering is generated by the source term. This leads to the recognition that all modification of the forward propagating field is incorporated in the d'Alembert operator, *i.e.* the part of the wave equation describing propagation of the field. In addition, this modification is generated by the slow variation of the mass density and compressibility, defined by the speed of sound $c(\mathbf{r})$ in Eq. (1.11).

V.C Modeling of the heterogeneous Green's function - the concept of the screen

The solution of the homogeneous wave equation with a source term in Eq. (1.4), is analog to the solution of the heterogeneous wave equation given in Eq. (1.13). The difference is in the construction of the Green's function, which for a homogeneous medium only is a function of the distance from the source position to the point of observation (the field point). The heterogeneous Green's function also varies in each spatial position due the changing speed of sound in the medium. Since the solutions are conceptually equal, the difference is conveniently modeled using the concept of the *generalized frequency-dependent screen.*

The heterogeneous Green's function is then written in the frequency domain as

$$g(\mathbf{r}, \mathbf{r}_0; \omega) = s(\mathbf{r}, \mathbf{r}_0; \omega)\ g_h(\mathbf{r} - \mathbf{r}_0; \omega)\ , \tag{1.19}$$

that is, the difference between the homogeneous and heterogeneous situation is modeled by a linear filter equation. Here, $s(\mathbf{r}, \mathbf{r}_0; \omega)$ denotes the generalized frequency-dependent screen, from now on denoted as *the screen*, and represents the frequency response of a filter which produces a modification of a homogeneous propagating field. The modification is given by a frequency dependent phase and amplitude factor, and is interpreted as aberration of the wave introduced by tissue inhomogeneities. Based on the discussion in the previous section, such a modelling is justifiable since aberration is generated by the d'Alembert operator of the wave equation.

Writing the screen with an amplitude and phase as

$$s(\mathbf{r}, \mathbf{r}_0; \omega) = a(\mathbf{r}, \mathbf{r}_0; \omega) e^{i\theta(\mathbf{r}, \mathbf{r}_0; \omega)} \ , \tag{1.20}$$

it is seen that non-linear variation of the phase with frequency produce stretching of the wave. Allowing a complex valued amplitude, may be interpreted as an additive frequency dependent phase factor, which again can be incorporated into θ. Thus for all practical purposes, the amplitude is assumed to be real valued.

Assuming a point impulse source exists in the focus $\mathbf{r}_f$ of an array, it is seen from Eq. (1.13) that the field received on the array is directly given by the Green's function. The aberration of the medium can then be explicitly found through the screen. Filtering the transmitted field on each array element with the complex conjugate of the screen, is in this case equivalent to time reversal[13] and reproduces the diffraction limited impulse field in $\mathbf{r}_f$. Results corroborating this statement is provided in Ch. 2 of this thesis.

The complex conjugate of the screen thus defines an ideal aberration correction filter h for the focus point of an ultrasound array

$$h(\mathbf{r}_a; \omega) = s^*(\mathbf{r}_a, \mathbf{r}_f; \omega) \ , \tag{1.21}$$

where $\mathbf{r}_a$ denotes the array coordinate.

The main object of the work presented in this thesis, is to devise algorithms to determine the screen, and to use this as an aberration correction filter. In the literature, the most common investigated method for correcting aberration is to use a simple time-delay filter, or a time-delay and amplitude filter. Such filters are defined in the frequency domain as

$$h(\mathbf{r}_a; \omega) = e^{i\omega\tau(\mathbf{r}_a)} \tag{1.22}$$

$$h(\mathbf{r}_a; \omega) = a(\mathbf{r}_a) e^{i\omega\tau(\mathbf{r}_a)} \ , \tag{1.23}$$

and represent approximations to the ideal correction filter given by the screen.

A correction filter using a simple time-delay cannot correct for non-linear phase variations with frequency. In Ch. 2, it is shown that a time-delay and amplitude filter produce close to ideal aberration correction when estimated from a point source. This indicates that non-linear variations of the phase of the screen with frequency can be neglected for low-frequency ultrasound imaging (1-3 MHz). The results were obtained using a transmit pulse with 2.5 MHz center frequency. The same conclusion was found by measurements performed at 3 MHz.[14]

V.D The receive signal model: Scatterer independent aberration

Inserting the model of the heterogeneous Green's function in Eq. (1.19) into Eq. (1.15) gives

$$p(\mathbf{r}; \omega) = \int_V \mathrm{d}r_0^3 \ s(\mathbf{r}, \mathbf{r}_0; \omega) g_h(\mathbf{r} - \mathbf{r}_0; \omega) q(\mathbf{r}_0; \omega) \ . \tag{1.24}$$

This equation can be analyzed with respect to the size of the source volume V.

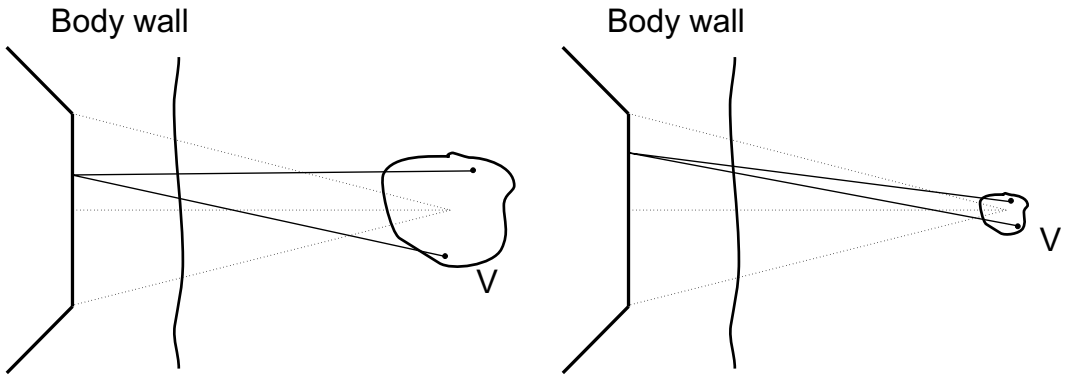

(a) Scatterer dependent aberration (b) Scatterer independent aberration

Figure 1.8: Receive scatterer dependent and independent situations.

Figure 1.8 depicts an ultrasound array with a body wall in front of it. Assume the medium from the body wall to the source volume V to be homogeneous. In the general case, the field received on a point $\mathbf{r}$ on the array is dependent on the sum of the contribution of sources, each with its specific Green's function. This is what Eq. (1.24) describes. For this case, a separate screen function must be applied to each contributing source due to their different propagation paths as show in Fig. 1.8 (a).

Similarly to Eq. (1.24), the received signal on an array element y can be written as

$$y(\mathbf{r};\omega) = \int_V \mathrm{d}r_0^3 \; 2s(\mathbf{r},\mathbf{r}_0;\omega) g_h(\mathbf{r}-\mathbf{r}_0;\omega) q_{ts}(\mathbf{r}_0;\omega) \; . \tag{1.25}$$

Here the source term q_{ts} incorporates the transmitted field and scattering from the volume, and may hence be viewed as a scattering term. Equation (1.25) describes a situation which here is termed *receive scatterer dependent aberration* and abbreviated *scatterer dependent aberration*.

If the focused transmit beam insonifies a small scattering volume, so small that the propagation path is approximately the same for each scatterer contribution, the screen is independent of scatterer position and the received signal can be approximated as

$$y(\mathbf{r};\omega) \approx s(\mathbf{r};\omega) \int_V \mathrm{d}r_0^3 \; 2g_h(\mathbf{r}-\mathbf{r}_0;\omega) q_{ts}(\mathbf{r}_0;\omega) \equiv s(\mathbf{r};\omega) \; f(\mathbf{r};\omega) \; . \tag{1.26}$$

This situation, depicted in Fig. 1.8 (b), is here denoted *receive scatterer independent aberration* and abbreviated *scatterer independent aberration*. The screen is now referred to as the *scatterer independent screen*. A volume of scatterers fulfilling this requirement is denoted an *isoplanatic patch*, a term coined in astronomy where similar effects are considered when the light from distant stars pass through the atmosphere. Note that if the array is focused in a different direction, the source distribution and propagation path change, giving a different screen. This means that the screen generally is a function of the focus $\mathbf{r}_f$ of the array.

If all aberration is concentrated in an infinitely thin layer at the array surface, the screen also becomes independent of the focusing position of the array and

$$s(\mathbf{r},\mathbf{r}_0;\omega) = s(\mathbf{r},\mathbf{r}_f;\omega) \equiv s(\mathbf{r};\omega). \tag{1.27}$$

Note that for an infinitely thin aberrating layer situated some distance from the array, the assumption of scatterer independent aberration does not hold.

In general aberration correction must be performed by filtering the transmitted signal with a correction filter of some sort. This means that the assumption of scatterer independent aberration should be fulfilled to a certain extent for proper estimation of aberration characteristics.

V.E The Van Cittert-Zernike theorem

Scatterers contributing to an ultrasound image, are randomly distributed in space. The receive signal is therefore a stochastic variable. Note that for a specific beam, the screen is deterministic.

The van Cittert-Zernike theorem [15] was developed for propagation in a homogenous medium. The theorem describes the spatial covariance in the received signal when the scattering is incoherent. Using the assumption of scatterer independent aberration, the theorem remains valid and may be written as [Ref. 9 (p. 11.55)]

$$F(\boldsymbol{\xi};\omega) = \frac{\sigma_\nu^2}{4\pi^2}\int_{S_a} \mathrm{d}r^2 \; s(\mathbf{r}+\boldsymbol{\xi};\omega)s^*(\mathbf{r};\omega)o(\mathbf{r}+\boldsymbol{\xi})o^*(\mathbf{r}) \;, \tag{1.28}$$

where F is the covariance of f. Here σ_ν^2 is the scattering intensity, the integration is performed over the array surface S_a, and $o(\mathbf{r})$ denotes the array apodization function.

Equation (1.28) shows that the covariance in the received signal is limited by the aberration as well as the apodization of the array.

If aberration correction is performed by using the complex conjugate of the screen, the theorem becomes

$$F(\boldsymbol{\xi};\omega) = \frac{\sigma_\nu^2}{4\pi^2}\int_{S_a} \mathrm{d}r^2 \; |a(\mathbf{r}+\boldsymbol{\xi};\omega)|^2|a^*(\mathbf{r};\omega)|^2 \;, \tag{1.29}$$

where a is the amplitude of the screen as defined in Eq. (1.20), and the screen has been used as an apodization function. This means that the covariance of the received transmit corrected field is given by the correlation of the aberration amplitude squared.

V.F Aberration as a function of frequency

Aberration is an interference phenomenon. Interference is highly dependent on frequency. This strongly suggests that aberration also depends on frequency. This is mathematically stated by the generalized frequency-dependent screen, and van Cittert-Zernike theorem as described by Eq. (1.28). Very little research (or any at all) has been devoted to study the relation between frequency and aberration.

When imaging at high frequencies (7-15 MHz) the wavelength is in the order of 0.1 mm-0.2 mm (for water), compared to 0.6 mm at 2.5 MHz. This means that a specific time shift between two signals has a much more drastic effect when using higher frequencies. For example, a time-delay of 100 ns produce a shift of 0.15 mm. This represents 1/4 of a wavelength for a 2.5 MHz pulse, and 3/4 of a wavelength for a 7.5 MHz pulse. Strong time-delays between signals also introduce a non-linear varying phase with frequency. A discussion of aberration as a function of frequency is given in Appendix A.

VI Assumptions for the work presented in this thesis

All the results presented in this work are generated from simulations. Using simulations, pure aberration effects can be studied by eliminating factors such as reverberations and absorption. All phenomena occurring, can then be described uniquely by propagation effects linked to aberration

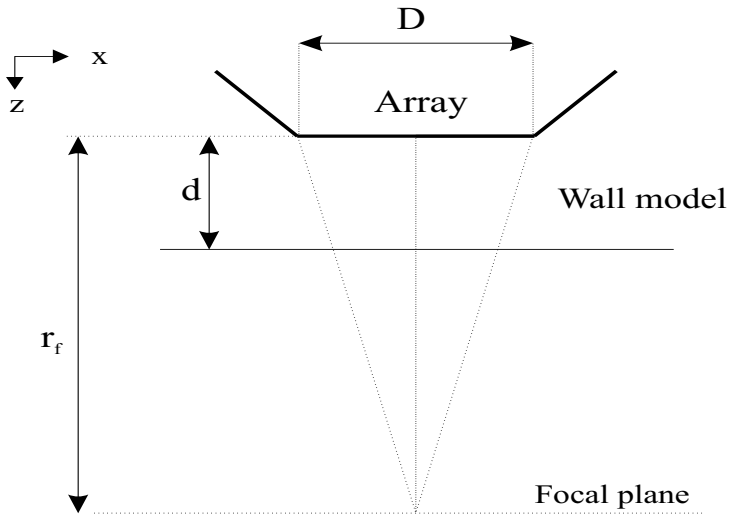

Figure 1.9: Basic simulation setup.

of the ultrasound signals. This again shows the maximum potential of aberration estimation and correction methods.

In a practical situation, reverberations, absorption, and electronic noise may affect both estimation and correction of aberration. Such effects, and their implications upon aberration estimation/correction are discussed in the following chapters of this thesis.

The simulations are carried out in two spatial directions and time. Acoustic absorption, reverberations and electronic noise are not included in the simulations.

The basic simulation setup is illustrated in Fig. 1.9. An ultrasound array with size D, is placed directly onto a body wall model of thickness d. The array is focused at position $\mathbf{r}_f$. The array elements are assumed to be point like in size, which means that element directivity is not accounted for.

The body wall is modeled using a distributed aberrator composed of successive time-delay screens. Note that only aberration from a body wall is studied, and not aberration from totally heterogeneous objects like the female breast.

For propagation, an angular spectrum method was used. A description of the propagation operator, and the aberration modeling, is provided in Ch. 2.

Random scattering is simulated using uniformly distributed scatterers with a Gaussian reflection strength. This means that scattering from objects or structures such as strong scattering or anechoic regions, is not investigated.

The simulations are implemented in MATLAB, and a package of functions has been created (over the past four years) for this purpose. This package is available free at *www.ntnu.no/∼sveinmas/*.

VII Overview of thesis

The thesis is composed of four chapters (in addition to this chapter). The chapters are written in the form of separate articles, and may hence be read individually. Due to this composition,

some aspects concerning basic theory, simulation setup, and data processing are repeated but all chapters introduce new theoretical considerations and simulation results. Chapters 2 and 3 are published as articles in the *Journal of the Acoustical Society of America* (JASA), and they are in the following referred to in their published form. Chapter 4 has been accepted for publication in JASA, and is scheduled for publication in December 2004, or January 2005. The last chapter is also planned for publication.

There are some changes in the presented material compared to the already published work. The changes are related to erroneous statements concerning basic assumptions for the aberration estimation methods presented. This only concerns a few phrases in each of the articles. Other aspects are not changed. These are connected to an increased theoretical and physical understanding of the estimators, and is meant to show an improved scientific understanding throughout the thesis. Hopefully, this will also become clear to the reader.

Minor changes in notation has been introduced in order to make it consistent throughout the presented work. There are also some corrections of spelling errors and phrasing.

Chapter 2 and 3, were accompanied with an errata with correction of minor calculation errors in the articles. These corrections are included here.

In Ch. 2,[16] aberration is estimated from a point source in the focus of an array. The basic result from this work shows that, if properly estimated, aberration can be corrected using a simple time-delay and amplitude filter applied on transmit. This is an approximation to the generalized frequency-dependent screen as given in Eq. (1.23).

Chapter 3,[17] presents an algorithm for determining the generalized frequency-dependent screen. The method is developed in the frequency domain. Based on the results from Ch. 2, the screen is approximated by a time-delay and amplitude filter. The main result shows that a single transmit beam may not be sufficient for determining the aberration correctly. This is due to the width of the aberrated transmit beam, which generally is larger than the isoplanatic patch. For this case, the assumption of scatterer independent aberration, which is fundamental for aberration correction, does not hold. With a back scattered signal from a region larger than the isoplanatic patch, the received signal is severely distorted due to the thickness of the body wall, creating strong aberration generated interference in addition to scatterer interference. This effect smoothens aberration parameters and they cannot be properly estimated.

A solution to this problem may be sought by iteration of transmit-beam aberration correction (transmit-beam iteration). Transmit-beam iteration is described as a process where an uncorrected transmit-beam is used for an initial estimate of aberration parameters. A new beam with correction is then transmitted, generating a new estimate of the parameters. This process is repeated until some convergence criterion is met.

Iteration of transmit-beam aberration correction is studied in Ch. 4.[18] Two developed algorithms for estimating aberration are here compared, where one of them is described in Ch. 3, and the other in Ref. 19. Transmit-beam iteration offers new theoretical insight into the similarities and differences between the algorithms. The results show that using a time-delay and amplitude aberration correction filter, both algorithms provide close to ideal aberration correction after two to three transmit-beam iterations. In addition, an earlier developed focus criterion[20] proves to give accurate description of the point of convergence, and the accuracy of the correction.

Both the aforementioned aberration algorithms are based on a cross-correlation estimation process. Different methods of averaging the cross-correlation can be applied to improve its estimate. For example, imaging a large artery provides moving scatterers which are replaced within a brief period of time. Transmitting several beams with the same focus and amplitude then yields statistically independent receive signals, which can be used to ameliorate the cross-correlation estimate. Alternatively, neighboring beams with multiple focusing in a sector/linear

scan may be used for the same purpose.[7,14,21]

Since the receive signal in ultrasound imaging is a stochastic variable, estimation of arrival time-delays and amplitudes at the array, is connected with uncertainty. In Ch. 5, a variance analysis of arrival time and amplitude fluctuation estimates is performed. The variance is investigated with respect to averaging the cross-correlation estimate over a varying number of independent receive signals. In addition, a time domain implementation of the estimation algorithm developed in Ch. 3 is given, and the differences between the two implementations are examined. The results show only minor differences between the two implementations with respect to variance. The standard deviation of arrival time and amplitude fluctuation estimates decrease, when the number of independent signals used increase. Using only one signal produces a relatively high standard deviation, but the results indicate that an iterative transmit-beam aberration correction scheme still converges to a properly corrected focus beam profile.

References

[1] T. Douglas Mast, Laura M. Hinkelman, and Michael J. Orr, V. W. Sparrow, and R. C. Waag, "Simulation of ultrasonic pulse propagation through the abdominal wall," *J. Acoust. Soc. Am.*, vol. 102, no. 2, pp. 1177–1190, August 1997.

[2] L. M. Hinkelman and D.-L. Liu, L. A. Metlay, and R. C. Waag, "Measurements of ultrasonic pulse arrival time and energy level variations produced by propagation through abdominal wall," *J. Acoust. Soc. Am.*, vol. 95, no. 1, pp. 530–541, January 1994.

[3] W. C. Black and H. G. Welch, "Advances in diagnostic imaging and overestimations of disease prevalence and the benefits of therapy," *New England J. Med.*, vol. 328, pp. 1237–1243, April 1993.

[4] P.-H. Zahl, B. Heine, and J. Mæhle, "Incidence of breast cancer in norway and sweden during introduction of nationwide screening: prospective cohort study," *British Medical Journal*, vol. 328, pp. 921–924, April 2004.

[5] A. Gelet, J. Chapelon, R. Bouvier, O. Rouvière, Y. Lasne, D. Lyonnet, and J. M. Dubernard, "Transrectal high-intensity focused ultrasound: Minimally invasive therapy of localized prostate cancer," *Journal of Endourology*, vol. 14, no. 6, August 2000.

[6] M. Pernot, J.-F. Aubry, M. Tanter, M. Fink, A.-L. Boch, and M. Kujas, "Ultrasonic brain therapy: First trans-skull in vivo experiments on sheep using adaptive focusing," *J. Acoust. Soc. Am.*, vol. 115, p. 2524, 2004.

[7] K. W. Rigby, C. L. Chalek, B. H. Haider, R. S. Lewandowski, M. O'Donnell, L. S. Smith, and D. G. Wildes, "Improved in vivo abdominal image quality using real-time estimation and correction of wavefront arrival time errors," *IEEE Ultrasonics Symposium*, vol. 2, pp. 1645–1653, October 2000.

[8] B. Angelsen, *Ultrasound imaging. Waves, signals and signal processing.* Trondheim: Emantec, 2000, vol. I, http://www.ultrasoundbook.com.

[9] B. Angelsen, *Ultrasound imaging. Waves, signals and signal processing.* Trondheim: Emantec, 2000, vol. II, http://www.ultrasoundbook.com.

[10] E. Kreyzig, *Advanced Engineering Mathematics*, 8th ed. Singapore: Wiley, 1999.

[11] T. D. Mast, L. M. Hinkelman, M. J. Orr, and R. C. Waag, "The effect of abdominal wall morphology on ultrasonic pulse distortion. part ii. simulations," *J. Acoust. Soc. Am.*, vol. 104, no. 6, pp. 3651–3664, December 1998.

[12] L. Hinkelman, T. D. Mast, L. A. Metlay, and R. C. Waag, "The effect of abdominal wall morphology on ultrasonic pulse distortion. part i. measurements," *J. Acoust. Soc. Am.*, vol. 104, no. 6, pp. 3635–3649, December 1998.

[13] M. Fink, C. Prada, F. Wu, and D. Cassereau, "Self focusing in inhomogeneous media with "Time Reversal" acoustic mirrors," *Ultrasonics Symposium, 1989 Proceedings, IEEE 1989*, pp. 681–686, 1989.

[14] T. Varslot, B. Angelsen, and R. C. Waag, "Spectral estimation for characterization of acoustic aberration," *J. Acoust. Soc. Am.*, vol. 116, no. 1, pp. 97–108, July 2004.

[15] R. Mallart and M. Fink, "The van Cittert-Zernike theorem in pulse echo measurements," *J. Acoust. Soc. Am.*, vol. 90, no. 5, pp. 2718–2727, November 1991.

[16] S.-E. Måsøy, T. F. Johansen, and B. Angelsen, "Correction of ultrasonic wave aberration with a time delay and amplitude filter," *J. Acoust. Soc. Am.*, vol. 113, no. 4, pp. 2009–2020, April 2003.

[17] S.-E. Måsøy, T. Varslot, and B. Angelsen, "Estimation of ultrasound wave aberration with signals from random scatterers," *J. Acoust. Soc. Am.*, vol. 115, no. 6, pp. 2998–3009, June 2004.

[18] S.-E. Måsøy and T. Varslot and B. Angelsen, "Iteration of transmit-beam aberration correction in medical ultrasound imaging," 2004, accepted for publication in JASA.

[19] T. Varslot, E. Mo, H. Krogstad, and B. Angelsen, "Eigenfunction analysis of stochastic backscatter for characterization of acoustic aberration in medical ultrasound imaging," *J. Acoust. Soc. Am.*, vol. 115, no. 6, pp. 3068–3076, June 2004.

[20] R. Mallart and M. Fink, "Adaptive focusing in scattering media through sound-speed inhomogeneities: The van Cittert Zernike approach and focusing criterion," *J. Acoust. Soc. Am.*, vol. 96, no. 6, pp. 3721–3732, December 1994.

[21] M. Karaman, A. Atalar, H. Köymen, and M. O'Donnell, "A phase aberration correction method for ultrasound imaging," *IEEE Trans. Ultrason. Ferroelectr. Freq. Control*, vol. 40, no. 4, pp. 275–282, July 1993.

Chapter 2

Correction of ultrasonic wave aberration with a time-delay and amplitude filter

S. Måsøy, T. F. Johansen, B. Angelsen
Department of Circulation and Imaging, NTNU.

2D simulations with propagation through two different heterogeneous human body wall models have been performed to analyze different correction filters for ultrasonic wave aberration due to forward wave propagation. The different models each produce most of the characteristic aberration effects such as phase aberration, relatively strong amplitude aberration and waveform deformation. Simulations of wave propagation from a point source in the focus (60 mm) of a 20 mm transducer through the body wall models were performed. Center frequency of the pulse was 2.5 MHz. Corrections of the aberrations introduced by the two body wall models were evaluated with reference to the corrections obtained with the optimal filter: a generalized frequency-dependent phase and amplitude correction filter.[1] Two correction filters were applied, a time-delay filter, and a time-delay and amplitude filter. Results showed that correction with a time-delay filter produced substantial reduction of the aberration in both cases. A time-delay and amplitude correction filter performed even better in both cases, and gave correction close to the ideal situation (no aberration). The results also indicated that the effect of the correction was very sensitive to the accuracy of the arrival time fluctuations estimate, *i.e.*, the time-delay correction filter.

I Introduction

Wave distortion in medical ultrasound imaging originates from inhomogeneities in the tissue, especially in the human body wall. Distortion of an ultrasonic wave, also known as aberration, leads to poorer resolution in the obtained images.

In the literature it is possible to deduce three different methods for correction of ultrasonic wave aberration.

1. A focusing and apodization method, where arrival time and amplitude fluctuations are corrected in the focusing and apodization of the transmitted signal. In this article this method will be denoted in the general case as a correction filter, or more specific as a time-delay correction filter alone or in combination with an amplitude correction filter.

Flax and O'Donnel[2] introduced a cross-correlation method for estimation of arrival time fluctuations in the received aberrated signal. This represents the classical method for estimation of arrival time fluctuations and has been extensively used in the literature on ultrasonic wave aberration.

2. Fink[3] introduced the time reversal mirror, which incorporates information about the pulse form in addition to arrival time and amplitude fluctuations. This method requires a point reflector in the insonified medium, which rarely is the case.

3. The back-propagation method introduced by Liu and Waag[4] propagates the signal homogeneously backwards in time in order to obtain an optimal situation for estimation of aberration parameters. For the case of estimating a time-delay correction filter, it is not yet completely understood if back-propagation followed by arrival time estimation works better than arrival time estimation at the transmitting array, for correction of the retransmitted wave.[5,6]

The objective of the work presented in this article was to find how well a time-delay correction filter, or a time-delay and amplitude correction filter, corrects for ultrasonic wave aberration. There has been performed much research on time-delay and amplitude correction of ultrasonic wave aberration[2,7–10], but all of this work has used a very simple aberration model consisting of a single pure time-delay screen placed just in front of, or some distance from the transmitting/receiving array. The work done by the ultrasound group at the University of Rochester,[11–16] has given valuable insight into how the inhomogeneities in the human body wall affect aberration of ultrasonic waves. This has been crucial in the understanding of this phenomenon, and possible corrections. Their work have also shown that a single time-delay screen model is to simple, and cannot adequately model ultrasonic wave aberration.

Berkhoff and Thijssen[6] introduced a number of successive time-delay screens to model ultrasonic wave aberration, but gave no characterization of the total accumulated effect of these successive screens. In the present article, the concept of successive time-delay screens have been further developed as a model of the human body wall, although this has been criticized not to be an appropriate method to model aberration introduced by propagation through the human body wall.[16] The main reason to create such a model was to simulate ultrasonic wave aberration with a relatively simple and non-expensive method. This method can be used to evaluate various techniques of estimation and correction of wave aberration. The work presented here shows that if care is used in designing the aforementioned wall model, it produces most of the reported aberration phenomena introduced by the human body wall.

A correction method using a generalized frequency-dependent phase and amplitude correction filter[1], was used as a reference for the best possible aberration correction. Such a filter comprises spatial and frequency dependency of both amplitude and phase fluctuations at the receiving array. Approximations of the generalized frequency-dependent correction filter with a time-delay filter alone, or in combination with an amplitude filter, was then evaluated from simulations of point sources placed in the focus of a focusing array. Simulations with point sources in the focus of an array provides the optimal situation for estimation of wave aberration. Six different methods were evaluated for the estimation of the time-delay correction filter. Absorption, reverberations, or electronic noise were not included in the simulations.

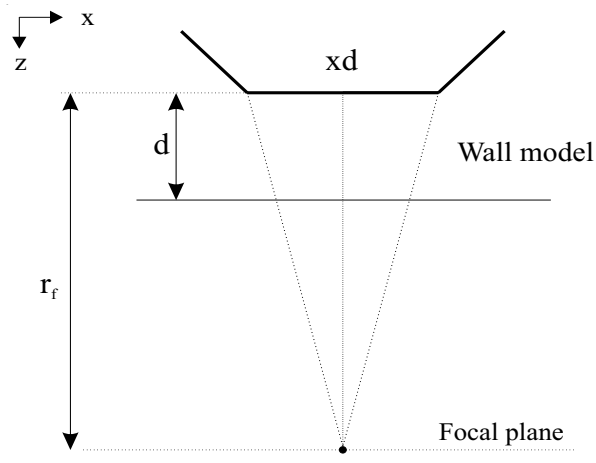

Figure 2.1: Simulation setup.

II Theory and method

II.A Simulation setup

The simulation setup is illustrated in Fig. 2.1. The figure depicts a simulation setup of a point source placed in the focus r_f of an array. A pulse was propagated from the point source through a body wall model of thickness d to the receiving array. A correction filter was estimated from the received signal and applied on transmit of a focused pulse. This pulse was propagated back to the focal plane for evaluation of the applied correction filter.

II.B Body wall modelling

The human body wall was modelled with different sets of several time-delay screens, in order to simulate various cases of aberration. A time-delay screen only introduces a shift in the phase of the ultrasonic signal with a pure time-delay. The time-delay screen was defined only in a plane (Fig. 2.2), and thus had zero thickness. The propagation through the body wall model was performed by homogeneous propagation with an angular spectrum operator (described in section II.C) between each time-delay screen.

In order to create different cases of aberration, 8 sequences of random numbers with a standard normal distribution were generated. These sequences were then low-pass filtered to obtain reported correlation lengths for the time-delays produced by the human abdominal wall. [11]

Four different configurations containing 2, 4, 6 and 8 sequences were selected in order to generate different aberration conditions. Various aberration situations could now easily be simulated by multiplying each configuration with an individual time-delay amplitude (given in seconds), thus turning the configuration into a set of time-delay screens. Note that in this article, all the time-delay screens in a specific configuration were multiplied with the same time-delay amplitude. The time-delay screens in a configuration, were uniformly spaced over a depth-range d with a distance $\Delta z = d/(number\ of\ screens)$ between them. The first time-delay screen was placed a distance Δz from the array, and the last was placed at the distance d from the array (see Fig. 2.2). To summarize: a given model of a body wall consisted of one of the above mentioned configurations, multiplied with a defined time-delay amplitude given in seconds, and distributed

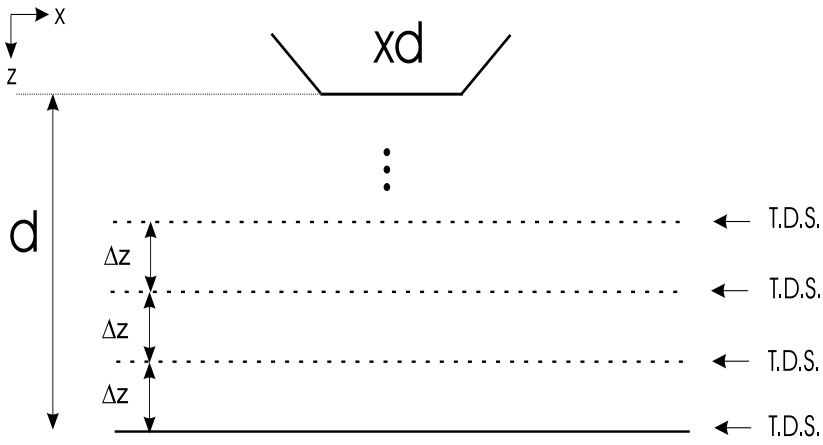

Figure 2.2: Body wall model with time-delay screens.

uniformly in space over a depth d.

Two categories of human body wall models were created, representing cases of weak and strong aberration. These two categories were not rigorously defined, but different created body wall models were placed into these categories after several selection criterions. The criterions were body wall statistics (correlation lengths and rms values of arrival time and energy level fluctuations), the level of waveform deformation (calculated by a waveform similarity factor), visual inspection of received arrival time and amplitude fluctuations, visual inspection of received waveforms, and visual inspection of aberrated beam profiles in the focal plane.

A first crude selection criterion was that the maximum peak to peak difference in the arrival time fluctuations should be less than half the period of the transmitted pulse for the weak aberration case. For the strong aberration case this value should be higher than half the period of the transmitted pulse. Based on this crude selection rule, four different body wall models with 2, 4, 6 and 8 time-delay screens respectively, were generated in both the weak and strong aberration category. Both categories thus contained all four sequence configurations, multiplied with a different time-delay amplitude.

One body wall model was then chosen from each of the two categories. The reason for this was to find the body wall model that produced the "worst" aberration in each category respectively. In this procedure the additional selection criterions were applied subjectively. The most important measures of aberration from these criterions were side lobe level in aberrated beam profiles, width of main lobe in aberrated beam profiles, shape distortion and shape deformation of received waveforms, and finally comparison of body wall statistics with measured statistics for human abdominal wall.[11]

The two selected body wall models were denoted w6 and s6, w6 representing the weak aberration category and s6 the strong aberration category. The number indicating that both body wall models contained 6 time-delay screens. The s6 body wall model was intended to represent a case of severe ultrasonic wave aberration. A main point for the s6 wall, was that in addition to all the other selection criterions, the received waveform should be severely shape deformed and the body wall statistics should be very "tough". This means that the rms values of the arrival time and energy level fluctuations should be well above the mean of those reported in Ref. 11, and the correlation lengths in the low region of the reported values.

To summarize: this elaborated process was carried out in order to secure that the two final selected body wall models, w6 and s6, generated aberration comparable to what is observed in ultrasonic imaging. These were also chosen because they represented the worst aberration in their respective categories. Note that simulation results with correction filters from only these two selected body wall models are presented in this article.

II.C Linear angular spectrum propagation operator

The propagation operator used in the simulation program was obtained by the solution of the linear homogeneous wave equation given as

$$\nabla^2 p - \frac{1}{c^2}\frac{\partial^2 p}{\partial t^2} = 0 \quad , \quad p = p(x, z, t) \ , \tag{2.1}$$

where p is the pressure and c is the constant speed of sound. The spatial coordinate x defines the array direction and z the propagation direction (see Fig. 2.1). The Fourier transform with respect to time t and the spatial coordinate x gives the equation of the form

$$\frac{\partial^2 p_{tx}}{\partial z^2} + {k_z}^2 p_{tx} = 0 \quad , \quad k_z = \sqrt{\left(\frac{\omega}{c}\right)^2 - k_x^2} \ , \tag{2.2}$$

where the indices indicate which coordinate that is Fourier transformed. The wave number in the propagation direction is defined as k_z, and k_x represents the wave number in the x-direction. The solution of this equation, with z as the positive propagation direction, can be expressed as

$$p_{tx}(k_x, z, \omega) = p_{tx}(k_x, z_0, \omega)\ e^{-ik_z(z-z_0)} \ , \tag{2.3}$$

where $p_{tx}(k_x, z_0, \omega)$ is the pressure given at $z = z_0$, which represents the array surface in the simulations. The propagation operator is given as $e^{-ik_z(z-z_0)}$, where z is the propagation distance. Note that the propagation operator propagates a two dimensional plane defined by the spatial coordinate x and the time coordinate t, in the propagation direction z. It should also be noted that k_x marks the limit for propagation in the propagation direction. If $\omega/c > k_x$, the operator is complex and represents propagation in the direction of z. If $\omega/c < k_x$ the operator becomes real valued and represents a damping of the wave, but no propagation. This phenomenon is known as evanescent waves.

II.D Correction filters and the generalized frequency-dependent screen

The solution of the wave equation with a point impulse source for an inhomogeneous medium, can be modelled in the frequency domain as[1]

$$g(\mathbf{r}, \mathbf{r}_s; \omega) = s(\mathbf{r}, \mathbf{r}_s; \omega)\ g_h(\mathbf{r} - \mathbf{r}_s; \omega) \ , \tag{2.4}$$

where g is the free-space Green's function in the inhomogeneous medium as a function of the field coordinate $\mathbf{r}$, the source location $\mathbf{r}_s$, and the angular frequency ω. The free-space Green's function for the homogeneous medium g_h is given as

$$g_h(\mathbf{r} - \mathbf{r}_s; \omega) = \frac{e^{-ik|\mathbf{r}-\mathbf{r}_s|}}{4\pi|\mathbf{r} - \mathbf{r}_s|} \ , \tag{2.5}$$

where k is the wave number. Here, $s(\mathbf{r}, \mathbf{r}_s; \omega)$ is the frequency response of a filter producing distortion of the ultrasonic wave as it propagates through the inhomogeneous medium. This

filter is referred to as the generalized frequency-dependent screen, and is composed of a frequency dependent amplitude and phase screen defined as[1]

$$s(\mathbf{r}, \mathbf{r}_s; \omega) = a(\mathbf{r}, \mathbf{r}_s; \omega)\ e^{i\theta(\mathbf{r}, \mathbf{r}_s; \omega)}\ , \tag{2.6}$$

where a and θ are the frequency dependent amplitude and phase screen respectively.

The generalized frequency-dependent screen can be used for correction of the wave distortion from a body wall as a time reversal mirror.[3] Assume that a signal from a point impulse source at $\mathbf{r}_s$, is measured over an array with limited aperture. Because of the reciprocity of the wave equation, retransmitting the time reversed signal received at each point on the array will reproduce the diffraction limited impulse field at $\mathbf{r}_s$. Time reversal of a real signal gives a complex conjugation of the signals temporal Fourier transform. This means that filtering a transmitted signal from an array on each channel with a filter $s^*(\mathbf{r}_a, \mathbf{r}_s; \omega)$, $\mathbf{r}_a$ denotes the array coordinate, is identical to time reversal and will reproduce the diffraction limited impulse field at $\mathbf{r}_s$. The complex conjugate of the generalized frequency-dependent screen thus represents the ideal correction filter for wave distortion.[1]

In the present paper the complex conjugate of the generalized frequency-dependent screen was used as an aberration correction filter along with two approximations of this defined as

$$\begin{aligned} h_1(\mathbf{r}_a, \mathbf{r}_s) &= e^{i\omega\tau(\mathbf{r}_a, \mathbf{r}_s)} \\ h_2(\mathbf{r}_a, \mathbf{r}_s) &= a(\mathbf{r}_a, \mathbf{r}_s)\ e^{i\omega\tau(\mathbf{r}_a, \mathbf{r}_s)}\ , \end{aligned} \tag{2.7}$$

where h_1 is a pure time-delay correction filter, and h_2 is a time-delay and amplitude correction filter.

III Simulation parameters and data processing

The simulation area was 10.24 cm in the x-direction, with a grid size of 0.1 mm. The sampling frequency was 62.4 MHz providing a time window of 16.4 μs. Center frequency of the pulse was 2.5 MHz with a -6 dB bandwidth of 1.6 MHz. The pulse was filtered on transmit with a 4 MHz band pass filter centered around the center frequency of the pulse. An array aperture size of 20 mm with point-like elements was chosen. The focal depth of the array was set to 60 mm (distance $\mathbf{r}_f$ in Fig. 2.1). Water at 37°C was used as the propagation medium. On receive, all signals were corrected for geometric focusing for the homogenous medium before processing of results.

The generalized frequency-dependent screen was estimated by filtering the received signal y with a Wiener-like filter h_W in the frequency domain given by

$$s(\mathbf{r}_a, \mathbf{r}_f; \omega) = h_W(\mathbf{r}_a, \mathbf{r}_f; \omega)\ y(\mathbf{r}_a, \mathbf{r}_f; \omega)\ , \tag{2.8}$$

where $\mathbf{r}_a$ represents the array coordinate and $\mathbf{r}_f$ the focus of the array (see Fig. 2.1). The transfer function for the filter was

$$h_W(\mathbf{r}_a, \mathbf{r}_f; \omega) = \frac{y_t^*(\mathbf{r}_a, \mathbf{r}_f; \omega)}{|y_t(\mathbf{r}_a, \mathbf{r}_f; \omega)|^2 + \frac{max(\ |y_t(\mathbf{r}_a, \mathbf{r}_f; \omega)|^2\ )}{SN}}\ , \tag{2.9}$$

where y_t is the transmitted frequency dependent signal from the point source. The factor SN represents a signal-to noise-ratio parameter in the filter.

The time-delay correction filter approximation of the generalized frequency-dependent screen, defined in section II.D, is identical to the arrival time fluctuations in the received signal, after

correction of geometric focusing for the homogenous medium. Six different methods were used for estimation of arrival time fluctuations. Three of the techniques calculated the angle of the cross-correlation function of the complex envelope at zero lag in the received signal.[17] The difference between them being in the choice of a reference for the calculation of the cross-correlation. The different methods are labeled a, b, c, d, e, f, and this notation will also be used in the presentation of results later in the article.

(a) Phase front tracking: A phase front tracking algorithm was developed as an arrival time fluctuation estimator. In essence the phase front tracking algorithm determined the peak of the first period of the received waveforms. The tracking was then performed on each channel, and the time-delay between two channels was defined as the difference in time between the two peaks of the respective channels.

(b) Neighbor cross-correlation: Cross-correlation technique (as described above) which calculated the cross-correlation of the complex envelopes, at zero lag, between neighboring channels in the receiving array. The total arrival time fluctuations was calculated as the cumulative sum of the time-delays between each neighbor channel, starting from the first channel in the array.

(c) Beamsum cross-correlation: Cross-correlation technique which used a reference signal and calculated the cross-correlation of all the channels at zero lag in the receiving array, with respect to the reference signal. The reference signal was the beamsum of the received signal. The beamsum was defined as the received signal summed over all channels in the array direction, resulting in a time dependent signal only.

(d) Reference channel cross-correlation: Same as (c), but the reference signal was now chosen as the signal at channel nr. 1 in the receiving array.

(e) Frequency mean: Arrival time fluctuations across the receiving array were determined by taking the Fourier transform in time of the received signal on each channel. The time-delay on each channel of the array was calculated as the arithmetic mean of the phase, of the now frequency dependent signal, over a band of frequencies ranging from 2-3 MHz and divided by the center frequency of the transmitted pulse (2.5 MHz). This band was chosen empirically as it produced satisfactory estimates in the weak aberration case.

(f) Ray delays: The last estimator was used as a comparative measure of the performance of the latter described estimators. Since the time-delay of each time-delay screen was known, arrival time fluctuations were calculated by summing the time-delay along a straight line from the focus to a channel on the receiving array.

Amplitude variations across the receiving array were determined in the same fashion as the time-delay estimator (e). The received waveform was Fourier transformed in time. The amplitude on each channel of the array was calculated as the arithmetic mean of the frequency dependent amplitudes over the same band of frequencies.

For the characterization of the different body wall models, leading to the selection of the two generating the most severe aberration, rms values of arrival time and energy level fluctuations were determined along with correlation lengths of these. A linear fit was subtracted from the arrival time fluctuations before the calculation of the correlation lengths and rms values, in order to remove direction steering of the beam by the body wall. The energy level fluctuations were simply defined as the square of the amplitude variations across the receiving array. Correlation lengths were defined as the full width between the half maximum points of the auto-correlation function.

In addition to these measures a waveform similarity factor was determined in order to quantify the extent of waveform deformation in the received signal. Waveform deformation severely complicates time-delay estimation due to low correlation in the received signal. Two similar versions of such a waveform similarity factor[4,18] has been proposed independently. In this article the approach of Liu and Waag[4] was chosen. The similarity of N received waveforms $y_1(t), y_2(t), \ldots, y_N(t)$ is defined to be maximum if

$$y_i(t) = a_i \; y(t - \tau_i) \quad , i = 1, \ldots, N \; , \tag{2.10}$$

where N is the number of elements on the receiving array. From the definition in Eq. 2.10, $y_i(t + \tau_i) = a_i \; y(t)$, must also be true, so that

$$\sum_{i=1}^{N} y_i(t + \tau_i) = \sum_{i=1}^{N} a_i \; y(t) \; . \tag{2.11}$$

Squaring and integrating this equation over time gives

$$\int_{-\infty}^{+\infty} \left(\sum_{i=1}^{N} y_i(t + \tau_i) \right)^2 \mathrm{d}t = \left(\sum_{i=1}^{N} a_i \right)^2 \int_{-\infty}^{+\infty} y^2(t) \mathrm{d}t \; . \tag{2.12}$$

Equation (2.10) gives

$$a_i^2 = \int_{-\infty}^{+\infty} y_i^2(t) \mathrm{d}t \Big/ \int_{-\infty}^{+\infty} y^2(t) \mathrm{d}t \quad . \tag{2.13}$$

Substituting (2.13) into (2.12) gives

$$\int_{-\infty}^{+\infty} \left(\sum_{i=1}^{N} y_i(t + \tau_i) \right)^2 \mathrm{d}t = \left(\sum_{i=1}^{N} \sqrt{\int_{-\infty}^{+\infty} y_i^2(t) \mathrm{d}t} \right)^2 \quad . \tag{2.14}$$

This leads to the definition of the waveform similarity factor r as

$$r = \frac{\sqrt{\int_{-\infty}^{+\infty} \left(\sum_{i=1}^{N} y_i(t + \tau_i) \right)^2 \mathrm{d}t}}{\sum_{i=1}^{N} \sqrt{\int_{-\infty}^{+\infty} y_i^2(t) \mathrm{d}t}} \; . \tag{2.15}$$

Mallart and Fink[18], who independently proposed a focusing criterion C, showed that for a point source the value of C lies between 0 and 1. This also holds for r, but note that r can only be 1 if the τ_i's are selected properly.

Beam profiles in the focal plane of the array were calculated as the rms value in time of each spatial position. These profiles were used as visual characterization of the aberration caused by the two established body wall models. They were also used for the visual evaluation of the effect of the different aberration correction filters.

Additional evaluation of the aberration correction was performed by analysis of the focus quality of the transmitted aberration corrected beam. Liu and Waag[19] have developed a method for evaluation of the focus quality of a transmitted beam. This method was also used here. A brief explanation of this method, as described in Ref. 19, is given here. As described in section II.C, the signal that is propagated has a spatial (array direction) and temporal dimension. The method calculates the envelope of the analytic signal in the focal plane, thus obtaining a two dimensional matrix of positive numbers which can be used for various focal quality measures. A first measure

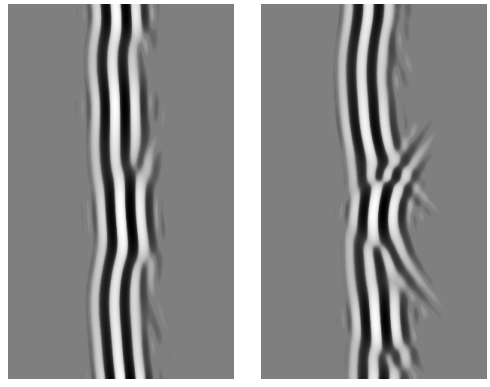

(a) w6 case (b) s6 case

Figure 2.3: Received waveforms after correction of geometric focusing for the homogenous medium. Each pane shows a temporal logarithmic gray scale picture of the waveforms at the receiving array. The dynamic range of the logarithmic scale is 40 dB. The horizontal axis represents time and spans 4.8 μs and the vertical axis represents the receiving array and spans 20 mm. The left pane shows the waveform received after propagation through the w6 body wall model and the right pane shows the waveform from the s6 body wall model.

is obtained by projection of the maximum value of the analytic envelope amplitudes in both the array and time direction. This provides one-dimensional amplitude profiles in both these directions. Effective widths of these profiles were found at -10 dB below the peak value. The effective width of such a profile was defined as the square root of the product of the radius in each direction of the profile, at the -10 dB level from the peak. A measure denoted the effective diameter was then calculated as the square root of the product of the effective widths in each direction. The effective diameter is hence the diameter of a circle with the same area as an ellipse defined by the effective widths in space and time. This provided a measure of the size of the focus at -10 dB from the peak value. The effective widths were also used in the evaluation of the -10 dB peripheral energy ratio. An ellipse was specified with axes equal to half of the effective widths in space and time, defining a central and peripheral region of the signal. The -10 dB energy ratio was then calculated as the energy outside the ellipse to the energy inside it. These measures, in combination with visual inspection of the beam profiles in the focal plane, gave substantial information of the focus quality of the corrected beam.

IV Results

Figure 2.3 shows the received waveforms after correction of geometric focusing for the homogenous medium. The left pane shows the weak aberration case and the right pane the strong aberration case. Shape distortion of the waveform is clearly visible, and in the strong aberration case deformation of the waveform also occurs in several places. This was, as earlier described, one of the main selection criterions for the strong aberration body wall model as a case of severe aberration. Since the waveforms are pictured with a logarithmic scale and a dynamic range of 40 dB, amplitude variations do not show. Table 2.1 shows the statistical properties and the waveform similarity factors for the four body wall models in each class (weak and strong), where the w6 and s6 wall are shown in boldface. The values for the arrival time

Table 2.1: Body wall models statistics and waveform similarity factors (WSF).

	Arrival time fluctuations		Energy level fluctuations		WSF
Wall model	rms value (ns)	Corr. len. (mm)	rms value (dB)	Corr. len. (mm)	(*1e-3)
w2	36.0	2.8	2.9	1.6	971
w4	37.5	2.8	2.4	1.6	984
w6	**49.4**	**3.0**	**3.1**	**1.8**	**975**
w8	47.7	3.0	2.5	2.2	992
s2	39.6	2.8	3.6	2.0	957
s4	54.5	3.4	4.0	2.0	924
s6	**53.7**	**2.4**	**4.1**	**1.4**	**914**
s8	69.8	4.0	3.8	1.8	949

fluctuations are based on the phase front estimation method (a). The rms values of the arrival time fluctuations for the w6 and s6 wall are well above the mean value of those reported by Hinkelman *et al.*[11] Especially the energy level fluctuations for the s6 wall model are higher than any of the reported values. Correlation lengths for the arrival time and energy fluctuations are well below the mean of the reported values for both w6 and s6. The waveform similarity factors have been calculated after correction for geometric focusing and aberration correction with the phasefront tracking algorithm. If compared to the received waveform, the phase front tracking method shows a very accurate representation of the time-delay variation of the wavefront. For the w6 wall the waveform similarity is quite high, indicating low level of wave deformation which also can be seen in Fig. 2.3 (a). The waveform similarity for the s6 wall on the other hand is quite low quantifying the amount of waveform deformation clearly visible in Fig. 2.3 (b). Figure 2.4 shows the estimated arrival time fluctuations for the weak aberration case (w6 body wall model). Figure 2.4 (a) shows the arrival time fluctuations as determined by the phase front tracking algorithm. This has been used as a reference in the other plots, indicated by a dotted line, for comparison of the estimated arrival time fluctuations to the actual time-delay variation of the phase front. The figure shows that the different estimation methods produce very similar results for the weak aberration case.

Table 2.2 shows the normalized L^2-norm between the arrival time fluctuation estimation methods, where the phase front tracking method (a) serves as the reference. The table shows that there are some deviations between the frequency mean method (e), the different cross-correlation techniques (b), (c), (d) and the time-delay variation of the phase front, but they are relatively small. The ray delays method (f) and the arrival time fluctuations of the phase front are almost identical in this case. It must be emphasized that (f) is not an estimation method, but is merely used as a qualitative measure of the arrival time fluctuations.

In Fig. 2.5 the arrival time fluctuation estimates from the strong aberration case is presented. In this case several of the arrival time fluctuation estimation methods fail to estimate the time-delay variation of the phase front of the received waveform. The neighbor cross-correlation method (b) and the frequency mean method (e), show large deviations in the estimates and the L^2-norm is large. The beamsum cross-correlation method (c) shows "jumps" in the estimates. By closer inspection these deviations and "jumps", all occur in the shape deformed region of the

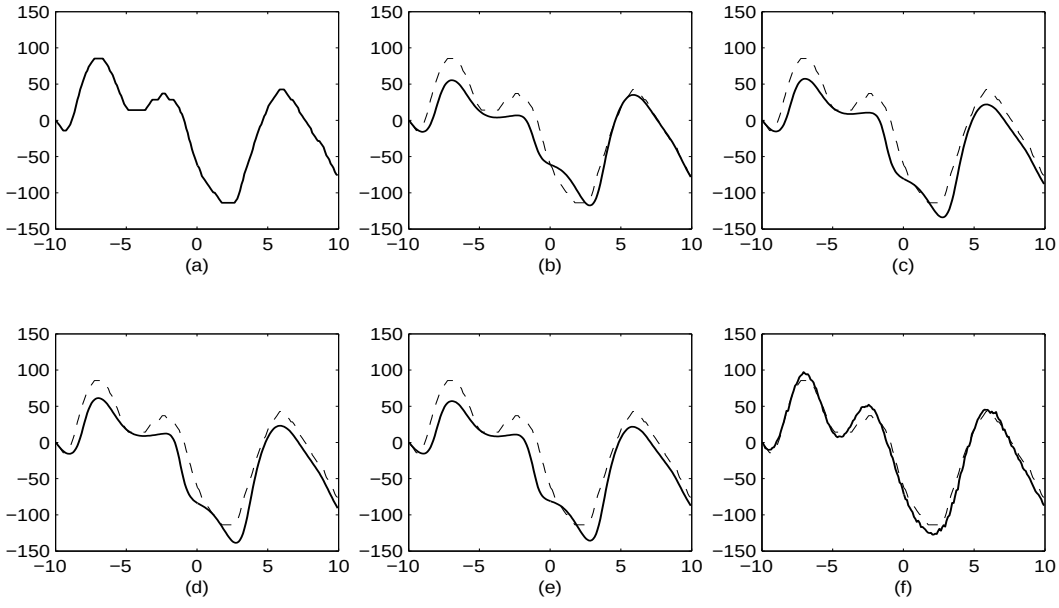

Figure 2.4: Arrival time fluctuation estimates from the w6 wall model. The notation (a), (b) etc. in the different panes of the figure follows the notation introduced for the different arrival time estimators in Section III. The horizontal axis represent the array direction (mm), and the vertical axis the time-delays (ns). For the horizontal axis, zero represents the center of the array and -10 mm the first channel in the array, which was used as reference for the reference channel cross-correlation method (d), and starting point of the cumulative summation in method (b). In each figure the solid line represents the estimate, and the dotted line the arrival time fluctuations of the phase front method (a), which is only plotted as a reference.

Table 2.2: Normalized L^2-norm. The L^2-norm between the phase front tracking method (a) and all the other methods for both the weak and strong aberration case, where the L^2-norm is normalized with respect to (a).

w6 case		s6 case	
Method	L^2	Method	L^2
(a)	0.0	(a)	0.0
(b)	0.34	(b)	0.98
(c)	0.40	(c)	0.45
(d)	0.39	(d)	0.28
(e)	0.42	(e)	1.43
(f)	0.17	(f)	0.33

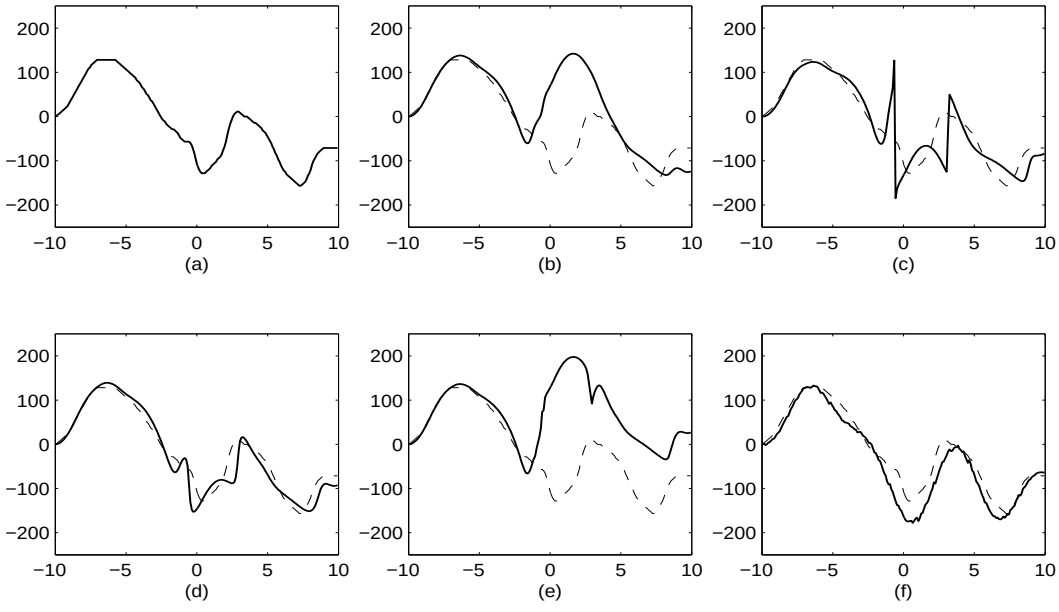

Figure 2.5: Arrival time fluctuation estimates from s6 wall. The same notation as in Fig. 2.4 is used.

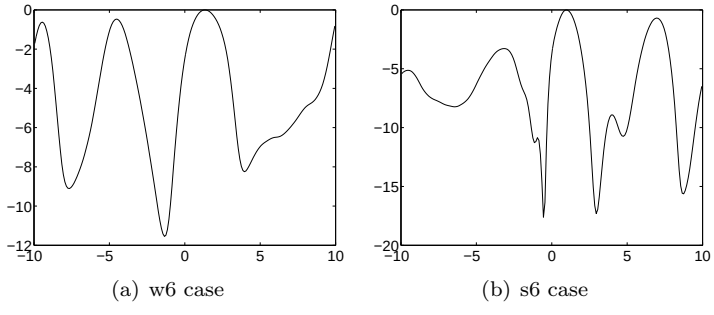

Figure 2.6: Amplitude variations across the receiving array for the weak and strong aberration cases. The horizontal axis represent the array direction (mm) and the vertical axis the amplitude (dB).

received waveform. The reference channel cross-correlation method (d), estimates the time-delay variations very well, but also here the estimates shows smaller "jumps" in the shape deformed region of the received waveform. There are only smaller variations in the L^2-norms for method (c), (d), and (f).

Amplitude variations across the receiving array for the weak and strong aberration cases are presented in Fig. 2.6. In the strong aberration case amplitude variations of approximately 18 dB are observed.

Figure 2.7 shows beam profiles corrected with the generalized frequency-dependent correction filter for both the weak and strong aberration case. This is the best correction obtainable with a transmit correction filter of any kind, and the correction is very close to the ideal case. Table 2.3 presents the results of the focus quality calculations as described in Section III. These values

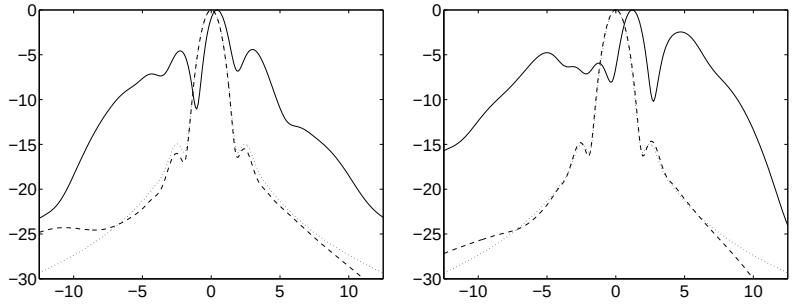

(a) w6 (b) s6

Figure 2.7: Beam profiles corrected with generalized frequency-dependent correction filter. Left pane shows the weak aberration case and the right pane the strong aberration case. The horizontal axis represents the focal plane (mm) and the vertical axis the energy (dB). The solid line represents the aberrated profile, the dashed line the corrected profile and the dotted line the profile with no aberration, which serves as a reference. The zero point on the horizontal axis denotes the center axis of the transmitting array. All profiles are normalized to their maximum value.

give a more detailed description of what is observed in the beam profiles as time [which is the same as depth in the z-direction (see Fig. 2.1] is also included. It must be stressed that the focus quality variables in Table 2.3 can not be directly linked to the presented beam profiles, as they are calculated in a different way. After correction with the generalized frequency-dependent correction filter, the peripheral energy ratios are almost identical to the ideal case even if the effective widths are slightly higher.

Beam profiles in the focal plane after correction with a time-delay correction filter for the weak aberration case are shown in Fig. 2.8. The aberrated profiles show side lobe level of -5 dB from the peak value, and the profile is quite wide. Since the arrival time fluctuation estimates for the weak aberration case are very similar, only small differences in the different corrected profiles are visible. By visual inspection of the beam profiles, a general reduction of about 10 dB in the strongest side lobes is obtained with the time-delay correction filter. Further away from the central axis the correction is less substantial. The effective widths at -10 dB in space and time is identical to the ideal case, but the peripheral energy ratio is relatively high, because the side lobe level is still high in comparison to the ideal case. Note that the ray delays method (f) gives the poorest correction.

Beam profiles corrected with a time-delay and amplitude correction filter for the weak aberration case, are presented in Fig. 2.9. Now the strongest side lobes are reduced to the side lobe level of the non-aberrated profile, and a strong reduction in the side lobe level further away from the central axis can be noticed. Also here the effective widths in Table 2.3 at -10 dB are very close to the ideal case. The -10 dB peripheral energy ratios with time-delay and amplitude correction are very close to the ideal case, and almost half the value of time-delay correction only. The peripheral energy ratios for the phase front tracking method (a) and the ray delays method (f), are somewhat higher than for the other methods.

Figure 2.10 shows beam profiles with time-delay correction for the strong aberration case. Now the aberrated profile is severely distorted and very wide. As shown in Fig. 2.5, the estimation neighbor cross-correlation method (b) and the frequency mean method (e), fail to predict the arrival time fluctuations of the wave front, and they produce little or no correction at all. The other methods perform rather well, especially the beamsum and reference channel cross-

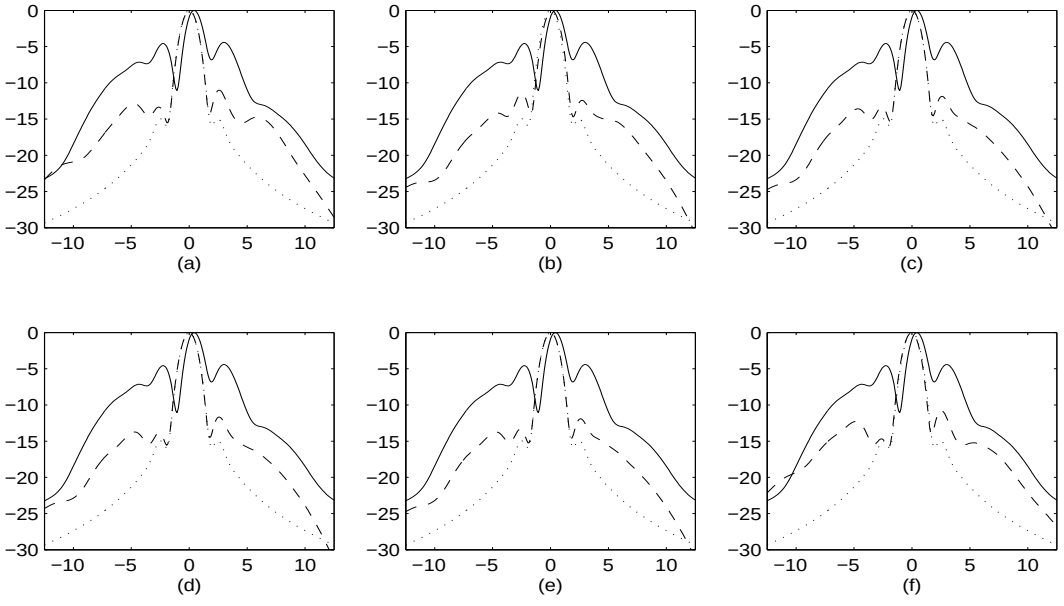

Figure 2.8: Beam profiles in the focal plane corrected with a time-delay correction filter for the weak aberration wall model. Same notation as in Fig. 2.7.

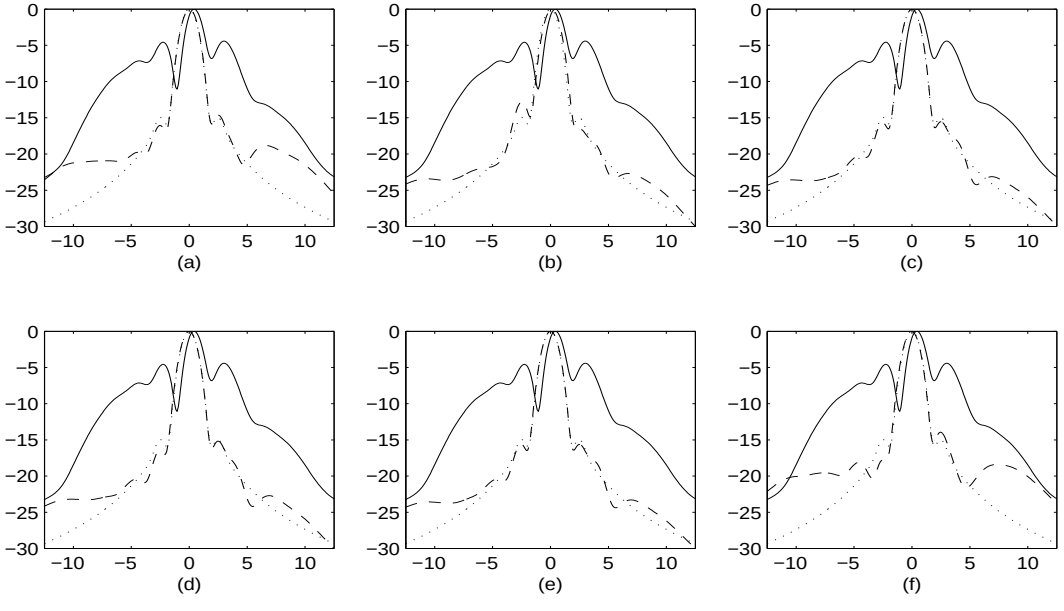

Figure 2.9: Beam profiles in the focal plane corrected with a time-delay and amplitude correction filter for the weak aberration wall model. Same notation as Fig. 2.7.

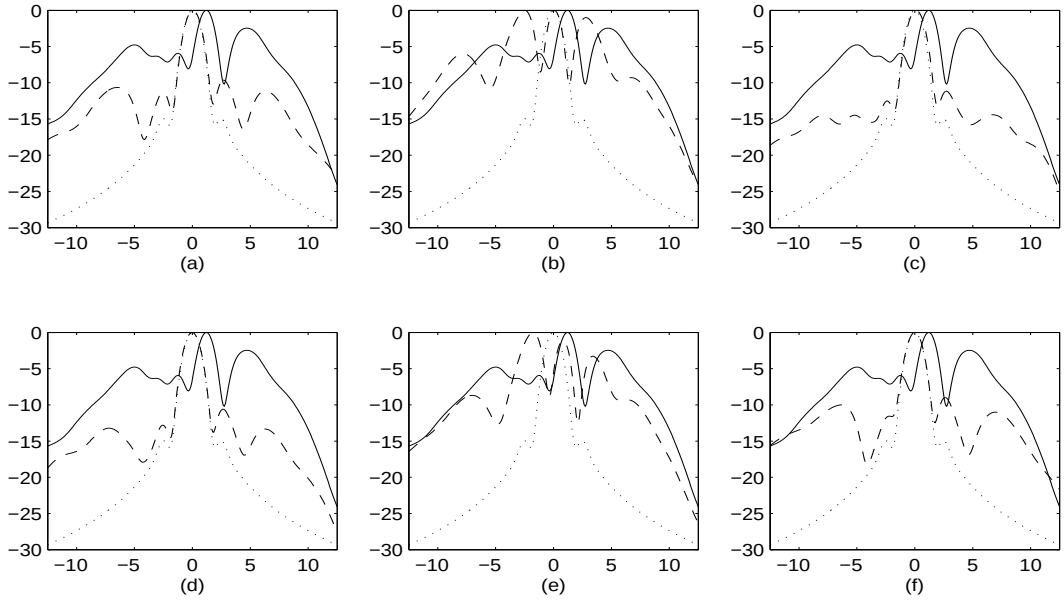

Figure 2.10: Beam profiles with time-delay correction for the strong aberration wall model. Same notation as Fig. 2.7.

correlation methods (c) and (d), but it is quite obvious that this is a more difficult case. From table 2.3 the -10 dB peripheral energy ratios are somewhat higher for this case than for the weak aberration case, even if the effective widths have not increased much. It should be noted that there is great uncertainty about the focus quality parameters of method (b) and (e) as there is no clearly defined main lobe. This poses problems for the calculation of the effective widths. The same argument holds for the aberrated profiles. It should also be pointed out that even if there is only a small difference in the L^2-norm between method d) and the ray delays method (f), the difference in the -10 dB peripheral energy ratio is large.

Beam profiles with time-delay and amplitude correction are shown in Fig. 2.11. Now the correction is quite substantial with all methods except (b) and (e). The focus quality parameter in table 2.3 show that the beamsum cross-correlation and reference channel methods (c) and (d), perform very well also for the strong aberration case. With time-delay and amplitude correction the peripheral energy ratios with these methods are very close to those for the weak aberration case (and thus the ideal case), indicating their robustness. Notice that even if method (c) has "jumps" in the arrival time fluctuations estimates, it still performs quite well. Notice also that the peripheral energy ratio for method (f) is almost double the value of method (d), even if the differences in the estimated arrival time fluctuations are relatively small (see Fig. 2.5). This indicates the sensitivity of the arrival time estimate and illustrates the importance of a proper estimate.

V Discussion

Several studies have modelled the human body wall with single or multiple time-delay screens.[4,6,8–10] Some of these have used measured or estimated human body wall statistics

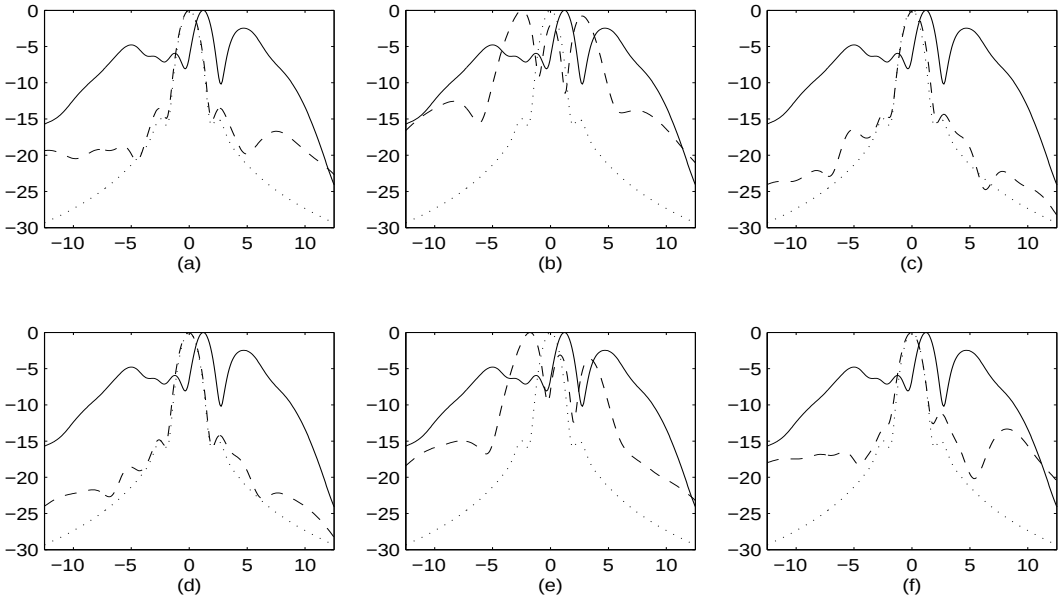

Figure 2.11: Beam profiles with time-delay and amplitude correction for the strong aberration wall model. Same notation as Fig. 2.7.

as a basis for a realization of a simple random distribution, used as a time-delay aberration screen. Usually the statistics are rms values and correlation lengths of arrival time and amplitude fluctuations. In Ref. 16, such models are criticized on the basis that even if they produce wave distortion with statistics similar to the human body wall, they are not truly able to reproduce human body wall aberration. This is simply due to the fact that a body wall does not represent a true random medium, and that it is the tissue structure of the wall that introduces the aberration. An example of this is connective tissue aligned close to the propagation direction in the subcutaneous fat layer. As demonstrated by Mast *et al.*, this structure causes scattering of energy and generates arrival time fluctuations that increase cumulatively with propagation through the fat layer.[16] The use of time-delay screen models are thus criticized not to account for aberrations created by the subcutaneous fat layer, and that they are more appropriate for describing aberration caused by muscle layers.[16] Mast *et al.* show that muscle layers mainly introduce phase distortion and weak amplitude distortion, and that amplitude distortion basically originates from the inhomogeneities in the subcutaneous fat layer.[16]

In this article the body wall statistics has only been one of several criterions in the making of the body wall models. A selection of eight normally distributed random sequences were combined, filtered and tuned to obtain eight different body wall models. Then a careful selection of two specific wall models among the eight was performed. The selection criterions were visual inspection of gray scale pictures of received waveforms, calculation of body wall statistics and waveform similarity factors, visual evaluation of arrival time fluctuations and amplitude variations, and evaluation of aberrated beam profiles in the focal plane. The body wall statistics were compared with similar statistics as measured correlation lengths for the human abdominal wall.[11] This evaluation was performed in order to select two body wall models that produced weak and strong aberration respectively. As seen from Table 2.1 the w6 body wall model has the toughest body wall statistics in the weak category even if the waveform similarity is somewhat

Table 2.3: Table of focus quality with respect to applied correction method. The peripheral energy ratio (PER) and all effective widths have been calculated at -10 dB level from the peak. The two column headings refers to the weak and strong aberration cases respectively. The first column indicates which time-delay fluctuation estimation method that is used. The second column specifies the type of correction where τ denotes time-delay correction, and τ&a time-delay and amplitude correction. The parameters d_e, w_a, and w_t denotes the effective diameter, the effective width in the array direction, and the effective width in the time direction respectively. The three lowest rows have no value in the second column. The first of these rows show the correction with the generalized frequency-dependent correction filter, the second show the aberrated case and the third show the ideal case with no aberration.

w6 case						s6 case					
		PER	d_e (mm)	w_a (mm)	w_t (mm)			PER	d_e (mm)	w_a (mm)	w_t (mm)
(a)	τ	0.486	1.84	2.70	1.26	(a)	τ	0.797	1.84	2.80	1.21
(b)	τ	0.446	1.84	2.70	1.26	(b)	τ	2.370	3.16	4.70	2.13
(c)	τ	0.426	1.84	2.70	1.26	(c)	τ	0.575	1.91	2.90	1.26
(d)	τ	0.426	1.84	2.70	1.26	(d)	τ	0.579	1.88	2.80	1.26
(e)	τ	0.426	1.84	2.70	1.26	(e)	τ	0.850	3.51	5.90	2.13
(f)	τ	0.518	1.84	2.70	1.26	(f)	τ	0.932	1.91	2.90	1.26
(a)	τ&a	0.301	1.84	2.70	1.26	(a)	τ&a	0.393	1.91	2.90	1.26
(b)	τ&a	0.264	1.88	2.80	1.26	(b)	τ&a	1.140	3.31	6.00	1.82
(c)	τ&a	0.242	1.88	2.80	1.26	(c)	τ&a	0.288	1.91	2.90	1.26
(d)	τ&a	0.242	1.82	2.80	1.26	(d)	τ&a	0.273	1.91	2.90	1.26
(e)	τ&a	0.242	1.88	2.80	1.26	(e)	τ&a	1.170	2.50	3.70	1.69
(f)	τ&a	0.331	1.84	2.70	1.26	(f)	τ&a	0.544	1.94	3.00	1.26
filter		0.220	1.87	2.70	1.30	filter		0.210	1.84	2.70	1.26
abb		1.220	2.58	4.50	1.47	abb		1.430	3.68	6.50	2.08
ideal		0.227	1.84	2.70	1.26	ideal		0.227	1.84	2.70	1.26

higher than the w2 wall. When comparing all the above mentioned criterions the w6 model still came out as the worst in its category. In the strong category, the s8 wall has very high rms value of the arrival time fluctuations, but a relatively high correlation length and waveform similarity factor. This makes arrival time estimation easier, and this in combination with the other criterions is why the s6 wall was preferred as a case of severe aberration.

A close inspection of arrival time fluctuations for the weak and strong aberration case (Fig. 2.4 and Fig. 2.5), show variations that can be interpreted as cumulative time-delays resulting from propagation through larger or smaller structures. A comparison of the time-delay screens for these two cases with the arrival time fluctuations obtained with time-delay estimator (f), *i.e.* summing the time-delay along a straight line from the focus to a channel on the receiving array, showed that the specific variations did not stem from a single strong time-delay screen alone. Large variations were results of high correlation between all six time-delay screens in the direction of summation, smaller variations were results from lower correlation. These observations indicate that the w6 and s6 model walls do model correlated structures of different sizes. A structure such as connective tissue aligned close to the propagation direction in the subcutaneous fat layer, would result in a large drop in amplitude level over a small region on the receiving array. The amplitude variation of the s6 model wall [Fig. 2.6 (b)], show this type of amplitude variation. An amplitude drop of about 18 dB is observed, which is close to what observed in

Ref. 16.

The waveform similarity factor was only used to quantify the amount of waveform deformation in the received signals. As explained in Section IV, the waveform similarity factor was calculated after correction for geometric focusing and aberration correction with the phasefront tracking algorithm. Since the factor is dependent on the selected time-delays τ_i [see Eq. (2.15), Section III], it is dependent of the arrival time estimation method. In this article simulations were performed with point sources without noise, and the phase front tracking algorithm will in this situation always give a reliable estimate of the time-delay variation of the wavefront since it is clearly defined. The method proved to give an accurate estimate of the time-delay variation of the received wavefront, giving a very good focusing of the received signal. This means that variations in the waveform similarity factor in Table 2.1 is only due to the difference in waveform deformation of the received aberrated signal, and thus gives an accurate quantification of the waveform deformation. Note that in a more realistic situation, with interference from multiple scatterers and acoustic and electronic noise, the phasefront tracking method will probably be less accurate since there no longer exists an evident wavefront.

A weakness in the simulations was that absorption effects were not included. Mast *et al.* have shown that both absorption and scattering effects makes a significant contribution to the total insertion loss in the human body wall.[16] They suggest that estimation of attenuation by the human abdominal wall for correction of amplitude aberration, should consider both scattering and absorption effects. They indicate that scattering accounts for about 36% of total insertion loss in the human abdominal wall at 3.75 MHz.[16] Attenuation of the amplitudes by absorption would probably deteriorate the amplitude correction.

In both the weak and strong aberration case, correction with a generalized frequency-dependent correction filter produced very close to ideal correction. For the weak aberration case the different arrival time fluctuation estimators all performed well. In the strong aberration case both neighbor cross-correlation method (b), and the frequency mean method (e), failed severely. This is obviously due to the waveform deformation in this case, which also caused problems for the beamsum and reference channel cross-correlation methods [(c) and (d)]. In Fig. 2.5, it is clearly visible that the reference channel cross-correlation method encounters problems in the same region as the cross-correlation beamsum method, but they are less severe. This indicates that the choice of reference is of importance in cross-correlation techniques, where strong waveform distortion and deformation occurs. On the other hand these methods perform rather well despite of the problems. This can be explained by comparing the "jumps" in the estimates with the methods (c) and (d), and the amplitude variation for the strong aberration case [Fig. 2.6 (b)]. The large drops in the amplitude variation corresponds with the regions where the waveform is deformed [Fig. 2.3 (b)]. The "jumps" in the arrival time fluctuation estimates occurs in the exact same places as the amplitude drops, due to the waveform deformation. Therefore the "jumps" in the arrival time fluctuation estimates do not influence the correction, because the amplitudes are negligible in these regions on transmit. It is also worth commenting that arrival time fluctuations obtained with the phase front tracking algorithm do not produce the best aberration correction, although this could be expected intuitively since this method gives the actual time-delay variation of the wavefront. This is just a statement of the difficulty of properly defining the time-delay between two signals in ultrasonic imaging.

The peripheral energy ratios, after correction with the generalized frequency correction filter, are actually somewhat better than the ideal non-aberration situation for both body wall models. This is probably due to the Wiener-like filtering process that is performed to obtain the generalized frequency correction filter. When the filter is applied on transmit, it slightly changes the transmitted pulse, and in this case this results in lower peripheral energy ratios than the ideal situation.

The differences in the L^2-norms should also be commented further. For the weak aberration case, the ray delays method (f) has more than half the L^2-norm compared to beamsum cross-correlation method (c), but the peripheral energy ratio is higher. For the strong aberration case there are only smaller differences in the L^2-norms between method (c), (d) and (f). Still the peripheral energy ratio of the ray delays method (f), is almost double the value of both method (c) and (d). This indicates that in some cases, the effect of the correction can be very sensitive to how the arrival time fluctuations are estimated. Relatively small differences in the arrival fluctuation estimates can give large variations in the focus spot size of the corrected beam.

VI Conclusions

Different correction filters for ultrasonic wave aberration have been investigated. The results in this article indicate that correction of aberration of the transmit beam with a time-delay and amplitude correction filter, produce substantial correction of the focus quality. Correction with a time-delay filter alone performed poorer than correction with a time-delay and amplitude filter, but improved focus quality considerably. Two cases were studied, a weak and strong aberration case, were the strong aberration case represented a case of severe wave aberration. For both cases correction with a time-delay and amplitude filter gave results close to the ideal unaberrated case, indicating that this correction method is very robust. The main criterion for this method to work, was that the arrival time fluctuations were estimated correctly. Six different arrival time estimation methods were investigated. The best result was obtained with a method that calculated the cross-correlation at zero lag of the complex envelope of the received signal, with a reference signal. Two reference signals were tested: the beamsum and a signal from a channel on the transducer. The two different references produced approximately the same aberration corrections, even if there were some differences in the estimated arrival time fluctuations.

Acknowledgments

The work presented in this article was supported by the Medicine and Health program of the Research Council of Norway.

References

[1] B. Angelsen, *Ultrasound imaging. Waves, signals and signal processing.* Trondheim: Emantec, 2000, vol. II, http://www.ultrasoundbook.com.

[2] S. W. Flax and M. O'Donnell, "Phase-aberration correction using signals from point reflectors and diffuse scatterers: Basic principles," *IEEE Trans. Ultrason. Ferroelectr. Freq. Control*, vol. 35, no. 6, pp. 758–767, November 1988.

[3] M. Fink, C. Prada, F. Wu, and D. Cassereau, "Self focusing in inhomogeneous media with "Time Reversal" acoustic mirrors," *Ultrasonics Symposium, 1989 Proceedings, IEEE 1989*, pp. 681–686, 1989.

[4] D.-L. Liu and R. C. Waag, "Correction of ultrasonic wavefront distortion using backpropagation and a reference waveform method for time-shift compensation," *J. Acoust. Soc. Am.*, vol. 96, no. 2, pp. 649–660, August 1994.

[5] J. C. Lacefield and R. C. Waag, "Evaluation of backpropagation methods for transmit focus compensation," *Ultrasonics Symposium, 2001 IEEE*, vol. 2, pp. 1495–1498, 2001.

[6] A. P. Berkhoff and J. Thijssen, "Correction of concentrated and distributed aberrations in medical ultrasound imaging," *1996 IEEE Ultrasonics Symp. Proc.*, vol. 2, pp. 1405–1410, 1996.

[7] M. O'Donnell and S. W. Flax, "Phase-aberration correction using signals from point reflectors and diffuse scatterers: Measurements," *IEEE Trans. Ultrason. Ferroelectr. Freq. Control*, vol. 35, no. 6, pp. 768–774, November 1988.

[8] L. A. Ødegaard, "Using signals scattered from diffuse inhomogeneities to correct for phase aberrations caused by a phase-screen far from the transducer," *IEEE Ultrasonics Symp. Proc.*, vol. 2, pp. 1443–1447, 1995.

[9] S. Krishnan, P.-C. Li, and M. O'Donnell, "Adaptive compensation of phase and magnitude aberrations," *IEEE Trans. Ultrason. Ferroelectr. Freq. Control*, vol. 43, no. 1, pp. 44–55, January 1996.

[10] W. F. Walker and G. E. Trahey, "Aberrator integration error in adaptive imaging," *IEEE Trans. Ultrason. Ferroelectr. Freq. Control*, vol. 44, no. 4, pp. 780–791, July 1997.

[11] L. M. Hinkelman and D.-L. Liu, L. A. Metlay, and R. C. Waag, "Measurements of ultrasonic pulse arrival time and energy level variations produced by propagation through abdominal wall," *J. Acoust. Soc. Am.*, vol. 95, no. 1, pp. 530–541, January 1994.

[12] L. M. Hinkelman and D.-L. Liu, R. C. Waag, and Q. Zhu and B. D. Steinberg, "Measurement and correction of ultrasonic pulse distortion produced by the human breast," *J. Acoust. Soc. Am.*, vol. 97, no. 3, pp. 1958–1969, March 1995.

[13] L. M. Hinkelman, T. L. Szabo, and R. C. Waag, "Measurements of ultrasonic pulse distortion produced by human chest wall," *J. Acoust. Soc. Am.*, vol. 101, no. 4, pp. 2365–2373, April 1997.

[14] T. Douglas Mast, Laura M. Hinkelman, and Michael J. Orr, V. W. Sparrow, and R. C. Waag, "Simulation of ultrasonic pulse propagation through the abdominal wall," *J. Acoust. Soc. Am.*, vol. 102, no. 2, pp. 1177–1190, August 1997.

[15] L. Hinkelman, T. D. Mast, L. A. Metlay, and R. C. Waag, "The effect of abdominal wall morphology on ultrasonic pulse distortion. part i. measurements," *J. Acoust. Soc. Am.*, vol. 104, no. 6, pp. 3635–3649, December 1998.

[16] T. D. Mast, L. M. Hinkelman, M. J. Orr, and R. C. Waag, "The effect of abdominal wall morphology on ultrasonic pulse distortion. part ii. simulations," *J. Acoust. Soc. Am.*, vol. 104, no. 6, pp. 3651–3664, December 1998.

[17] M. O'Donnell and W. E. Engeler, "Real-time phase aberration correction system for medical ultrasound imaging," *Annual International Conference of the IEEE Engineering in Medicine and Biology Society*, vol. 12, 1990.

[18] R. Mallart and M. Fink, "Adaptive focusing in scattering media through sound-speed inhomogeneities: The van Cittert Zernike approach and focusing criterion," *J. Acoust. Soc. Am.*, vol. 96, no. 6, pp. 3721–3732, December 1994.

[19] D.-L. Liu and R. C. Waag, "Time-shift compensation of ultrasonic pulse focus degradation using least-mean-square error estimates of arrival time," *J. Acoust. Soc. Am.*, vol. 95, no. 1, pp. 542–555, January 1994.

Chapter 3

Estimation of ultrasound wave aberration with signals from random scatterers

S. Måsøy[1], T. Varslot[2], B. Angelsen[1]
1)Department of Circulation and Imaging, NTNU
2)Department of Mathematical Sciences, NTNU.

A method for estimating waveform aberration from random scatterers in medical ultrasound imaging has been derived and its properties investigated using two-dimensional simulations. The method use a weighted and modified cross-spectrum in order to estimate arrival time and amplitude fluctuations from received signals. The arrival time and amplitude fluctuations were used in a time-delay, and a time-delay and amplitude aberration correction filter, for evaluation of the re-transmitted aberration corrected signal. Different types of aberration have been used in this study. First, aberration was concentrated on the plane of the transmitting/receiving array. Second, aberration was generated with a distributed aberrator. Both conditions emulated aberration from the human abdominal wall. Results show that for the concentrated aberrator, arrival time and amplitude fluctuations were estimated in close agreement with reference values. The reference values were obtained from simulations with a point source in the focal point of the array. Correction of the transmitted signal with a time-delay, and a time-delay and amplitude filter produced approximately equal correction as with point source estimates. For the distributed aberrator, the estimator performance degraded significantly. Arrival time and amplitude fluctuations deviated from reference values, leading to a limited correction of the re-transmitted signal.

I Introduction

Aberration in medical ultrasound imaging, mainly due to the inhomogeneities in the human body wall, enlarges the insonified scatterer region because of a defocusing of the transmitted beam. [1–6] This effect blurs the ultrasound image and reduces the physicians ability to make an accurate diagnosis.

There are two main objectives of this article.

1. Investigate a method developed for estimating arrival time and amplitude fluctuations using signals from random scatterers.

2. Test the estimator under two different aberration situations. First, a concentrated aberrator where all aberration is concentrated to a plane on the transmitting/receiving array. Second, a distributed aberrator with a specified thickness. Both aberration situations emulated the human abdominal wall.

Aberration correction is often based on estimating arrival time, or arrival time and amplitude fluctuations, which are used as a correction filter on transmit of the ultrasonic signal.[1,3,6–12] This method is here referred to as a time-delay, or a time-delay and amplitude aberration correction filter.

The time reversal mirror introduced by Fink *et al.*,[13] requires a point source in the insonified medium, which rarely is the case in an imaging situation. Liu and Waag introduced a back-propagation method which propagates the signal homogeneously backwards in time in order to obtain an optimal situation for estimation of a time-delay screen.[14] It is not yet sure if this method performs better for transmit correction than time-delay correction estimated at the array surface.[15] In Ref. 12 it was shown that if arrival time and amplitude fluctuations in the received signals are accurately estimated, they will produce close to ideal aberration correction when used as a time-delay and amplitude correction filter on transmit.

Aberration correction is a filter process which inherently assumes the receive aberration, on a given array element, to be independent of the spatial position of the reflecting scatterer. The aberration correction filter thus assumes all aberration of the heterogeneous medium to be concentrated in a plane on the array surface. An approximation to this situation would be for the aberration to be generated in a thin layer just in front of the array.

Assuming all aberration to be concentrated in a plane, is often denoted a concentrated aberrator or an aberrating screen in the literature. For a concentrated aberrator at the array surface this notation is not precise enough. In this article, the situation where a concentrated aberrator is situated at the array surface is denoted receive scatterer independent aberration, or simply scatterer independent aberration. The reason for this is that placing an aberrating screen some distance from the array, would not lead to a situation where aberration at a receive array element is independent on the scatterers position in space.

Scatterer independent aberration is an approximation to the more general and physical case where the aberrated receive signal, on a given array element, is expected to be dependent on the scatterers spatial position. This is because different types of aberration is generated in different parts of the human body wall, that is, over the whole thickness of the body wall.[5,16] Since body wall thickness and anatomy varies strongly between humans, this also implies that the degree to which aberration on receive will be scatterer dependent, also varies.

There exists a region of scatterers, for which the aberration (at a given array element) in a signal received from any scatterer inside this region, is practically the same. This region is termed an isoplanatic patch, a term coined in astronomy where aberration effects occur when light from stars pass through the atmosphere. By the definition of the isoplanatic patch, focusing the transmitted beam to the inside of the patch, leads to receive scatterer independent aberration even for a thick or extended aberrator. Remark that the isoplanatic patch size change with a change in the location of the array focus.

Based on the previous discussion, the results in this article show the difference of scatterer independent and scatterer dependent aberration. This information is important in understanding how these different aberration situations influence the estimation of arrival time and amplitude fluctuations.

Three simulation situations were studied to evaluate the developed estimation method for arrival time and amplitude fluctuations, and the performance of the time-delay, and the time-delay and amplitude aberration correction filter:

1. **Scatterer independent aberration (SIA):** Simulations have been performed were all the aberration is concentrated in a plane on the transmitting/receiving array. This represents a situation were the simulated data concurs with the aberration estimation/correction method.

2. **Scatterer dependent aberration (SDA):** This represents a realistic aberration situation. Now the underlying assumption for the correction method is not fulfilled, and the object is to test its validity.

3. **Scatterer dependent aberration with a corrected transmit beam (CSDA):** This is the same situation as in (2), but now the transmitted beam is corrected with a time-delay and amplitude filter estimated from a point source. The motivation for this was to show that a well estimated time-delay and amplitude correction filter leads to scatterer independent aberration, because the energy of the corrected retransmitted beam is focused to the inside of the isoplanatic patch.

Absorption effects and electronic/acoustic noise were not included in the simulations.

II Theory

II.A The generalized frequency-dependent screen and the time-delay and amplitude correction filter

In Ref. 12 the Green's function for a heterogeneous medium was modeled in the frequency domain as

$$g(\mathbf{r}, \mathbf{r}_s; \omega) = s(\mathbf{r}, \mathbf{r}_s; \omega)\ g_h(\mathbf{r} - \mathbf{r}_s; \omega), \tag{3.1}$$

where g is the Green's function in the heterogeneous medium as a function of the field coordinate $\mathbf{r}$, the source or scatterer location $\mathbf{r}_s$, and the angular frequency ω. Here g_h is the Green's function for the homogeneous medium.

Propagation in an heterogeneous medium generates interference, which results in an aberrated signal. Interference is a frequency dependent phenomenon. The function $s(\mathbf{r}, \mathbf{r}_s; \omega)$ is therefore the frequency response of a filter, that produces a distortion of the amplitude and phase of a frequency component of the wave, as it propagates through the medium.

This filter is denoted the generalized frequency-dependent screen, and is composed of an amplitude screen and a phase screen defined as

$$s(\mathbf{r}, \mathbf{r}_s; \omega) = a(\mathbf{r}, \mathbf{r}_s; \omega)\ e^{i\theta(\mathbf{r}, \mathbf{r}_s; \omega)}\ . \tag{3.2}$$

The generalized frequency-dependent screen is dependent of the scatterers spatial position. Variation of the amplitude and phase with frequency of this filter, is a result of the aberration generated interference. Note that variation of the phase screen with frequency generates shape deformation (stretching) of the wave.

If a point impulse source is placed in the focus $\mathbf{r}_f$ of the array, it is shown in Ref. 17 (Ch. 11), that filtering the transmitted signal on each array element with the complex conjugate of the generalized frequency-dependent screen, is equal to time reversal,[13] and will reproduce the diffraction limited impulse field in $\mathbf{r}_f$.

This filter, defined as

$$h(\mathbf{r}_a; \omega) = s^*(\mathbf{r}_a, \mathbf{r}_f; \omega)\ , \tag{3.3}$$

where $\mathbf{r}_a$ is the array coordinate, represents an ideal diffraction limited aberration correction filter for the focal point of the array.

If the aberration is scatterer independent, the generalized frequency-dependent screen is independent of the scatterer position, and

$$s(\mathbf{r}_a, \mathbf{r}_s; \omega) = s(\mathbf{r}_a, \mathbf{r}_f; \omega) \equiv s(\mathbf{r}_a, \omega) \ , \tag{3.4}$$

where $s(\mathbf{r}_a, \omega)$ is denoted the generalized scatterer independent screen, or simply, the scatterer independent screen. For this case, the ideal aberration correction filter is

$$h(\mathbf{r}_a; \omega) = s^*(\mathbf{r}_a, \omega) \ . \tag{3.5}$$

The scatterer independent approximation is valid inside the isoplanatic patch, and ideal aberration correction with $s^*(\mathbf{r}_a, \omega)$ will be obtained inside the patch. In Ref. 12 it was shown that correction with the complex conjugate of the generalized frequency-dependent screen, produced almost ideal aberration correction (no aberration) to a level of -25 dB from the maximum value of beam profiles in the focal plane of the array, for both a weak and strong aberration situation.

In the work presented here, aberration correction was performed with a matched time-delay, and a time-delay and amplitude correction filter on transmit. This is an approximation of $s^*(\mathbf{r}_a, \mathbf{r}_f; \omega)$, and the aberration correction filter is now given as

$$\begin{aligned} h(\mathbf{r}_a; \omega) &= e^{i\omega\tau(\mathbf{r}_a)} \\ h(\mathbf{r}_a; \omega) &= a(\mathbf{r}_a) \ e^{i\omega\tau(\mathbf{r}_a)} \ , \end{aligned} \tag{3.6}$$

where both time-delays and amplitudes are assumed to be independent of frequency.

The discussion in this section shows that a time-delay, or a time-delay and amplitude aberration correction filter, represents a two-level approximation to aberration from an extended aberrator such as the human body wall. First, aberration is assumed to be scatterer independent $[s(\mathbf{r}_a, \mathbf{r}_f; \omega) = s(\mathbf{r}_a, \omega)]$. Second, aberration parameters (arrival time and amplitude fluctuations) are assumed to be independent of frequency.

II.B Aberration estimation

The developed estimation procedure is based on estimating the generalized frequency-dependent screen, $s(\mathbf{r}_a, \mathbf{r}_f, \omega)$, from back-scattered random signals using cross-correlation. Frequency independent arrival time and amplitude fluctuations are then determined from $s(\mathbf{r}_a, \mathbf{r}_f, \omega)$. The method assumes scatterer independent aberration, and Eq. (3.4) is thus valid.

In order to improve the cross-correlation estimate, averaging is performed. In general, two methods of averaging can be used. First, range averaging, that is, dividing the received signal in range segments and averaging cross-correlations for each segment. Second, using multiple transmit beams to generate backscatter from different scatterer volumes.

Assume the scatterers to constitute a statistical ensemble. Each outcome of the ensemble represents a spatial distribution of the scatterers $\nu(\mathbf{r}_s)$, where $\mathbf{r}_s$ denotes the scatterers spatial position. If the scatterer distributions are independent, averaging over the ensemble results in a δ-correlation of the scatterer distribution given as

$$\mathrm{E}[\nu(\mathbf{r}_{s1})\nu(\mathbf{r}_{s2})] = \sigma_\nu^2(\mathbf{r}_{s1}) \ \delta(\mathbf{r}_{s2} - \mathbf{r}_{s1}) \ , \tag{3.7}$$

where σ_ν^2 is the variance parameter of the distribution. This is valid if the correlation length of the scatterer distribution is much smaller than the wave length, and is normally denoted an incoherent medium. In a practical situation it is difficult to obtain δ-correlated scatterers due to tissue structures, which in most cases are larger than the wave length. A solution may be envisaged by imaging moving scatterers, like the heart or blood. Using consecutive transmit

beams with the same focus and amplitude, separated in time to ensure all scatterers in the observation volume to be replaced for each beam, the received signals will represent independent realizations of the ensemble.

Otherwise, neighboring transmit beams and multiple focusing may be used for stationary objects.[18,19] In this situation, some correlation between beams may exist, and the improvement in the correlation estimate is directly linked to the degree of correlation between the different receive signals used in the averaging process.

Development of the estimation procedure

The received signal y, can in the scatterer independent aberration situation be written in the frequency domain as [Ref. 17 (p. 11.55)]

$$y(\mathbf{r}_a;\omega) = s(\mathbf{r}_a,\mathbf{r}_f;\omega)\ f(\mathbf{r}_a;\omega) = s(\mathbf{r}_a;\omega)\ f(\mathbf{r}_a;\omega)\ , \tag{3.8}$$

where $f(\mathbf{r}_a;\omega)$ represents the unaberrated signal on receive. The function $f(\mathbf{r}_a;\omega)$ thus contains aberration on transmit, but not on receive.

The received signal can be written in a discrete form as

$$y_p = s_p f_p \quad , p = 1,\ldots,N\ , \tag{3.9}$$

where subscript p indicates the element number, and N the total number of elements on the array. Frequency dependence has now been dropped for notational convenience.

The cross-spectrum between element p and n on the receiving array is defined as

$$R_{pn} = \mathrm{E}[y_p\ y_n^*]\ , \tag{3.10}$$

where $\mathrm{E}[\cdot]$ denotes an expectation operator. Inserting from Eq. (3.9) gives

$$\begin{aligned} R_{pn} &= \mathrm{E}[s_p f_p (s_n f_n)^*] \\ &= s_p\ s_n^*\ F_{pn}\ , \end{aligned} \tag{3.11}$$

where $F_{pn} = \mathrm{E}[f_p\ f_n^*]$.

In the rest of the development, the magnitude of F_{pn} is assumed to be a known variable. The basis for this is discussed in the next section.

Solving for s_p gives

$$s_p = a_p\ e^{i\theta_p} = \frac{R_{pn}}{F_{pn}}\frac{e^{i\theta_n}}{a_n}\ , \tag{3.12}$$

where both s_p and s_n has been written with an amplitude and a phase. In the general case, F_{pn} can have a phase due to a refraction of the transmit beam introduced by the body wall [Ref. 17(p. 11.57-11.59)]. This phase is unknown and is incorporated into the phase of s_p as

$$s_p = \frac{R_{pn}}{|F_{pn}|}\frac{e^{i(\theta_n-\Delta_{pn})}}{a_n} \equiv \frac{R_{pn}}{|F_{pn}|}\frac{e^{i\theta_n}}{a_n} = \frac{R_{pn}}{|F_{pn}|}\frac{1}{s_n^*}\ , \tag{3.13}$$

where Δ_{pn} is the phase of F_{pn}, and $\theta_n - \Delta_{pn}$ has been renamed θ_n. This has been done since Δ_{pn} cannot be determined, and will not affect the calculation of s_p.

An estimate for R_{pn} was calculated as

$$\tilde{R}_{pn} = \frac{1}{K}\sum_{k=1}^{K} y_{kp}\ y_{kn}^*\ , \tag{3.14}$$

where K denotes the number of measurements from different realizations of the scattering region.

In Ref. 20 (p. 703) it is shown that the variance of the amplitude and phase of $\tilde{R}_{pn}$ is given as

$$\begin{aligned} \mathrm{Var}[\ |\tilde{R}_{pn}|\ ] &\sim \frac{1}{2K}|R_{pn}|^2\left(\frac{1}{|w_{pn}|^2}+1\right) \\ \mathrm{Var}[\ \angle\ \tilde{R}_{pn}\ ] &\sim \frac{1}{2K}\left(\frac{1}{|w_{pn}|^2}-1\right)\ , \end{aligned} \tag{3.15}$$

where the coherence w_{pn} is defined as

$$w_{pn} = \frac{R_{pn}}{\sqrt{R_{pp}\ R_{nn}}}\ . \tag{3.16}$$

Equation (3.15) shows that the variance of $\tilde{R}_{pn}$ is high when $|w_{pn}|^2$ is low. This motivates a weighted mean estimate of s_p as

$$\tilde{s}_p = \sum_{n=1}^{N} W_{pn}\ \frac{\tilde{R}_{pn}}{|F_{pn}|}\frac{1}{\tilde{s}_n^*}\ ,\ p=1,\ldots,N\ . \tag{3.17}$$

Here, W_{pn} is a weight function defined as

$$W_{pn} = |\tilde{w}_{pn}|^2 \Bigg/ \sum_{n=1}^{N}|\tilde{w}_{pn}|^2\ \ , \tag{3.18}$$

where $\tilde{w}_{pn}$ is an estimate of w_{pn} based on $\tilde{R}_{pn}$.

Equation (3.17) is an implicit equation, and was solved by iteration. An iterative scheme was set up as follows

$$\tilde{s}_{p,q+1} = \tilde{s}_{p,q} + \mu\left\{\tilde{s}_{p,q} - \left[\sum_{n=1}^{N} W_{pn}\frac{\tilde{R}_{pn}}{|F_{pn}|}\frac{1}{\tilde{s}_{n,q}^*}\right]\right\}\ , \tag{3.19}$$

where q is the iteration parameter, and μ is a constant convergence parameter. Zero phase and unity amplitude across the array was chosen as initial values for $\tilde{s}_p$ in the iteration scheme.

After convergence of Eq. (3.19), phase and amplitude estimates were defined as

$$\tilde{\theta}_p = \angle\ \tilde{s}_p,\ \tilde{a}_p = |\tilde{s}_p|\ . \tag{3.20}$$

Up to this point, the estimation procedure is still dependent on frequency, and Eq. (3.19) can be solved independently for all frequencies in the signal. As described in Section II.A, aberration correction was in this article performed with a frequency independent time-delay, and time-delay and amplitude filter [Eq. (3.6)]. This was done by estimating the cross-spectrum from Eq. (3.14), at the center angular frequency ω_0 of the transmitted signal. In addition, $\tilde{R}_{pn}$ was assumed to be a smooth function around ω_0, and additional averaging around ω_0 was performed to reduce the variance in the estimate.

To obtain a pure time-delay estimate, the phase estimate in Eq. (3.20) was assumed to be linear with the center angular frequency ω_0 of the transmitted pulse. The phase estimate $\tilde{\theta}_p$ is an absolute phase, and to obtain a relative phase estimate, the reference value for all $\tilde{\theta}_p$ was taken to be the arithmetic mean of the estimated values. The arrival time fluctuations estimate was then calculated as

$$\tau_p = \frac{1}{\omega_0}\left[\tilde{\theta}_p - \frac{1}{N}\sum_{n=1}^{N}\tilde{\theta}_n\right]\ . \tag{3.21}$$

Analysis of estimator

In the development of the estimator in Eq. (3.17), $|F_{pn}|$ was assumed to be a known variable. In Ref. 17 (p. 11.55) it is shown that for an incoherent medium (δ-correlated scatterers), F_{pn} can be calculated as

$$F_{pn} = \sum_l s_l \; s^*_{l+n-p} o_l \; o^*_{l+n-p} \; , \; l = 1, \ldots, N \; . \tag{3.22}$$

The function o denotes the excitation momentum amplitude of the array. Equation (3.22) is equivalent to the van Cittert-Zernike theorem which states that for propagation in a homogeneous medium, the receive spatial covariance from incoherent scatterers is the auto-covariance of the transmitted array function.[21] In this case, the array function is the product of the scatterer independent screen and the excitation momentum amplitude. Note that F_{pn} is frequency dependent due to the frequency dependence of the scatterer independent screen.

The magnitude of the scatterer independent screen can be normalized to a function that varies between 0 and 1. This means that

$$|R_{pn}| \leq |F_{pn}| \; , \tag{3.23}$$

with equality if, and only if $|s| = 1$. Because of the previous result, the ratio $\tilde{R}_{pn}/|F_{pn}|$ in Eq. (3.17) will be dominated by $\tilde{R}_{pn}$, and little sensitive to variations in $|F_{pn}|$. As a result of this, Eq. (3.19) was solved with the value of $|F_{pn}|$ obtained from Eq. (3.22) with $|s| = 1$ and $|o| = 1$, which results in a correlation of a rectangular function with itself.

The estimate of the cross-spectrum [Eq. (3.14)] can be showed to be unbiased.

$$\mathrm{E}[\tilde{R}_{pn}] = \mathrm{E}\left[\frac{1}{K}\sum_{k=1}^{K} y_{kp} y^*_{kn}\right] = \frac{1}{K}\sum_{k=1}^{K} R_{pn} = R_{pn} \; . \tag{3.24}$$

Inserting $\tilde{a}_n = a_n$ and $\tilde{\theta}_n = \theta_n$ into Eq. (3.17) and calculating the expectation gives

$$\mathrm{E}[\tilde{s}_p] = \sum_{n=1}^{N} W_{pn} \frac{\mathrm{E}[\tilde{R}_{pn}]}{|F_{pn}|} \frac{e^{i\theta_n}}{a_n} = \sum_{n=1}^{N} W_{pn} \frac{R_{pn}}{|F_{pn}|} \frac{1}{s^*_n} = s_p \sum_{n=1}^{N} W_{pn} \; . \tag{3.25}$$

In this case the estimate is unbiased if $\sum_n W_{pn} = 1$, which by the definition of the weights W_{pn} in Eq. (3.18) is fulfilled.

If $\tilde{a}_n \neq a_n$ and $\tilde{\theta}_n \neq \theta_n$, it is difficult to calculate the expectation of $\tilde{s}_p$, since it requires solution of a set of implicit equations. In Ref. 12 it was shown that estimates of arrival time and amplitude fluctuations in the signal from a point source, provided close to optimal correction of the transmitted focused beam when used in an aberration correction filter. This leads to the recognition that estimates of arrival time and amplitude fluctuations from point sources are qualified estimates of the screen s_p, and can be used as reference values for quantifying the quality of the developed estimation procedure. This was done here.

Inserting Eq. (3.14) into Eq. (3.17) leads to

$$\tilde{s}_p = \sum_{n=1}^{N} W_{pn} \frac{1}{K} \sum_{k=1}^{K} y_{kp} y^*_{kn} \frac{1}{|F_{pn}|} \frac{1}{\tilde{s}^*_n} = \frac{1}{K} \sum_{k=1}^{K} y_{kp} \; \hat{b}^*_{kp} \; , \tag{3.26}$$

where

$$\hat{b}_{kp} = \sum_{n=1}^{N} y_{kn} \frac{W_{pn}}{|F_{np}|} \frac{1}{\tilde{s}_n} \; . \tag{3.27}$$

The estimate $\tilde{s}_p$ can hence be viewed as a correlation of the received signal on element p with a modified beamformer output of the signal received over the whole array. The beamformer output b of a received signal is defined as

$$b = \sum_{n=1}^{N} y_n \ . \tag{3.28}$$

The modification consists of a weight term and an aberration correction term.

III Method

III.A Modeling of aberration

To generate realistic aberration, two body wall models were created. These are the same two body wall models which were used in Ref. 12, where a weak aberrating body wall model was denoted w6, and a strong aberrating body wall model was denoted s6. In this article these two body wall models are denoted the weak, and strong aberrator respectively. In Ref. 12 a thorough description of the generation of the body wall models, and their justification, is given.

III.B Simulations

After creating suitable body wall models for generating aberration, 2D simulations were performed. A homogeneous angular spectrum operator, described in Ref. 12, was used to propagate the signals. All simulations were performed for 20 different realizations of the scattering region, and for both the weak and strong aberrators. The simulation setup in Fig. 3.1 was used in three different situations as described below.

Point source simulations

In order to estimate the general frequency-dependent screen [Eq. (3.1)], and to estimate reference values for the arrival time and amplitude fluctuations, point source simulations were performed according to the setup in Fig. 3.1. No scattering region was now present in the setup.

A point source was simulated in the focus $\mathbf{r}_f$ of an array of size D. The array was situated directly onto the distributed body wall models of thickness d. A pulse was generated at the point source and propagated homogeneously with the angular spectrum operator to the body wall models, and then through the wall models as described in Ref. 12, to the receive array.

A point source simulation provides the ideal situation for estimation of the generalized frequency-dependent screen. It was determined by filtering the received signal y from the point source with a Wiener-like filter h_W in the frequency domain given by the equation

$$s(\mathbf{r}_a, \mathbf{r}_f; \omega) = h_W(\mathbf{r}_a, \mathbf{r}_f; \omega)\ y(\mathbf{r}_a, \mathbf{r}_f; \omega), \tag{3.29}$$

where $\mathbf{r}_a$ represents the array coordinate and $\mathbf{r}_f$ the focus of the array (see Fig. 3.1). The transfer function for the filter was

$$h_W(\mathbf{r}_a, \mathbf{r}_f; \omega) = \frac{y_t^*(\mathbf{r}_a, \mathbf{r}_f; \omega)}{|y_t(\mathbf{r}_a, \mathbf{r}_f; \omega)|^2 + \frac{max(\ |y_t(\mathbf{r}_a, \mathbf{r}_f; \omega)|^2\ )}{SN}}, \tag{3.30}$$

where y_t is the transmitted frequency dependent signal from the point source. The factor SN represents a signal-to-noise ratio parameter in the filter which was determined empirically.

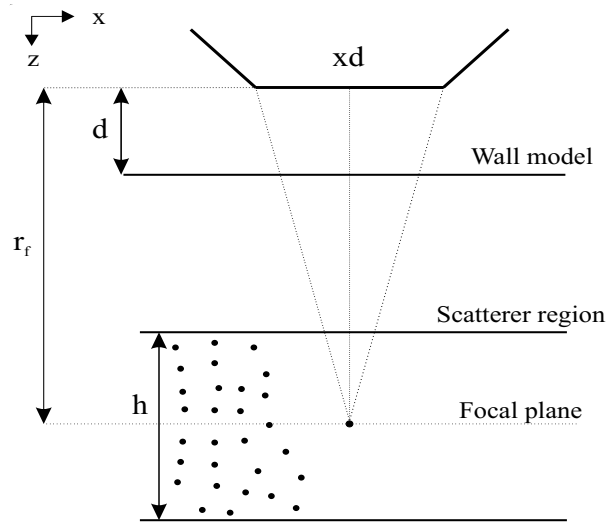

Figure 3.1: Simulation setup.

Scatterer independent aberration simulations

In the general case, the generalized frequency-dependent screen is dependent on the source position in space (in this case the focus point of the array $\mathbf{r}_f$). As explained in the introduction, scatterer independent aberration was created by concentrating all distortion of the heterogeneous medium into a plane on the transmitting/receiving array. This is equal to assuming scatterer independent aberration as in Eq. (3.4).

Scatterer independent signals could then be generated without using the extended aberrator in Fig. 3.1. These were round-trip simulations.

On transmit, the focused signal from the array was filtered with $s(\mathbf{r}_a, \mathbf{r}_f; \omega)$ as estimated in Eq. (3.29), to create scatterer independent aberration. The aberrated signal was propagated homogeneously to the scattering region, where it was scattered according to the Born approximation, *i.e.* only first order scattering was considered. The scattered signal was propagated back to the array, where it again was filtered with $s(\mathbf{r}_a, \mathbf{r}_f; \omega)$ to generate receive aberration.

Scatterer dependent aberration simulations

Scatterer dependent aberration was created by using the distributed body wall models, as for the point source simulations. These were also round-trip simulations and the same setup was used for scatterer dependent aberration with a corrected transmitted beam.

The transmitted signal was propagated through the body wall models, and then homogeneously to the scattering region. Here it was scattered according to the Born approximation, and propagated back to the array through the body wall models.

IV Simulation parameters and data processing

The simulations were implemented in MATLAB, and the FFTW algorithm for calculation of the angular spectrum was used. The simulation area was 10.24 cm in the lateral direction (x-direction in Fig. 3.1) with a resolution of 0.2 mm. To avoid wrap-around effects from the FFT, the signal was tapered to zero over 2.54 cm region at each edge of the simulation area in the x-direction. The tapering was performed for a sufficient number of propagation steps in order to keep the noise level from the wrap-around effects sufficiently low. The sampling frequency was 35.1 MHz providing a time window of 58.3 μs. Center frequency of the pulse was 2.5 MHz with a -6 dB bandwidth of 1.6 MHz. The pulse was filtered on transmit with a 3.7 MHz band-pass filter centered around the center frequency of the pulse. An array aperture size of 20 mm with point-like elements was chosen. The focal depth of the array was set to 60 mm. Water at 37°C was used as the propagation medium. All receive signals were corrected for geometric focusing for the homogenous medium before processing of results.

To generate a realistic speckle signal, an area of 30.5 mm (time window of 20 μs), 15.25 mm to each side of the focal plane (see Fig. 3.1), was used as a scattering region. The scatterer density was approximately 1600 scatterers per square centimeter. The scatterers were uniformly distributed in the x and z-direction, and had a Gaussian distributed reflection strength. Twenty different independent realizations of the scatterer region were produced.

The cross-spectrum (Sec. II.B) was calculated by taking the Fourier transform of the received signal on each array element over the entire range of the scattering region. The cross-spectrum between all elements on the receiving array was then calculated according to Eq. (3.14), and this process was performed and averaged for the twenty generated statistically independent signals. The cross-spectrum was assumed to be a smooth function around the parameter frequency (in this case the center frequency of the signal) and was averaged over a small band of frequencies with equal weight. This band ranged from approximately 2.4 MHz to 2.6 MHz, which constituted eleven frequencies with the resolution used in the simulations.

Estimation of arrival time fluctuations from point source simulations was performed with a phase front tracking algorithm. In essence, the phase front tracking algorithm determined the peak of the first period of the received waveform from the point source. The tracking was then performed on each element, and the time-delay between two elements was defined as the difference in time between the two peaks of the respective elements. For all arrival time fluctuations estimates presented in this article, a linear fit was subtracted in order to remove any refraction of the beam.

Arrival amplitude fluctuations across the array from point source simulations, were determined by taking the Fourier transform in time of the received signal on each element. The amplitude on each element of the array was calculated as the arithmetic mean of the amplitudes, of the now frequency dependent signal, over a band of frequencies ranging from 2-3 MHz. This band was chosen empirically.

Beam profiles in the focal plane of the array were used for visual evaluation of the effect of different aberration correction filters. All aberration corrected signals were propagated through the distributed body wall models as in Fig. 3.1. The profiles were calculated as the rms value in time of each spatial position.

Additional evaluation of the correction filters in the focal plane were performed by calculation of focus quality parameters. These were effective widths in the array and range direction, and calculation of a peripheral energy ratio. Details of the definition of these parameters are given in.[1]

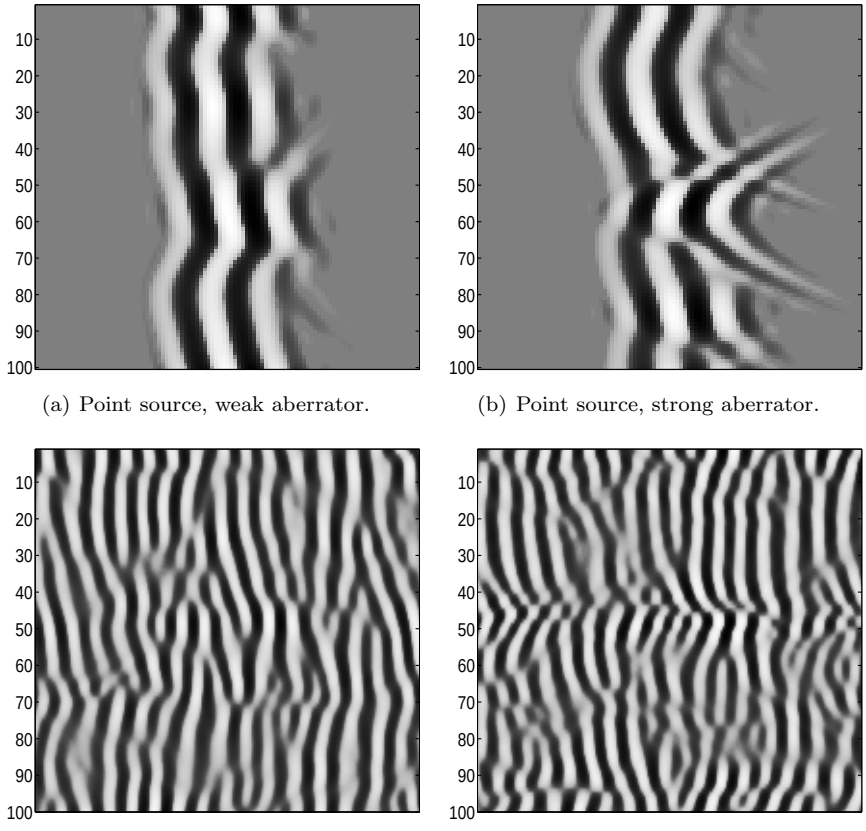

(a) Point source, weak aberrator.

(b) Point source, strong aberrator.

(c) Random scatterers, weak aberrator.

(d) Random scatterers, strong aberrator.

Figure 3.2: Received waveforms from point sources in the focus of the array and from one realization of the random scatterers for the SDA situation. Each pane shows a temporal logarithmic gray scale picture of the waveforms at the receiving array. The dynamic range of the logarithmic scale is 40 dB. The horizontal axis represents time, and for the point source simulations it spans 2.9 μs. For the random scatterer results the time axis spans 5.7 μs. The vertical axis represents the receive array elements and spans 20 mm. The left panes shows the waveform received after propagation through the weak aberrator and the right panes shows the waveform from the strong aberrator.

V Results

Figure 3.2 shows received waveforms from the point source simulations, and from one realization of the random scatterers for the SDA situation. For the point source simulations, shape distortion of the waveforms is clearly visible, and in the strong aberration case deformation of the waveform also occurs in several places. Since the waveforms are pictured with a logarithmic scale and a dynamic range of 40 dB, amplitude fluctuations do not show. For the signal from random scatterers strong decorrelation of the signals is visible.

In the expression for the variance [Eq. (3.15)] of the amplitude of the cross-spectrum, the absolute value of the cross-spectrum squared, and the inverse of the coherence squared enters. The variance of the phase of the cross-spectrum is given by the inverse of the coherence squared. Figure 3.3 displays contour plots of the absolute value of the cross-spectrum and coherence,

between all elements on the receiving array for the weak aberrator. The diagonal from bottom left to top right of the cross-spectrum matrices displays areas of high and low correlation in the signal due to variations in receive amplitudes. In Fig. 3.3 (a) (SIA), such variations are clearly visible. For the SDA situation (c), cross-spectrum values are in general higher compared to the scatterer independent case indicating a higher variance and a poorer amplitude estimate. There is also a stretching of the high amplitude areas in the matrix, resulting in a reduced pinpointing of amplitude peaks. In the CSDA case the same variations in the cross-spectrum as in the SIA case are visible, but the width of the diagonal amplitude band is wider, indicating higher variance.

The coherence is the cross-spectrum normalized according to Eq. (3.16). In the SIA case, the coherence displays a diagonal band indicating high correlation along the whole of the receiving array. The width of the band (rows in the matrix) indicates how other elements of the array correlates with a specific element. For the SIA case, the width of the band is approximately constant which means that the same amount of information is used in estimation of the phase and amplitude for each element. In the SDA situation, the width of the band is generally narrower and varies along the diagonal resulting in an increased variance of the phase estimate. Results for the CSDA situation show increased coherence along the diagonal resulting in reduced variance for the phase estimate in comparison to the SDA situation.

Figure 3.4 shows contour plots of the absolute value of the cross-spectrum and coherence for the strong aberrator. These results depict the same situation as for the weak aberrator. Note that the width of the coherence band for the SIA situation [Fig. 3.4 (b)] is reduced in comparison to the weak aberrator, which shows that the correlation is reduced for the strong aberrator.

Arrival time and amplitude fluctuation estimates for the weak aberrator are presented in Fig. 3.5. The figure shows that estimates of arrival time fluctuations for the SIA [Fig. 3.5 (a)], and CSDA situation [Fig. 3.5 (e)], are approximately identical and very close to point source estimates. In the SDA case, estimates deviate from point source estimates, which is a direct result of the lowered correlation in the estimated cross-spectrum as shown in Fig. 3.3.

Figure 3.6 shows arrival time and amplitude fluctuation estimates for the strong aberrator. These results show the same trend as for the weak aberrator. In the SDA case, estimated arrival time fluctuations strongly deviates from point source estimates due to lowered correlation in the received signal. Note that for the SIA and the CSDA, discontinuities occur in the estimates. These discontinuities are due to the wave deformation clearly visible in Fig. 3.2 (b). The wave deformation is also visible in Fig. 3.4, where the coherence is close to zero in the region of pulse deformation. This effect cause the variance of phase estimates to be very high, resulting in poor arrival time fluctuation estimates.

Arrival amplitude fluctuation estimates for both the weak and strong aberrators, show the same trend as estimates for arrival time fluctuations. Amplitude estimate in the SIA situation is approximately identical to point source estimates for both body wall models. Estimates for the SDA are very poor for both body walls respectively. This is an effect of the reduced variation in the cross-spectrum as shown in Figs. 3.3 (c) and 3.4 (c). In the CSDA situation, estimates are not as good as point source estimates, but compared to the SDA situation they have improved substantially.

Beam profiles corrected with a time-delay, and a time-delay and amplitude filter for the weak aberrator, are presented in Fig. 3.7. The beam profiles, together with the focus quality parameters given in Table 3.1, show the efficiency of the aberration correction filter. Note that the focus quality measures in Table 3.1 cannot be directly compared to the presented beam profiles, as they are calculated in a different way. But they do portray the same effects visible in the beam profiles. It should also be stressed that focus quality measures of the aberrated beam profiles are uncertain since there is no clearly defined mainlobe. For the SIA, and CSDA situation, time-delay corrected profiles are almost identical and very close to the point source

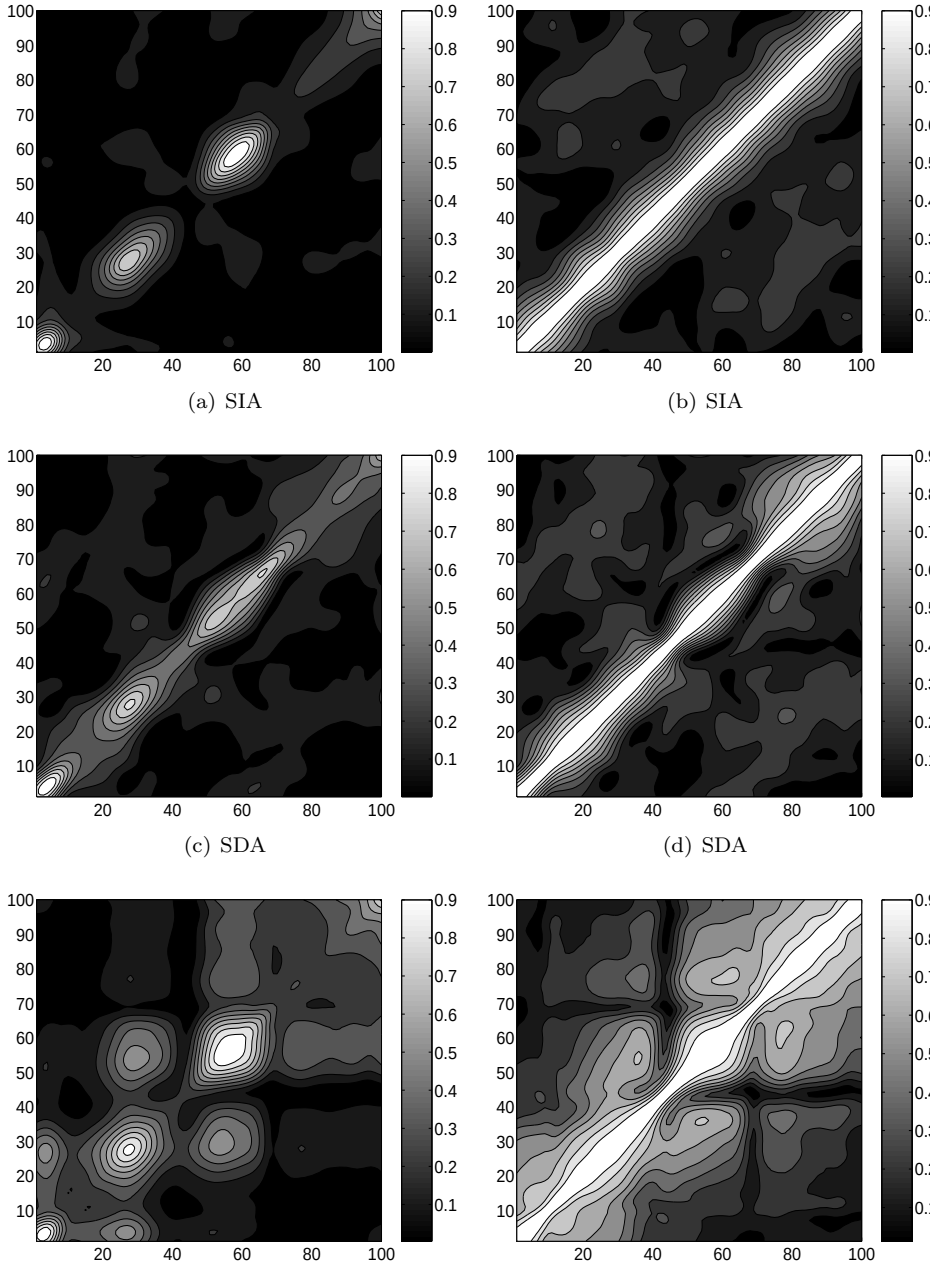

(a) SIA (b) SIA

(c) SDA (d) SDA

(e) CSDA (f) CSDA

Figure 3.3: Contour plots of the absolute value of the cross-spectrum and coherence between all elements on the receiving array, for the weak aberrator. The values are stacked in a matrix form. The left column shows absolute values of the cross-spectrum and the right column absolute values of the coherence. The cross-spectrum is normalized to the largest value in the matrix. Both the horizontal and vertical axes represent array elements. The labels explains the aberration situation. SIA - scatterer independent aberration, SDA - scatterer dependent aberration, CSDA - corrected scatterer dependent aberration.

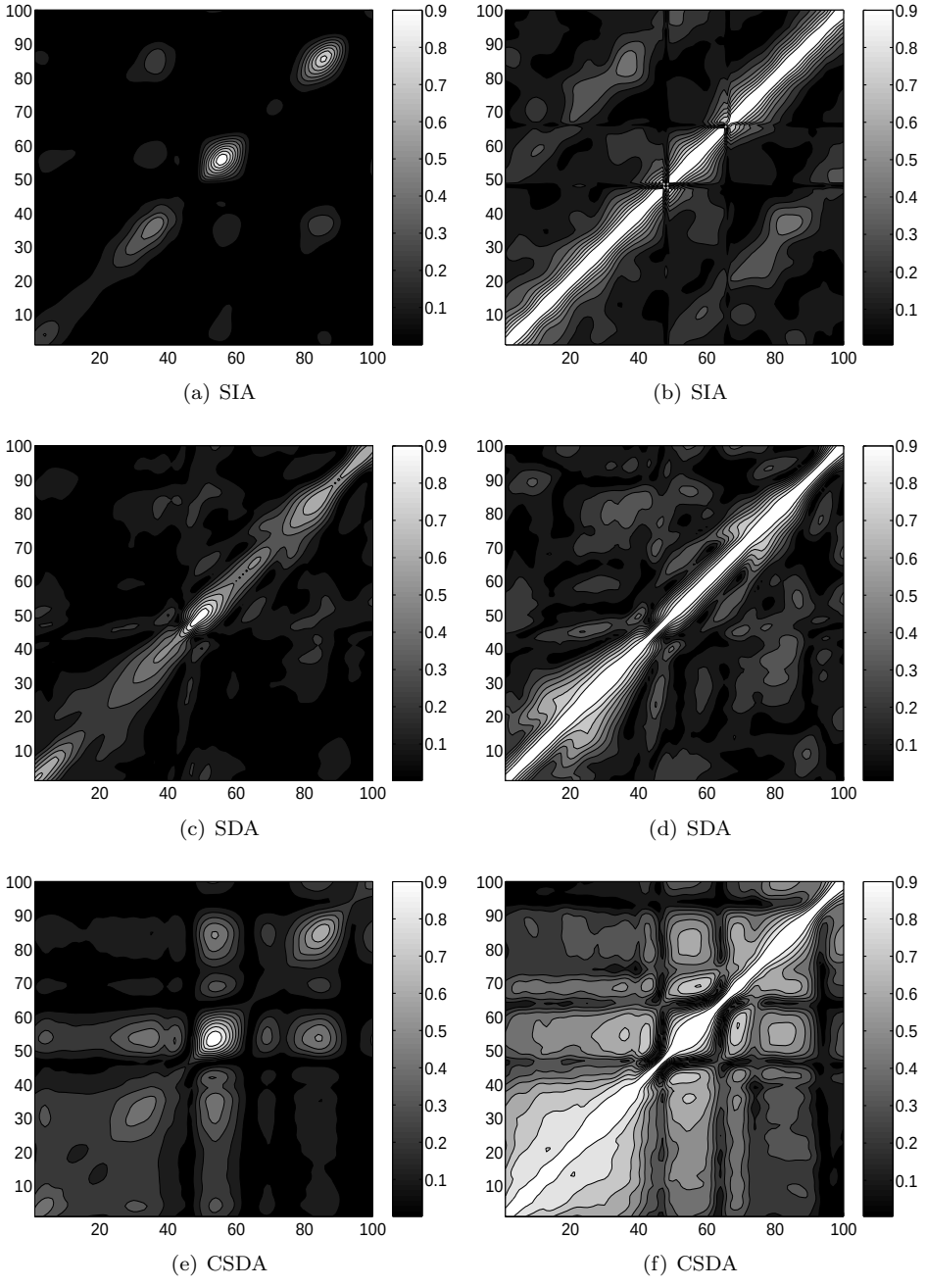

Figure 3.4: Contour plots of the absolute value of the cross-spectrum and coherence between all elements on the receiving array for the strong aberrator. The values are stacked in a matrix form. The left column shows absolute values of the cross-spectrum and the right column absolute values of the coherence. The cross-spectrum is normalized to the largest value in the matrix. Both the horizontal and vertical axes represent array elements. Same labeling as in Fig. 3.3.

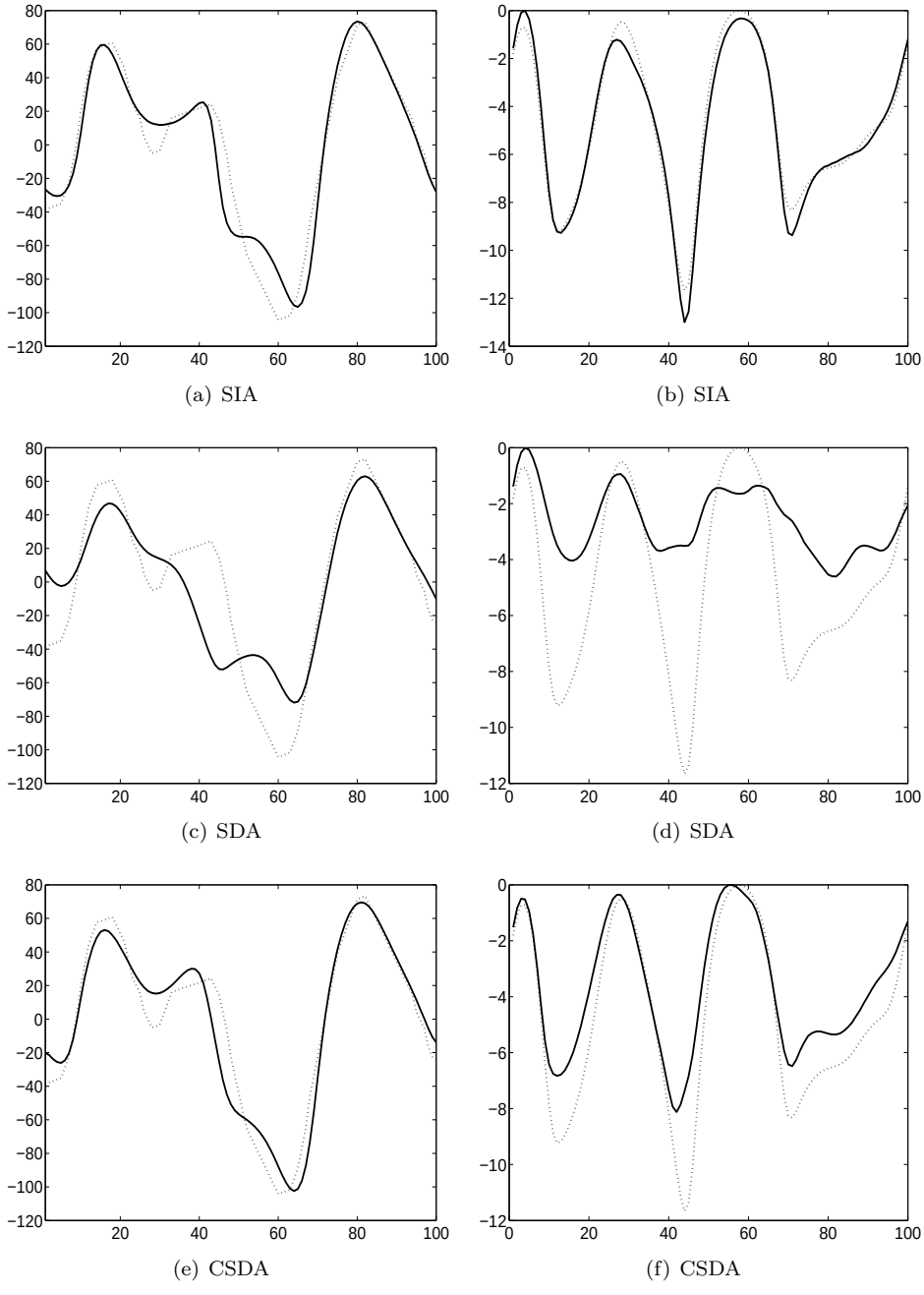

Figure 3.5: Arrival time and amplitude fluctuation estimates for the weak aberrator. The left column shows arrival time fluctuations and the right column amplitude fluctuations. The horizontal axis in both rows represents array elements. The vertical axis for arrival time fluctuations is displayed in (ns), and the vertical axis for amplitude fluctuations is in (dB). The dotted line represents estimates from point source simulations and serves as a reference. The solid line shows estimates from the random scatterer region. Same labeling as in Fig. 3.3.

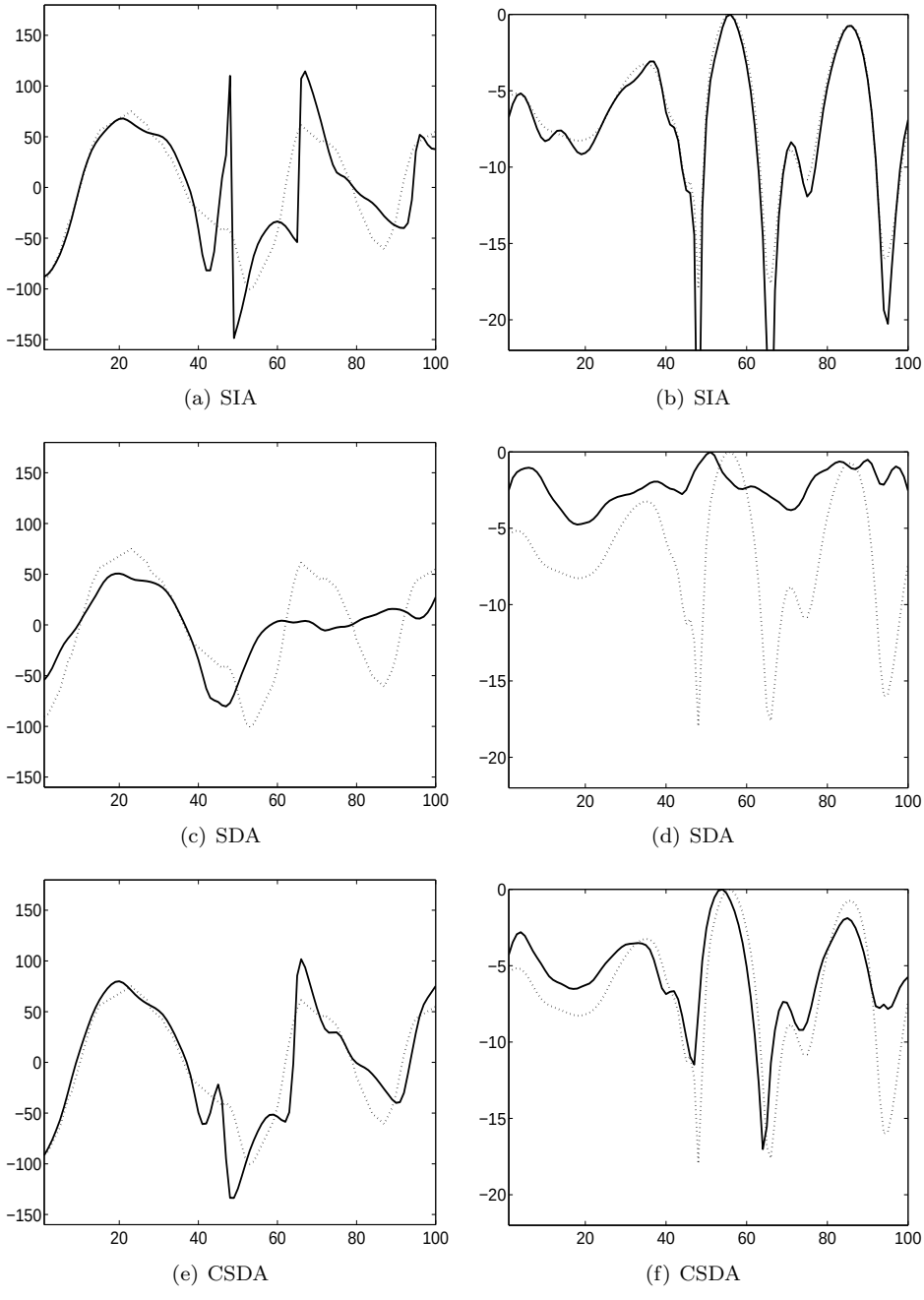

(a) SIA (b) SIA

(c) SDA (d) SDA

(e) CSDA (f) CSDA

Figure 3.6: Arrival time and amplitude fluctuation estimates for the strong aberrator. The left column shows arrival time fluctuations and the right column amplitude fluctuations. The horizontal axis in both rows represents array elements. Same notation and labeling as in Fig. 3.5.

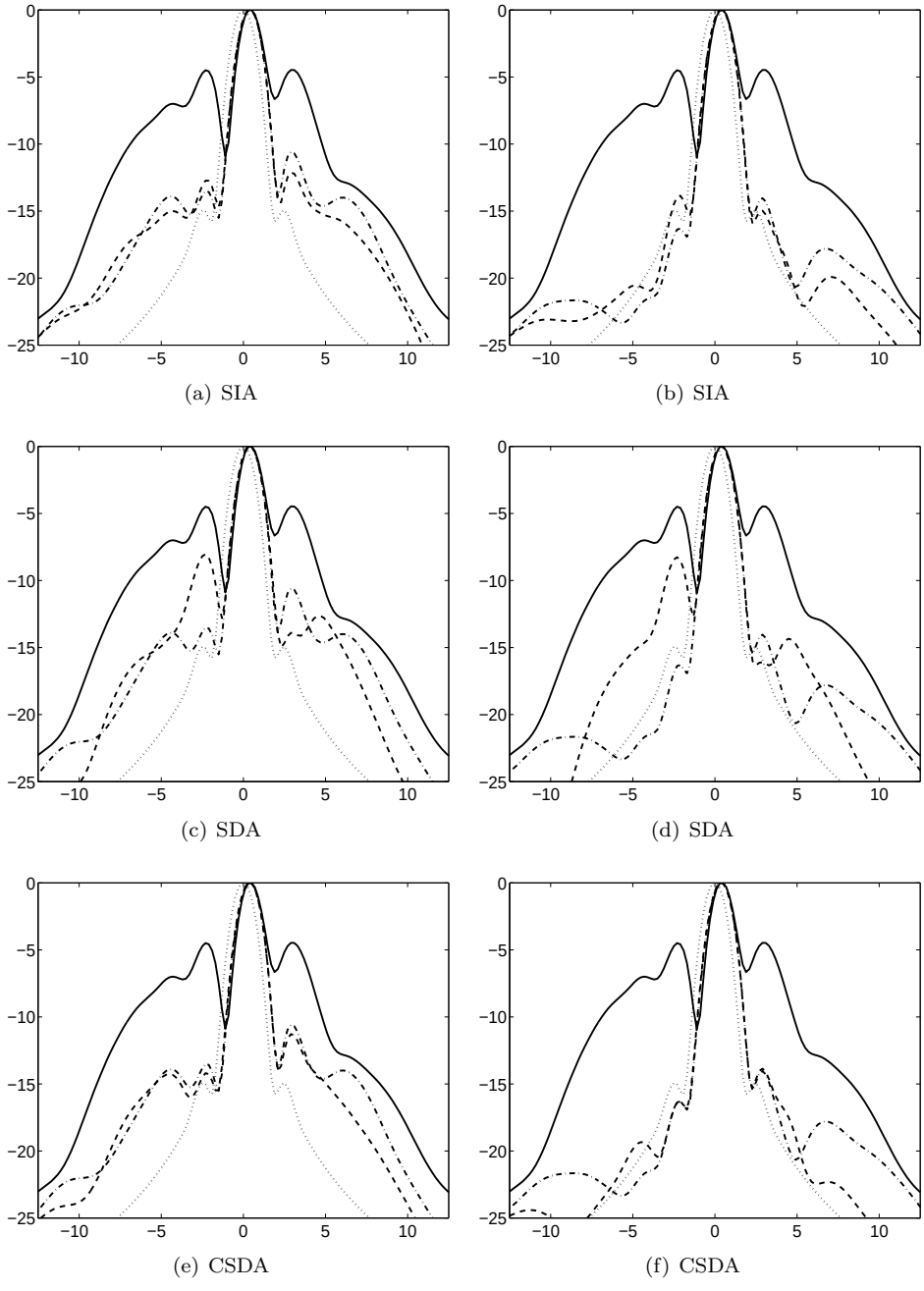

Figure 3.7: Beam profiles in the focal plane for the weak aberrator. The left column shows beam profiles corrected with a time-delay correction filter. The right column shows beam profiles corrected with a time-delay and amplitude correction filter. The horizontal axis represents the focal plane (mm) and the vertical axis energy (dB). The zero point on the horizontal axis denotes the center axis of the transmitting array. The solid line represents the aberrated profile, the dashed-dotted line the profile corrected with estimates from a point source, the dashed line shows the profile corrected with estimates from the random scattering region, and the dotted line the profile with no aberration, which serves as a reference. All profiles are normalized to their maximum value. Same labeling as in Fig. 3.3.

corrected profile. Note that there is a slight refraction of the beam to the right of the center axis of the array. The effective widths from Table 3.1 are identical to the ideal case for these two cases, but the -10 dB peripheral energy ratio is higher due to generally higher sidelobe level. In the SDA situation, estimates of arrival time fluctuations deviated from point source estimates resulting in a less focused beam profile with a relatively high side lobe level. The beam profile for the SDA situation has a turning point at approximately -10 dB, and makes the -10 dB peripheral energy ratio measure unreliable. The effective width at -10 dB is, on the other hand, very large in the array direction portraying poor correction.

Beam profiles corrected with a time-delay and amplitude filter show a further reduction in sidelobe level for the SIA and CSDA situations. Note also that correction of the beam profile has improved further away from the central axis of the array. This again leads to reduced peripheral energy ratios, and for both cases they are now close to the ideal situation. For the SDA situation, amplitude estimates were very poor and do not change the corrected beam profile significantly. There is some reduction in the effective width in the array direction, and the peripheral energy ratio.

Corrected beam profiles for the strong aberrator are shown in Fig. 3.8. Also in this case, correction with a time-delay filter for the SIA and CSDA situation, improves the beam profiles. Note that refraction of the beam is stronger for this aberrator than for the weak. Introducing amplitude correction in addition to time-delay correction, improves beam profiles substantially for both these cases. This is also shown in the focus quality variables where the -10 dB peripheral energy ratio is reduced. For the SDA situation, correction with a time-delay filter is very poor. Introducing amplitude correction does not change the beam profile, and there is almost no difference in the peripheral energy ratio.

VI Discussion

The aberration in the scatterer independent aberration simulations, were performed by filtering the signal on transmit and receive with an estimate of the generalized frequency-dependent screen [Eq. (3.29)]. This means that the resulting aberrated beam profiles for the SIA and SDA situation are not identical. The results of the estimated arrival time and amplitude fluctuations for these cases (Fig. 3.5 and Fig. 3.6), show that the differences are negligible.

As explained in Section IV, the cross-spectrum was assumed to be a smooth function around the center angular frequency, and averaged over eleven neighboring frequencies. Averaging over a number of M frequencies is analogous to averaging in range, that is subdividing the signal in M range segments for each channel and estimating the cross-spectrum of each segment. This results in a smoothing of the frequency spectrum. The band of frequencies for averaging was chosen empirically.

The scatterers were modeled as uniformly distributed in space with a Gaussian distributed reflection strength. This constitutes an ideal set of scatterers with no interference from strong scatterers, or strong scattering regions within the scattering region itself. Absorption and electronic/acoustic noise (*e.g.* reverberations) were not included in the simulations. In a practical situation, all of these effects would exist and probably deteriorate the estimate of the cross-spectrum. One of the purposes of this article was, on the other hand, to demonstrate the basic differences between scatterer independent aberration (which forms the general assumption for aberration correction) and scatterer dependent aberration. Thus having a receive signal as ideal as possible was in the interest of the analysis.

The range of the scatterer region was chosen to be well inside the 3 dB depth of focus of the

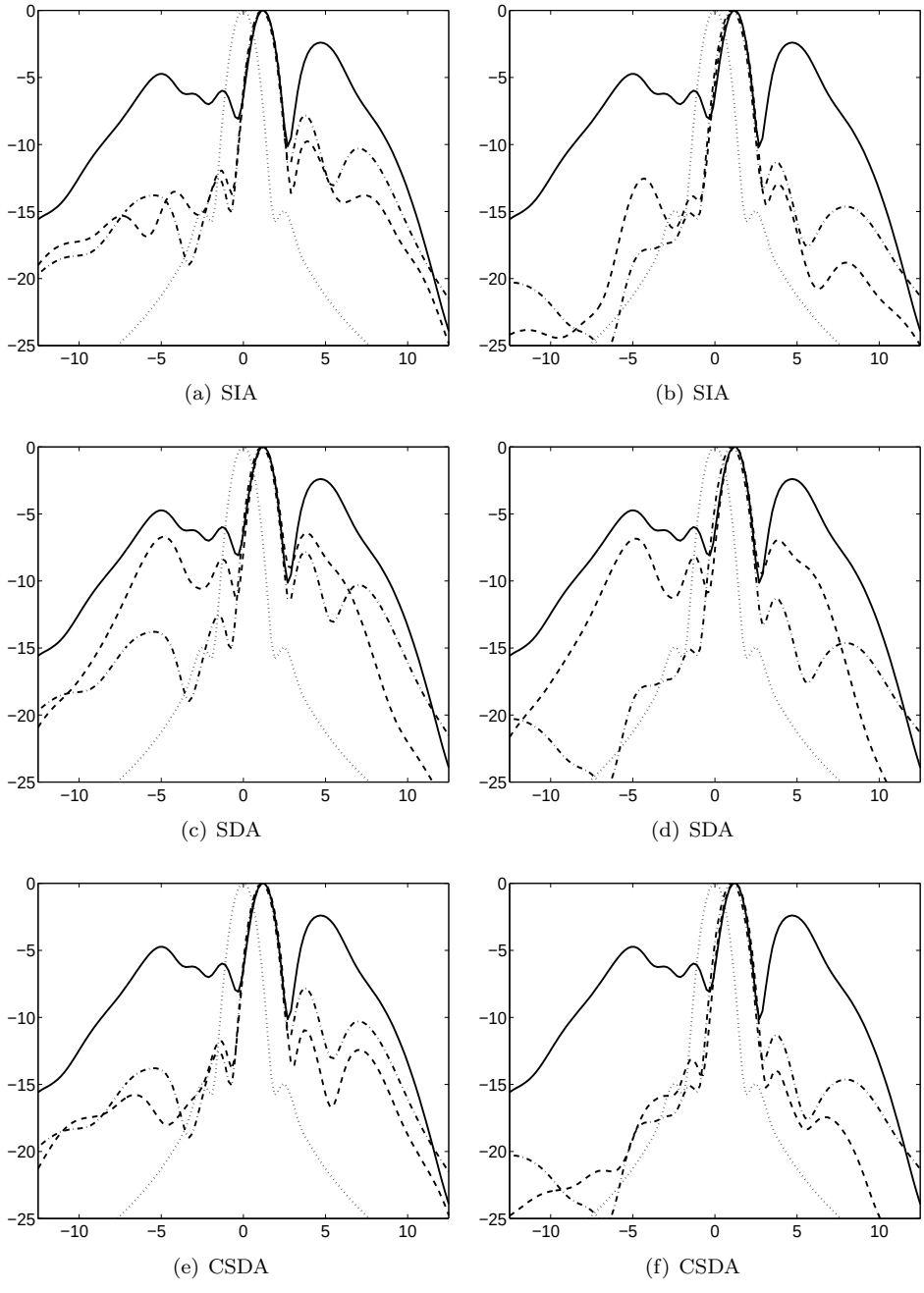

(a) SIA (b) SIA

(c) SDA (d) SDA

(e) CSDA (f) CSDA

Figure 3.8: Beam profiles in the focal plane for the strong aberrator. The left column shows beam profiles corrected with a time-delay correction filter. The right column shows beam profiles corrected with a time-delay and amplitude correction filter. Same notation and labeling as in Fig. 3.7.

Table 3.1: Table of focus quality parameters. The peripheral energy ratio (PER) and all effective widths have been calculated at -10 dB level from the peak. The parameters d_e, w_a, and w_t denotes the effective diameter, the effective width in the array direction, and the effective width in the time direction respectively. The two column headings refers to the weak and strong aberration aberrators. The first column indicates the aberration situation and the notation follows the notation in Fig. 3.3. The notation **PS** in this column denotes correction with estimates from the point source. The second column specifies the type of correction where $\boldsymbol{\tau}$ denotes the time-delay correction filter, and $\boldsymbol{\tau}$**&a** the time-delay and amplitude correction filter. The two last rows has no value in the second column. The first of these rows shows the ideal situation with no aberration, and the second the aberrated situation.

		Weak aberrator						Strong aberrator			
		PER	d_e (mm)	w_a (mm)	w_t (mm)			PER	d_e (mm)	w_a (mm)	w_t (mm)
SIA	τ	0.427	1.84	2.70	1.26	SIA	τ	0.645	1.88	2.80	1.26
SDA	τ	0.420	2.68	5.70	1.26	SDA	τ	1.060	2.34	3.70	1.47
CSDA	τ	0.418	1.84	2.70	1.26	CSDA	τ	0.554	1.88	2.80	1.26
PS	τ	0.477	1.84	2.70	1.26	PS	τ	0.763	1.88	2.80	1.26
SIA	τ&a	0.287	1.84	2.70	1.26	SIA	τ&a	0.363	1.94	3.00	1.26
SDA	τ&a	0.362	2.63	5.50	1.26	SDA	τ&a	1.080	2.03	2.80	1.47
CSDA	τ&a	0.253	1.88	2.80	1.26	CSDA	τ&a	0.315	1.91	2.90	1.30
PS	τ&a	0.300	1.84	2.70	1.26	PS	τ&a	0.439	1.91	2.90	1.26
IDEAL		0.228	1.84	2.70	1.26	IDEAL		0.228	1.84	2.70	1.26
AB		1.230	2.58	4.50	1.47	AB		1.440	3.68	6.50	2.08

array. The 3 dB depth of focus can be calculated as [Ref. 22 (p. 1.14)]

$$L_f(3\text{ dB}) \approx 7.2\lambda(\text{FN})^2 \ , \tag{3.31}$$

where λ is the wavelength of the transmitted pulse and FN the *f*-number defined as $\text{FN} = \mathbf{r}_f/D$ (see Fig. 3.1). In the simulations performed in this article, the wavelength was $\lambda = 0.6$ mm and the *f*-number FN = 3, which gives $L_f(3\text{ dB}) \approx 39$ mm. A scattering region of 15.25 mm in range to each side of the focal point, is thus well inside the 3 dB focal depth of the transmitting array.

The wavefront tracking algorithm used to estimate arrival time fluctuations from the point source simulations is dependent on a clearly defined wavefront, which is the case for a wave emanating from a single point source. The speckle signal created in this article represents the sum of signals from many point sources, and has not a clearly defined wavefront. This would also be the case for tissue images in ultrasound imaging systems, and this method for arrival time estimation is only suited for ideal situations. Since the method tracks the front of the wave, it is little sensitive to waveform deformation, and for the point source simulations performed, this method proved to give very accurate estimates of arrival time fluctuations in the received wavefront.

Results in this article show that for scatterer independent aberration, arrival time and amplitude fluctuations are estimated in accordance with results obtained from point source simulations. When introducing a body wall model of thickness two centimeters, the quality of estimates of arrival time and amplitude fluctuations are significantly reduced compared to point source estimates. This is mainly due to the increased aberration interference in the signal, caused by the distributed aberrator, which results in a reduced spatial coherence (see Figs. 3.3

and 3.4).

There is some improvement in the beam profiles for the scatterer dependent aberration, especially for the weak aberrator. This leads to the notion of an iterated estimation/correction procedure. In an iteration procedure, arrival time and amplitude fluctuations could be estimated as in this article, and a corrected signal would be transmitted for the purpose of performing a new estimation of the same parameters. The process would be repeated until some convergence criterion is achieved. This is also known as adaptive imaging. The optimum convergence would be obtained when the estimates are equal to those obtained from a point source. The corrected scatterer dependent aberration situation presented in this article, displays the ideal last stage of such an iteration process. The results show that if the transmitted signal is corrected with an ideal time-delay and amplitude filter, aberration in the received signal is indeed scatterer independent, and arrival time fluctuations are very well estimated. Amplitude variations are not as well estimated as from the point source simulations, but this does not affect the corrected beam profiles noticeably, and the peripheral energy ratios in this case are even better than for the point source estimates (see Table 3.1).

VII Conclusions

A method for estimating arrival time and amplitude fluctuations from random signals has been developed. The method can also be used to estimate phase and amplitude aberration for all frequency components in the received signal. It was tested on different situations of aberration, scatterer independent aberration and scatterer dependent aberration. Results obtained with signals from random scatterers were compared with estimates from point source simulations.

For the SIA and CSDA situation, arrival time and amplitude fluctuations estimates were very close to point source estimates for both the weak and strong aberrator. Used in a time-delay, and time-delay and amplitude aberration correction filter, they produced equivalent correction of transmitted beam profiles as correction with point source estimates. For both the SIA and CSDA situation, a time-delay and amplitude filter corrected significantly better than a time-delay filter alone.

In the SDA situation, arrival time fluctuations differed significantly from point source estimates. With the strong aberrator, estimates were poor, yielding a limited correction of the beam profile. The method was only able to estimate arrival amplitude variations of about 4 dB for both aberrators, while for the strong aberrator, variations of up to 18 dB was estimated from the point source. The difference between a time-delay, or a time-delay and amplitude correction filter was negligible for the strong aberrator. This was mainly due to the poor estimates of both arrival time and amplitude fluctuations. For the weak aberrator, correction of the beam profile was observed (there is some correction also in the strong case) and the time-delay and amplitude filter corrects better than the time-delay filter.

The results presented here demonstrate the difficulty of estimating and correcting ultrasound aberration with a time-delay, or a time-delay and amplitude aberration correction filter. This is due to the fact that aberration is generated over an extended part of the human body wall. Aberration correction with a time-delay, or a time-delay and amplitude aberration correction filter assumes all aberration to be concentrated on the transmitting/receiving array. On the other hand, the results show that if the receive aberration is scatterer independent, the developed estimation method for arrival time and amplitude fluctuations from random signals works well.

For the distributed body wall models (scatterer dependent aberration), the estimation method does not produce satisfactory results, even with 20 independent realizations of the received signals. Some correction is still obtained, and estimates could possibly be improved by iteration.

This work also demonstrates that, if correctly estimated, a time-delay or a time-delay and amplitude correction filter produce receive signals with aberration that is independent of the scatterers spatial position. This indicates that such a correction filter can focus the aberrated transmitted beam to the inside of the isoplanatic patch, the necessary condition for obtaining receive scatterer independent aberrated signals from randomly distributed scatterers.

Acknowledgments

The work presented in this article was supported by the Medicine and Health program of the Research Council of Norway. Tonni F. Johansen and Ingmund Bjørkan developed large parts of the Born approximation scattering part of the simulation code. The authors would like to thank Professor Harald Krogstad at the Department of Mathematical Sciences, NTNU, for valuable insight into the world of stochastic processes. The reviewers are thanked for constructive comments that improved this article.

References

[1] D.-L. Liu and R. C. Waag, "Time-shift compensation of ultrasonic pulse focus degradation using least-mean-square error estimates of arrival time," *J. Acoust. Soc. Am.*, vol. 95, no. 1, pp. 542–555, January 1994.

[2] L. M. Hinkelman and D.-L. Liu, L. A. Metlay, and R. C. Waag, "Measurements of ultrasonic pulse arrival time and energy level variations produced by propagation through abdominal wall," *J. Acoust. Soc. Am.*, vol. 95, no. 1, pp. 530–541, January 1994.

[3] L. M. Hinkelman and D.-L. Liu, R. C. Waag, and Q. Zhu and B. D. Steinberg, "Measurement and correction of ultrasonic pulse distortion produced by the human breast," *J. Acoust. Soc. Am.*, vol. 97, no. 3, pp. 1958–1969, March 1995.

[4] L. M. Hinkelman, T. L. Szabo, and R. C. Waag, "Measurements of ultrasonic pulse distortion produced by human chest wall," *J. Acoust. Soc. Am.*, vol. 101, no. 4, pp. 2365–2373, April 1997.

[5] L. Hinkelman, T. D. Mast, L. A. Metlay, and R. C. Waag, "The effect of abdominal wall morphology on ultrasonic pulse distortion. part i. measurements," *J. Acoust. Soc. Am.*, vol. 104, no. 6, pp. 3635–3649, December 1998.

[6] Q. Zhu and B. Steinberg, "Deaberration of incoherent wavefront distortion: An approach toward inverse filtering," *IEEE Trans. Ultrason. Ferroelectr. Freq. Control*, vol. 44, no. 3, pp. 575–589, May 1997.

[7] S. W. Flax and M. O'Donnell, "Phase-aberration correction using signals from point reflectors and diffuse scatterers: Basic principles," *IEEE Trans. Ultrason. Ferroelectr. Freq. Control*, vol. 35, no. 6, pp. 758–767, November 1988.

[8] M. O'Donnell and S. W. Flax, "Phase-aberration correction using signals from point reflectors and diffuse scatterers: Measurements," *IEEE Trans. Ultrason. Ferroelectr. Freq. Control*, vol. 35, no. 6, pp. 768–774, November 1988.

[9] L. A. Ødegaard, "Using signals scattered from diffuse inhomogeneities to correct for phase aberrations caused by a phase-screen far from the transducer," *IEEE Ultrasonics Symp. Proc.*, vol. 2, pp. 1443–1447, 1995.

[10] S. Krishnan, P.-C. Li, and M. O'Donnell, "Adaptive compensation of phase and magnitude aberrations," *IEEE Trans. Ultrason. Ferroelectr. Freq. Control*, vol. 43, no. 1, pp. 44–55, January 1996.

[11] W. F. Walker and G. E. Trahey, "Aberrator integration error in adaptive imaging," *IEEE Trans. Ultrason. Ferroelectr. Freq. Control*, vol. 44, no. 4, pp. 780–791, July 1997.

[12] S.-E. Måsøy, T. F. Johansen, and B. Angelsen, "Correction of ultrasonic wave aberration with a time delay and amplitude filter," *J. Acoust. Soc. Am.*, vol. 113, no. 4, pp. 2009–2020, April 2003.

[13] M. Fink, C. Prada, F. Wu, and D. Cassereau, "Self focusing in inhomogeneous media with "Time Reversal" acoustic mirrors," *Ultrasonics Symposium, 1989 Proceedings, IEEE 1989*, pp. 681–686, 1989.

[14] D.-L. Liu and R. C. Waag, "Correction of ultrasonic wavefront distortion using backpropagation and a reference waveform method for time-shift compensation," *J. Acoust. Soc. Am.*, vol. 96, no. 2, pp. 649–660, August 1994.

[15] J. C. Lacefield and R. C. Waag, "Evaluation of backpropagation methods for transmit focus compensation," *Ultrasonics Symposium, 2001 IEEE*, vol. 2, pp. 1495–1498, 2001.

[16] T. D. Mast, L. M. Hinkelman, M. J. Orr, and R. C. Waag, "The effect of abdominal wall morphology on ultrasonic pulse distortion. part ii. simulations," *J. Acoust. Soc. Am.*, vol. 104, no. 6, pp. 3651–3664, December 1998.

[17] B. Angelsen, *Ultrasound imaging. Waves, signals and signal processing.* Trondheim: Emantec, 2000, vol. II, http://www.ultrasoundbook.com.

[18] M. Karaman, A. Atalar, H. Köymen, and M. O'Donnell, "A phase aberration correction method for ultrasound imaging," *IEEE Trans. Ultrason. Ferroelectr. Freq. Control*, vol. 40, no. 4, pp. 275–282, July 1993.

[19] T. Varslot, B. Angelsen, and R. C. Waag, "Spectral estimation for characterization of acoustic aberration," *J. Acoust. Soc. Am.*, vol. 116, no. 1, pp. 97–108, July 2004.

[20] M. B. Priestley, *Spectral Analysis and Time Series.* Academic Press, 1988.

[21] R. Mallart and M. Fink, "The van Cittert-Zernike theorem in pulse echo measurements," *J. Acoust. Soc. Am.*, vol. 90, no. 5, pp. 2718–2727, November 1991.

[22] B. Angelsen, *Ultrasound imaging. Waves, signals and signal processing.* Trondheim: Emantec, 2000, vol. I, http://www.ultrasoundbook.com.

Chapter 4

Iteration of transmit-beam aberration correction in medical ultrasound imaging

S. Måsøy[1] and T. Varslot[2], B. Angelsen[1]
1)Department of Circulation and Imaging, NTNU
2)Department of Mathematical Sciences, NTNU.

Simulations of iterative transmit-beam aberration correction using a time-delay and amplitude filter have been performed to study the convergence of such a process. Aberration in medical ultrasonic imaging is usually modeled by arrival-time and amplitude fluctuations concentrated on the transducer array. This is an approximation of the physical aberration process, and may be applied to correct the transmitted signal using a time-delay and amplitude filter. Estimation of such a filter has proven difficult in the presence of severe aberration. Presented here is an iterative approach, whereby a filter estimate is applied to correct the transmit-beam. This beam induces acoustic backscatter better suited for arrival-time and amplitude estimation, thus facilitating an improved filter estimate. Two correlation-based methods for estimating arrival-time and amplitude fluctuations in received echoes from random scatterers were employed. Aberration was introduced using eight models emulating aberration produced by the human abdominal wall. Results show that only a few iterations are needed to obtain corrected transmit-beam profiles comparable to those of an ideal aberration correction filter. Furthermore, a previously developed focusing criterion is found to quantify the convergence accurately.

I Introduction

Aberration in medical ultrasound imaging is observed as reduced resolution in the images. It is mainly produced by spatial variation of acoustic parameters (mass density and bulk compressibility) in the human body wall. The loss of resolution may, in many situations, render a reliable diagnosis based on these images difficult to obtain. Extensive research has therefore been carried out in order to solve this problem.

Iteration of transmit-beam aberration correction is defined as a process where a set of aberration parameters is estimated; the estimated parameters are used for correcting the transmitted ultrasound beam; and a new estimate of the same parameters is calculated. This

process is then repeated. The parameters are typically arrival-time or arrival-time and amplitude fluctuations. Iteration of transmit-beam aberration correction is sometimes referred to as adaptive imaging or auto-focusing, but these terms are also used to denote aberration correction in general.

In the presented work, iteration of transmit-beam aberration correction is studied. This process is abbreviated *transmit-beam iteration* in the remainder of the article.

Flax and O'Donnell[1,2] studied transmit-beam iteration using estimated arrival-time differences between neighbor elements on the receiving array. They considered aberration from a thin phase-screen just in front of the array. Using such aberration, a transmit-beam iteration process for correcting the phase of the transmit signal using time-delays estimated from neighbor correlation, was argued to be a process that inherently converges to an ideal transmit-focus.

In Refs. 3 and 4 the morphology of the abdominal wall was studied. It was found that a single time-delay or phase-screen is not adequate for modeling aberration of the ultrasound wave. This is due to the fact that aberration consists of both phase and amplitude aberration, and that these effects occur throughout the whole thickness of the body wall.[4] In this situation, the arguments of Flax and O'Donnell[2] are not sufficient. In Ref. 5 it was shown that an appropriate time-delay and amplitude filter can produce close-to-ideal correction. It has yet to be shown that iterative transmit-beam aberration correction based on estimating a time-delay and amplitude filter from random scatterers will yield a similar correction.

In Refs. 6–8 transmit-beam iteration was performed using different methods for aberration correction, but no consistent measure of convergence was introduced. In Ref. 6 several iterations were performed in order to estimate phase aberrations only. The efficiency of the correction was evaluated using the root-mean-square (rms) difference between the estimated phase and a reference phase, where the reference was obtained from a beacon signal (point source). In many practical situations such a beacon signal is not available. This metric is therefore not useful for evaluating convergence of transmit-beam iteration in most imaging situations.

Rigby *et al.*[9] performed *in vivo* transmit-beam iteration using time-delays with a 1.75D array. They used a beamsum-channel correlation method for estimating arrival-time fluctuations and found the algorithm to converge after three or four iterations. The results obtained showed improved image quality, but it is not certain to what the algorithm converged as no reference values could be obtained from the subjects investigated.

Other authors have also described transmit-beam iteration,[10–14] but only performed aberration correction on either the received signal, or on the transmitted and the received signal. No further iterations were carried out.

In order to obtain qualitative data concerning the convergence of a transmit-beam iteration process, two aberration estimation methods are compared in this article. Both methods estimate arrival-time and amplitude fluctuations using signals from random scatterers. The estimated arrival-time and amplitude fluctuations are then used as a matched filter for time-delay and amplitude aberration correction.

The first estimation method correlates each element signal with a reference signal. The reference signal is a weighted and modified beamformer output of the received signal.[15] The second method uses an eigenfunction decomposition of the cross-spectrum to maximize the expected energy in the received signal.[16]

In order to evaluate the quality of an aberration correction method, Mallart and Fink developed a focusing criterion based on the van Cittert-Zernike theorem.[11] An analogous criterion was developed by Liu and Waag.[10] Lacefield and Waag[14] discuss the utility of this focusing criterion since the van Cittert-Zernike theorem is only valid for propagation in a homogeneous medium. The width of the average receive coherence function at different levels was suggested as an alternative measure to evaluate an aberration correction method. A monotonic relation

between the coherence widths and the effective widths of point spread functions was observed in single-transmit images.

Both of these measures are used in this article, in order to evaluate the convergence of the transmit-beam iteration process. The process is also evaluated by comparing arrival-time and amplitude fluctuation estimates to those obtained from point source simulations. A simulation with a point source in the focus of the array provides an optimal situation for observing aberration of the ultrasound wave, and serves as a good reference.

Absorption effects, electronic noise and acoustic reverberation noise were not included in the simulations.

II Theory

II.A Signal and aberration correction modeling

Following Angelsen [Ref. 17 (Ch. 11)], the aberration is modeled by relating the Green's function for the wave equation with constant coefficients to the Green's function for the wave equation with spatially variable coefficients using a filter denoted the *generalized frequency-dependent screen*. The frequency response of this filter describes the aberration introduced to each frequency component of the signal.

If the generalized frequency-dependent screen is independent of the position in space at which the backscatter was created, the signal received at array coordinate $\mathbf{r}_a$ can be written as[15]

$$y(\mathbf{r}_a;\omega) = s(\mathbf{r}_a;\omega)\ f(\mathbf{r}_a;\omega)\ . \tag{4.1}$$

The function $f(\mathbf{r}_a;\omega)$ is an integral over a volume containing scatterers distributed in space, and represents the unaberrated acoustic backscatter signal. It does, however, depend on the transmitted beam, and is thus a function of the transmit aberration.

The situation where aberration on an array element satisfies the assumption of being independent of the spatial position of the scatterer, is denoted *scatterer-independent aberration.*[15] This can be viewed as concentrating all aberration of the inhomogeneous medium to a layer at the array surface. For an extended aberrator of varying thickness, this assumption is generally not satisfied, but may be a good approximation inside a region surrounding the focal point; *the isoplanatic patch.* A received signal according to Eq. (4.1) is thus obtained by focusing the transmitted beam to the inside of the isoplanatic patch.

The two aberration estimation methods employed in this article perform aberration correction using a time-delay and amplitude correction filter with transfer function

$$h(\mathbf{r}_a;\omega) = a(\mathbf{r}_a)\ e^{i\omega\tau(\mathbf{r}_a)}. \tag{4.2}$$

The time-delay τ, and amplitude a, are functions of the array coordinate $\mathbf{r}_a$, but do not depend on frequency. This approximation of the correction filter is valid for band-limited signals assuming scatterer-independent aberration.

It has been shown that a time-delay and amplitude filter produces close-to-ideal correction (no aberration), if correct estimates for the arrival-time and amplitude fluctuations are obtained, even in the case of severe aberration.[5]

II.B Scatterer-independent aberration and the van Cittert-Zernike theorem

When the scatterers are randomly distributed in space, the backscatter signal is a stochastic variable. Assuming scatterer-independent aberration, the cross-spectrum between the received

signal at location $\mathbf{r}_p$ and $\mathbf{r}_n$ on an array may be expressed using Eq. (4.1)

$$R(\mathbf{r}_p, \mathbf{r}_n) = s(\mathbf{r}_p)s^*(\mathbf{r}_n)\ F(\mathbf{r}_p, \mathbf{r}_n). \tag{4.3}$$

Here $F(\mathbf{r}_p, \mathbf{r}_n)$ is the cross-spectrum of the backscatter signal without aberration. Dependence on frequency has been omitted for notational convenience.

In Ref. 18 the van Cittert-Zernike theorem was developed for incoherent acoustic backscatter and propagation through a homogeneous medium. If the aberration is scatterer-independent, the van Cittert-Zernike theorem may be applied. In this case, $F(\mathbf{r}_p, \mathbf{r}_n) = F(\mathbf{r}_p - \mathbf{r}_n) \equiv F(\boldsymbol{\xi})$ is computed as [Ref.[17] (p. 11.55)]

$$F(\boldsymbol{\xi}) = \frac{\sigma_\nu^2}{4\pi^2} \int_{S_a} s(\mathbf{r} + \boldsymbol{\xi})s^*(\mathbf{r})o(\mathbf{r} + \boldsymbol{\xi})o^*(\mathbf{r})\mathrm{d}\mathbf{r}. \tag{4.4}$$

Here σ_ν^2 is the scattering intensity, the integration is performed over the array surface S_a, and $o(\mathbf{r})$ denotes the array apodization function.

Equation (4.4) shows that the coherence in the received signal is limited by the aberration as well as the apodization function. This has been experimentally observed,[14] although it was not compared to an explicit theoretical prediction.

III Estimators

In this article two previously developed estimators[15,16] are employed to study transmit-beam iteration. For the convenience of the reader and to introduce notation, the rationale behind both estimators is briefly reviewed. Then the two methods are compared, and new insight into the similarities and differences between them is provided.

Both estimators are based on the cross-spectrum of the received acoustic backscatter. For the purpose of this study, the received signal is assumed to be a Gaussian stochastic process with zero mean value. This implies that all statistical information is contained in the covariance function, or equivalently, the cross-spectrum. For a time-delay and amplitude correction filter as in Eq. (4.2), it is sufficient to consider the cross-spectrum at a single frequency.

For a given frequency ω, the cross-spectrum between the *element signals* $y_p(\omega)$ and $y_n(\omega)$, received at element p and n respectively, is defined as

$$R_{pn} = \mathrm{E}[y_p\ y_n^*]\ . \tag{4.5}$$

Frequency-dependence has been dropped for notational convenience.

For the comparison to be useful, both estimation methods use the same estimate of the cross-spectrum. In order to obtain a proper estimate of the cross-spectrum with low variance, an average over statistically independent backscatter signals is used. In a practical situation, statistically independent signals can be obtained by imaging scatterers which are replaced between each consecutive transmit-beam, *e.g.* blood or contrast agents. Alternatively, non-overlapping regions of the scatterer distribution may be utilized by combining beams in a linear/sector scan.[6,19]

The estimate of the cross-spectrum is a cross-periodogram given as

$$\tilde{R}_{pn} = \frac{1}{K}\sum_{k=1}^{K} y_{kp}y_{kn}^*\ , \tag{4.6}$$

where k denotes received backscatter signals from different random scatterer realizations, and K is the total number of such realizations. To further lower the variance of the estimate in

Eq. (4.6), additional averaging over a small band of frequencies is performed which results in a smoothed cross-periodogram.

Reference 20 (p. 703) shows that the variance of the cross-spectrum estimate in Eq. (4.6) may be found as

$$\begin{aligned} \mathrm{Var}[\ |\tilde{R}_{pn}|\ ] &\sim \frac{1}{2K}|R_{pn}|^2\left(\frac{1}{|w_{pn}|^2}+1\right) \\ \mathrm{Var}[\ \angle\ \tilde{R}_{pn}\ ] &\sim \frac{1}{2K}\left(\frac{1}{|w_{pn}|^2}-1\right)\ , \end{aligned} \tag{4.7}$$

where the coherence w_{pn} is defined as

$$w_{pn} = \frac{R_{pn}}{\sqrt{R_{pp}\ R_{nn}}}\ . \tag{4.8}$$

This implies that the variance of the cross-spectrum is high when the coherence is low and vice versa.

Modified beamformer output - MBFO

This section offers a brief description of the *modified beamformer output* (MBFO) estimator, which was presented in Ref. 15.

The basic premise for this method is that the received signal can be written as in Eq. (4.1), that is, scatterer-independent aberration is assumed. Applying the same discrete notation as in Eq. (4.5) to denote elements p and n in Eq. (4.3), and solving for s_p leads to

$$s_p = \frac{R_{pn}}{F_{pn}}\frac{1}{s_n^*}. \tag{4.9}$$

In order to use all possible correlation information to estimate the phase and amplitude of s_p, a weighted average $\hat{s}_p$ is defined

$$\hat{s}_p = \sum_{n=1}^{N} W_{pn}\ \frac{\tilde{R}_{pn}}{F_{pn}}\frac{1}{\hat{s}_n^*}\ , \tag{4.10}$$

where N is the total number of elements on the array. Here W_{pn} is a set of weights and $\tilde{R}_{pn}$ is the estimate for R_{pn}.

In this article the weights are chosen as

$$W_{pn} = |\tilde{w}_{pn}|^2 \Big/ \sum_{n=1}^{N} |\tilde{w}_{pn}|^2\ \ , \tag{4.11}$$

where $\tilde{w}_{pn}$ is an estimate of the coherence w_{pn} [Eq. (4.8)] based on $\tilde{R}_{pn}$. Thus the estimates of R_{pn} with low variance are emphasized. Furthermore, the phase of F_{pn} is not known, and F_{pn} is therefore replaced by its absolute value. The MBFO estimator $\tilde{s}_p$ is then

$$\tilde{s}_p = \sum_{n=1}^{N} W_{pn}\ \frac{\tilde{R}_{pn}}{|F_{pn}|}\frac{1}{\tilde{s}_n^*}\ . \tag{4.12}$$

An estimate for $|F_{pn}|$ can be found from the van Cittert-Zernike theorem as formulated in Eq. (4.4).[15]

The estimator in Eq. (4.12) is a set of N coupled nonlinear equations which has to be solved, that is, for $p \in \{1, \cdots, N\}$. An iterative solution method as described in Ref. 15 was utilized for this purpose. The initial estimate for s_p in the iterative solution method was chosen as zero phase and unity amplitude across the array.

Eigenfunction estimator - EFE

The *eigenfunction estimator* (EFE) was presented in Ref. 16. Thus, only a short description of the method is provided here.

Consider the stochastic vector of receive signals at a particular frequency ω and transducer elements indexed from 1 to N

$$\mathbf{y} = [y_1 \; y_2 \; \cdots \; y_N]^{\mathrm{T}}. \tag{4.13}$$

Given a vector $\mathbf{h} = [h_1 \; h_2 \; \cdots \; h_N]^{\mathrm{T}}$, a stochastic linear functional $\mathcal{L}_h$ may be defined on $\mathbf{y}$ as

$$\mathcal{L}_h \mathbf{y} = \mathbf{h}^{\mathrm{H}} \mathbf{y} = \sum_{p=1}^{N} y_p h_p^*, \tag{4.14}$$

where H denotes the Hermitian of the vector.

The quantity $\mathcal{L}_h \mathbf{y}$ from Eq. (4.14) is the temporal frequency result when a filter with transfer function $h_p(\omega)$ is applied to the signal received at transducer element p before the standard beamforming procedure is executed. It is a stochastic variable with associated variance expressed as

$$\begin{aligned} ||\mathcal{L}_h \mathbf{y}||^2 &\equiv \mathrm{E}\left[\mathcal{L}_h \mathbf{y} \left(\mathcal{L}_h \mathbf{y}\right)^{\mathrm{H}}\right] \\ &= \mathbf{h}^{\mathrm{H}} \mathrm{E}\left[\mathbf{y}\mathbf{y}^{\mathrm{H}}\right] \mathbf{h} \\ &= \mathbf{h}^{\mathrm{H}} R \mathbf{h}. \end{aligned} \tag{4.15}$$

Here R is the cross-spectrum matrix of the receive signal at the frequency ω.

The variance is the *expected energy* for $\mathcal{L}_h \mathbf{y}$ at this frequency. Since the matrix R is Hermitian the expected energy, subject to the constraint $\mathbf{h}^{\mathrm{H}} \mathbf{h} = 1$, is maximized when $\mathbf{h}$ is an eigenvector associated with the largest eigenvalue of R (see Ref. 21, Ch. 6.5).

Through finding the eigenvector which maximizes the expression in Eq. (4.15), a match filter which maximizes the *speckle brightness*,[22] is constructed. The normalization $\mathbf{h}^{\mathrm{H}} \mathbf{h} = 1$ for each frequency ensures that the correction filter does not alter the frequency distribution for the energy of the aberration-corrected transmit-beam.

The eigenvector $\tilde{\mathbf{h}}$ associated with the largest eigenvalue of $\tilde{R}$ is calculated and used as an estimate of the filter $\mathbf{h}$.

Comparison of the estimators

Both methods estimate aberration from the cross-spectrum of stochastic backscatter. The MBFO estimator also assumes the aberration on a receive element to be independent of the spatial position of the scatterers, *i.e.*, a signal model according to Eq. (4.3). The EFE estimator makes no such assumption.

The MBFO estimator has been shown to be equivalent to correlating the received signal with a correlation reference;[15] a *modified beamformer output*

$$\begin{aligned} \tilde{s}_p &= \frac{1}{K}\sum_{k=1}^{K} y_{kp} b_{kp}^* \\ b_{kp} &= \sum_n W_{pn} \frac{1}{|F_{pn}|\tilde{s}_n} y_{kn}. \end{aligned} \tag{4.16}$$

The modified beamformer output, b_{kp}, is formed by using a weight term W_{pn} and a correction term $1/|F_{pn}|s_n$ for each element signal y_{kn}.

The same interpretation is possible for the EFE

$$\tilde{h}_p = \frac{1}{K}\sum_{k=1}^{K} y_{kp}\beta_k^* \tag{4.17}$$

$$\beta_k = \sum_n \frac{1}{\lambda}\tilde{h}_n^* y_{kn}. \tag{4.18}$$

Equal weight, $1/\lambda$, is placed on all element signals when forming the modified beamformer output β_k. The correction term in this case is h_n^*.

A major difference between the two estimators is that the correction term for the MBFO estimate is obtained by applying the aberration correction filter as an inverse filter, while the correction for the EFE is obtained by matched filtering. In addition, the MBFO estimator utilizes a different set of weights for each transducer channel p, thus obtaining a different correlation reference signal for each channel. The EFE estimator makes use of the same correlation reference for all channels.

To compare the estimators further, it is instructive to consider the case where $F_{pn} = |F_{pn}|$. This will be the case when for example the scattering medium is incoherent and all phase aberration of the transmitted beam has been corrected.

Let S be the diagonal matrix

$$S = \begin{pmatrix} s_1 & & \\ & \ddots & \\ & & s_N \end{pmatrix}. \tag{4.19}$$

Equation (4.15) is then reformulated as

$$\begin{aligned} ||\mathcal{L}_h \mathbf{y}||^2 &= \mathbf{h}^{\mathrm{H}} R \mathbf{h} \\ &= \mathbf{h}^{\mathrm{H}} S F S^{\mathrm{H}} \mathbf{h}, \end{aligned} \tag{4.20}$$

where F is the cross-spectrum matrix for the unaberrated acoustic backscatter. Therefore, $S^{\mathrm{H}}\mathbf{h}$ must be an eigenvector of F. Now, since F is real, then the eigenvector $S^{\mathrm{H}}\mathbf{h}$ is real as well. In this case the phase of h_p is equal to that of s_p; the phase estimated by the EFE will be an unbiased estimate for the phase of the screen.

Furthermore, it is easy to see that if $\mathbf{h}$ is an eigenvector of R with eigenvalue λ, then

$$h_p = \frac{1}{\lambda}\sum_n R_{pn} h_n = \sum_n \frac{|F_{pn}||h_n|^2}{\lambda} \frac{R_{pn}}{|F_{pn}|} \frac{1}{h_n^*}. \tag{4.21}$$

The EFE therefore satisfies an equation of the same type as Eq. (4.12) for the MBFO, with weights $W_{pn} = |F_{pn}||h_n|^2/\lambda$.

If the weights W_{pn} in Eq. (4.12) are required to satisfy $\sum_n W_{pn} = 1$, then the MBFO will by construction be an unbiased estimate for the screen.[15] However, for the EFE this requirement is not necessarily fulfilled. The result is a biased estimate of the amplitude.

Express the amplitude bias in a multiplicative fashion

$$h_p = \alpha_p s_p, \tag{4.22}$$

where α_p is real and positive, and s_p, as previously, denotes the screen. Inserting this into Eq. (4.21) yields

$$s_p = \sum_n \frac{|F_{pn}||s_n|^2\alpha_n}{\lambda\alpha_p} \frac{R_{pn}}{|F_{pn}|} \frac{1}{s_n^*}. \tag{4.23}$$

The fact that a normalized set of weights will obtain an unbiased estimate for the screen implies that the amplitude bias may be expressed as a solution to

$$\alpha_p = \sum_{n=1}^{N} \frac{|F_{pn}||s_n|^2}{\lambda} \alpha_n. \tag{4.24}$$

Because of the Toeplitz structure of F, and the fact that $|F_{pn}|$ decreases off the main diagonal, any solution α_p of Eq. (4.24) will decrease as a function of p when p moves towards the edges of the array. If $|F_{pn}|$ decreases monotonically, then α_p will also decrease monotonically from a maximum in the central region of the array. The filter amplitude is therefore an estimate for an apodized version of the screen amplitude. This apodization has previously been discussed,[16] but the expression for the apodization is new.

In general, when F is not real, the relationship between h_p and s_p is more complicated. It is, however, possible to show that an iterative transmit-beam aberration correction procedure will converge to a h_p which has a phase that concurs with the screen.[16] Applying the correct phase for aberration correction will result in a F which satisfies $F_{pn} = |F_{pn}|$. The preceding argument may then be used to assert that an apodized amplitude estimate is also obtained.

By omitting the phase of F_{pn}, an error is introduced in the MBFO estimate of the screen. Equation (4.10) can be written as

$$\hat{s}_p = \sum_{n=1}^{N} W_{pn} \frac{\tilde{R}_{pn}}{|F_{pn}|} \frac{e^{-i\Delta_{pn}}}{\hat{s}_n^*}, \tag{4.25}$$

where Δ_{pn} is the phase of F. Neglecting this phase will therefore, in general, contribute both to a phase and an amplitude error in the estimation of $\tilde{s}_p$ from Eq. (4.10). Assuming the transmit-beam iteration process converges to the true phase of s_p, as discussed above, F will be real valued and $\hat{s}_p$ becomes by definition equal to $\tilde{s}_p$.

Arrival-time and amplitude estimates

After obtaining an estimate at the center angular frequency, ω_0, for the scatterer-independent screen s_p and the energy maximizing filter h_p, using the MBFO and the EFE estimator respectively, arrival-time and amplitude fluctuations were calculated in a standard way.[15]

Note that although in the presented work only arrival-time and amplitude fluctuations were used, both the MBFO and the EFE may be employed to estimate a phase and amplitude aberration correction filter for all frequency components in the signal.

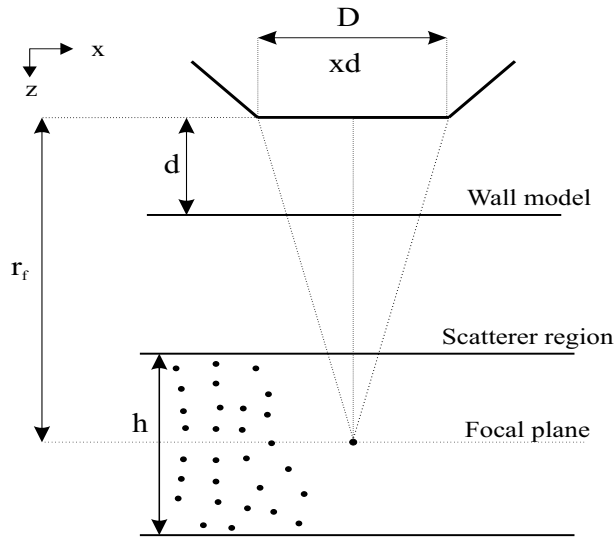

Figure 4.1: An ultrasound pulse was propagated from the transducer (xd), through a body wall to a scattering region. Scattering was computed according to the Born approximation and propagated back through the body wall to the transducer.

IV Simulations

The simulations presented in this article were performed using the two-dimensional (2D) simulation setup shown in Fig. 4.1. An angular spectrum operator was used for homogeneous propagation of the simulated signals.[5] A beam was propagated from the transducer through a body wall model to the scattering region. There it was scattered according to the Born approximation and propagated back to the transducer.

Eight body wall models were generated using equally spaced time-delay screens, filtered and tuned to obtain characteristics according to abdominal wall measurements.[23] The body wall models were also used in Ref. 5. A thorough description of the body wall models is offered in this reference.

The point source simulations were of a one-way nature: a point source was situated at the position of maximum energy of the transmitted beam in the focal plane for each of the aberrators. An emitted pulse from the source, identical to the transmit pulse from the array, was propagated to the array and processed to obtain a reference for the arrival-time and amplitude fluctuations.

IV.A Simulation parameters and data processing

The simulations were implemented in MATLAB. The simulation domain was 10.24 cm in the lateral direction (x-direction in Fig. 4.1) with a resolution of 0.2 mm. To avoid reflections at the edges of the spatial domain due to the FFT being periodic, the signal was tapered to zero with a raised cosine window over a 2.54 cm wide band. The sampling frequency was 35.1 MHz providing a time window of 58.3 µs. The transmitted pulse had a center frequency of 2.5 MHz and a −6 dB bandwidth of 1.5 MHz. An array aperture size of 20 mm with point-like elements was chosen. The focal depth of the array was set to 60 mm. The medium through which the signals were propagated had a speed of sound equal to that of water; 1523 m/s. Geometric focusing was removed from all received signals prior to further processing of the results.

To generate a realistic speckle signal, an area of 30.5 mm (time window of 20 µs), centered with 15.25 mm to each side of the focal plane was used as a scattering region (see Fig. 4.1). The scatterer density was approximately 1600 scatterers per square centimeter. The scatterers were uniformly distributed in space, and had a Gaussian distributed reflection strength.

For each transmit-beam iteration, scattering from twenty independent realizations of the scattering region were simulated for the purpose of cross-spectrum estimation.

Estimation of arrival-time fluctuations for the point source simulation was performed with a phase front tracking algorithm.[5] The method has proved to yield accurate estimates of the wavefront, and is not sensitive to waveform deformation which occurs behind the wavefront.

For all arrival-time fluctuation estimates presented in this article, a linear fit was subtracted in order to remove refraction steering of the beam.

Amplitude fluctuations from the point source simulations were determined by taking the Fourier transform of the received signal on each element as a function of time. The amplitude on each element of the array was calculated as the arithmetic mean of the amplitudes of the now frequency-dependent signal, over a band of frequencies ranging from 2-3 MHz. This band was chosen empirically.

In order to evaluate the accuracy of the estimation methods, the relative L^2 distances between arrival-time and amplitude estimates and their respective references obtained from the point source simulations were calculated. The L^2 distance was normalized with respect to the L^2 norm of the reference, and was thus calculated as

$$d(x, x_{\mathrm{ref}}) = \sqrt{\sum_{i=1}^{N} |x_i - x_{i,\mathrm{ref}}|^2} \Bigg/ \sqrt{\sum_{i=1}^{N} |x_{i,\mathrm{ref}}|^2} \ . \tag{4.26}$$

Here x is the arrival-time or amplitude estimate, and x_{ref} is the reference value obtained from the point source simulations. The mean value was subtracted from all estimates prior to the calculation of the L^2 distance.

For the comparison to be useful, the amplitude estimates and the point source reference need to have equal power. Assuming the estimated values for the amplitude fluctuations are proportional to the reference, a gain factor α may be defined as

$$\hat{\mathbf{a}} = \alpha \mathbf{a}. \tag{4.27}$$

Here $\hat{\mathbf{a}}$ is the estimate and $\mathbf{a}$ the point source reference. The gain factor was determined by minimizing the error between the reference and the estimate

$$\alpha = \frac{\hat{\mathbf{a}}^T \mathbf{a}}{\mathbf{a}^T \mathbf{a}} \ . \tag{4.28}$$

To ensure equal power, the estimated arrival amplitudes were then scaled using the gain factor, prior to the calculation of the relative L^2 distance.

The focusing criterion was calculated according to the derivations by Mallart and Fink.[11] They defined a focusing criterion as

$$C = \frac{\int_{-\infty}^{+\infty} \left(\sum_{p=1}^{N} y_p(t - \tau_p) \right)^2 \mathrm{d}t}{N \cdot \sum_{p=1}^{N} \int_{-\infty}^{+\infty} y_p^2(t) \mathrm{d}t} \ , \tag{4.29}$$

where N is the number of elements on the receiving array. Liu and Waag[10] independently proposed a similar criterion denoted the *waveform similarity factor*.

For a point source, the value of C lies between 0 and 1. For an incoherent medium Mallart and Fink showed that the maximum value of C is 2/3. Note that C can only attain its maximum value if τ_p is properly estimated.

The focusing criterion was, as earlier described, used to evaluate the convergence of the iterative aberration correction procedure, along with the widths of the average receive coherence function introduced by Lacefield and Waag.[14]

The average coherence function for the received signal, from now on denoted *coherence function*, was calculated as

$$\overline{w}_{p-n} = \frac{1}{N_\Delta} \sum_{N_\Delta} \tilde{w}_{pn} = \frac{1}{N_\Delta} \sum_{N_\Delta} \frac{\tilde{R}_{pn}}{\sqrt{\tilde{R}_{pp}\ \tilde{R}_{nn}}} \ , \tag{4.30}$$

where N_Δ denotes the number of element pairs with separation $p - n$. Note that the coherence function was only calculated for the center frequency of the signal. The magnitude of the coherence function was interpolated to a resolution of 0.05 mm sampling, before the width of the magnitude of the coherence function was calculated at levels 0.6 and 0.4.

All received data were corrected using arrival-time fluctuation estimates, obtained by the estimators, prior to the calculation of the focusing criterion C and the coherence function. For the focusing criterion, the linear fit of the arrival time estimates was not subtracted prior to receive correction.

Beam profiles in the focal plane of the array were acquired as the rms value of the temporal signal at each spatial position. These profiles were used for the visual evaluation of the effect of the different aberration correction methods.

V Results

Simulations were performed using eight different aberrators. To limit the amount of presented data, detailed results are only offered for two of the aberrators; w6 and s6. The w6 and s6 aberrator represent weak and strong aberration respectively, and are representative for overall performance of the iterative transmit-beam aberration correction. Only the parameter C is presented for all aberrators, as this proved to be the best criterion by which to quantify the transmit-beam iteration results.

In all the results presented, MBFO and EFE denote results obtained using the corresponding method for estimating arrival-time and amplitude fluctuations.

All results in this section are labeled with an iteration number. The iteration number is defined according to the transmit-beam. One transmit-beam iteration is defined as consisting of an estimation of arrival-time and amplitude fluctuations; an application of these estimates to a transmit-beam in order to obtain a corrected transmit-beam profile; and finally receiving scattering generated by the corrected transmit-beam. In this labeling scheme, *iteration 0* refers to the initial transmit-beam, where no aberration correction is applied. The arrival-time and amplitude fluctuations estimated using scattering created by the transmit-beam from iteration 0 are used to form the first truly corrected transmit-beam. These arrival-times, amplitudes, and the resulting beam profiles are thus labeled *iteration 1*, and so on.

Figure 4.2 shows beam profiles in the focal plane of the array. For the w6 aberrator, the corrected beam profiles appear to converge after two iterations for both methods. The resulting beam profiles are very well corrected and close to the unaberrated profile. In the case of the s6 aberrator, one additional iteration is required for MBFO to obtain the same results. Since only minor changes occur from iteration 2 to iteration 5 for the w6 aberrator, and from iteration 3 to iteration 5 for the s6 aberrator, only results from iterations 0, 1, 2 and 5 are presented.

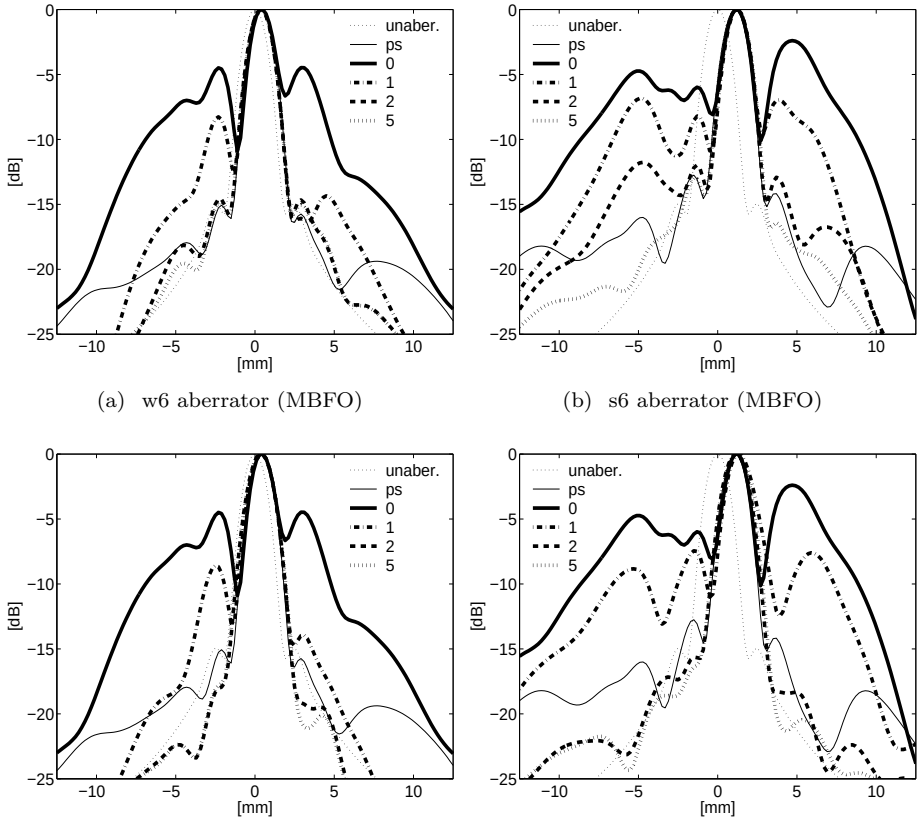

(a) w6 aberrator (MBFO)

(b) s6 aberrator (MBFO)

(c) w6 aberrator (EFE)

(d) s6 aberrator (EFE)

Figure 4.2: Beam profiles in the focal plane for the w6 and s6 aberrators. Zero on the horizontal axis represents the center axis of the array. All profiles are normalized to their maximum value. The reference profile represents the situation with no aberration, and the profile denoted ps shows correction using the point source reference. The numbers in the legend refer to the iteration number of the correction procedure, where the 0-iteration profile is the uncorrected transmitted profile.

The estimated time-delay and amplitude fluctuations used to produce the corrected beam profiles in Fig. 4.2 are shown in Figs. 4.3 and 4.4. The visual impression of convergence for the estimates is the same as for the beam profiles. It is worth noting, however, that the time-delay estimate is also very accurate after two iterations for MBFO applied to the s6 aberrator. The amplitude improves significantly at the third iteration. The improvement between iterations 2 and 3 for the beam profile is thus mainly explained by an improved amplitude estimate.

The relative L^2 distance between the estimated arrival-time/amplitude and the respective references was computed for each iteration. Figure 4.5 shows how the distance decreases for the first two iterations. In the case of the w6 aberrator the distances level out after the second iteration. For the s6 aberrator, the distance for the amplitude levels out in the same manner as for the w6 aberrator. The distance for the arrival-time, however, increases after the second iteration. This is related to the discontinuities in the arrival-time estimates observed in Fig. 4.3. The value at which the L^2 distance levels out for the EFE amplitude estimate is significantly higher than for the MBFO estimate. This is explained by the fact that the EFE amplitude is

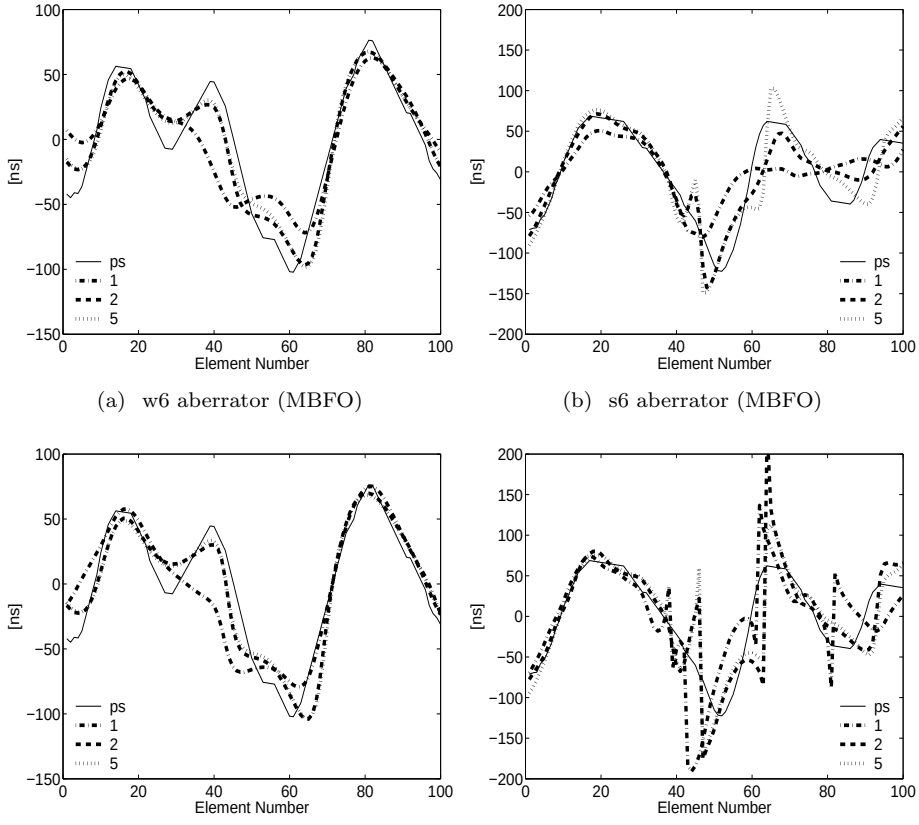

(a) w6 aberrator (MBFO)

(b) s6 aberrator (MBFO)

(c) w6 aberrator (EFE)

(d) s6 aberrator (EFE)

Figure 4.3: Arrival-time fluctuations for the w6 and s6 aberrators. The horizontal axis is given in array elements. The curves denoted ps are the references obtained from the point source simulations. The numbering of the arrival-time curves in the legend corresponds to the iteration number of the corrected transmitted beam in Fig. 4.2. Arrival-time curve number 1 was thus used to obtain beam profile number 1 in Fig. 4.2.

apodized relative to the screen, while the MBFO is not.

The magnitude of the coherence functions, and the coherence widths for the received scattering, are presented in Figs. 4.7 and 4.6. The coherence widths at different levels increase gradually with iteration, demonstrating an increased degree of spatial coherence in the receive signal.

The focus quality parameter for all aberrators is presented in Fig. 4.8 as a mean value and a standard deviation. These were calculated using the twenty independent receive signals for each iteration. In concurrence with the theoretical foundation for the parameter,[11] the strong increase in the focus quality parameter C corresponds to the improved focus apparent in the beam profiles in Fig. 4.2. With the exception of s8, convergence was obtained after 1-3 iterations using either algorithm.

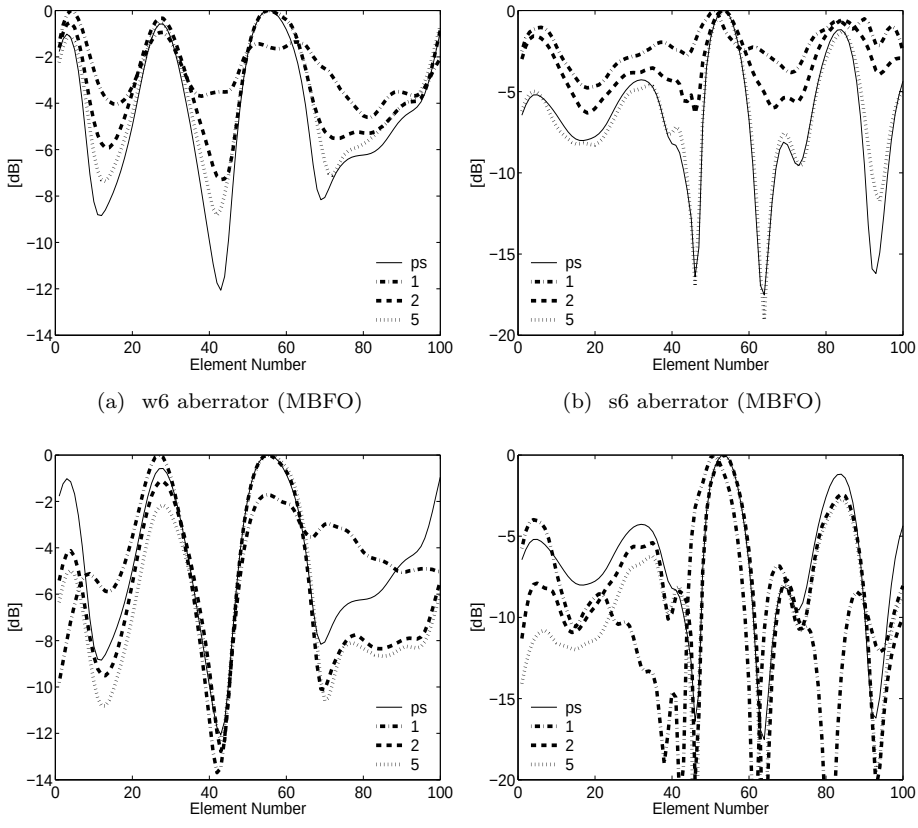

(a) w6 aberrator (MBFO)

(b) s6 aberrator (MBFO)

(c) w6 aberrator (EFE)

(d) s6 aberrator (EFE)

Figure 4.4: Amplitude fluctuations for the w6 and s6 aberrators. The horizontal axis is given in array elements. The curves denoted ps are the references obtained from the point source simulations. All amplitude fluctuation curves are normalized to their maximum value. The numbering in the legend is the same as in Fig. 4.3.

VI Discussion

As shown in this article, both the MBFO and EFE algorithm use an average of element signals as the reference value in a correlation process, in other words, a beamforming correlation process. This is conceptually similar to the speckle brightness method,[22] speckle look-back,[12] the beamsum-channel correlation method,[9] and the scaled covariance matrix algorithm[24] for phase estimation. The principal difference is that both methods presented here can estimate both phase and amplitude aberration at all frequency components, and thus represents a generalization of the above described methods.

In order to obtain a correlation based estimate, a stable reference signal is needed. The variance of the estimate will be as low as possible when the reference signal is coherent with the backscatter signal. In the case of the MBFO estimator, a separate reference b_{kp} is used for each element p. The EFE, on the other hand, uses the same reference, β_k, for all elements.

The MBFO estimate utilizes the signal model to create signals of equal strength at each element by factoring out the effect of the aberration amplitude. It then forms a reference which is coherent with the signal at element p by explicitly applying the coherence function as weights

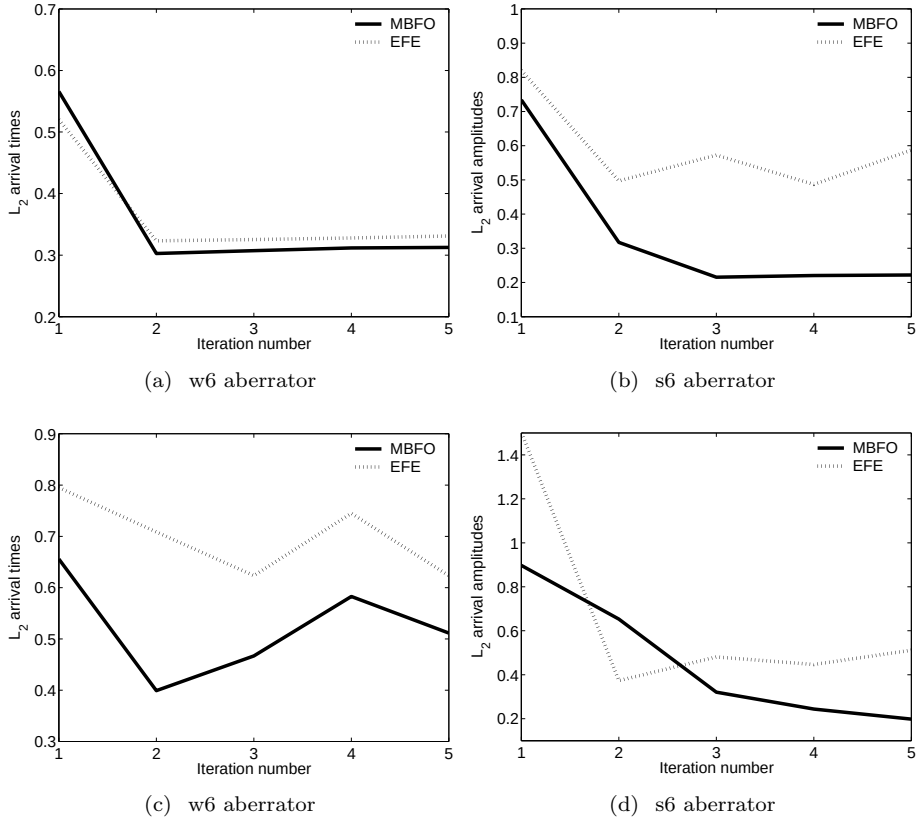

(a) w6 aberrator (b) s6 aberrator

(c) w6 aberrator (d) s6 aberrator

Figure 4.5: Relative L^2 distance between point source reference and estimate for w6 and s6 aberrators. The top row shows the L^2 distance for arrival-time fluctuations, and the bottom row for amplitude fluctuations. The horizontal axis indicates the iteration number according to Figs. 4.3 and 4.4.

in a weighted average.

The weight function works as a sliding window which efficiently implements a subaperture processing, automatically selecting an appropriate subaperture for the beamformer output from a variance perspective [confer Eq. (4.16)]. The weighting also ensures that the beamformer output is highly correlated with the element signal where the estimation occurs. Since the subaperture slides across the array, it is desirable with an inverse amplitude filtering in order for the reference signal to attain the same average energy level for each subaperture.

The EFE constructs one signal which is utilized as a common correlation reference for all element signals across the aperture. To this end no signal model is employed directly. Instead the reference signal is formed as a weighted coherent sum of the element signals. Assuming no amplitude damping due to absorption, a backscatter signal of large amplitude is the result of constructive interference. A low-amplitude backscatter signal, on the other hand, is the result of destructive interference. As a result, high-amplitude signals will resemble each other more closely than low-amplitude signals. The accuracy with which the aberration correction filter may be estimated, is directly connected to the degree of coherence between an element signal and the reference. In order to form a good estimate, it is therefore of importance to form a reference signal which is highly correlated with the element signals. Furthermore, because signals of high

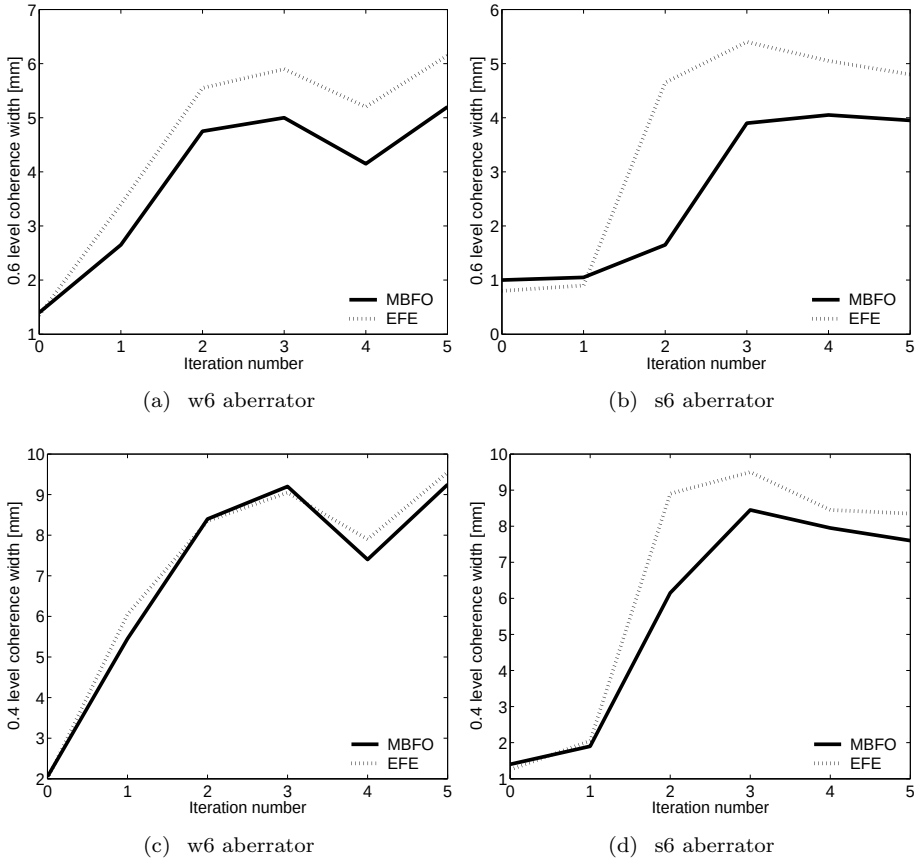

(a) w6 aberrator (b) s6 aberrator

(c) w6 aberrator (d) s6 aberrator

Figure 4.6: Coherence widths for the w6 and s6 aberrators at levels 0.6 and 0.4. The horizontal axis shows the iteration number as explained in Fig. 4.7.

amplitude contribute more to the overall focus quality than low-amplitude signals, it is most important to obtain an accurate estimate for the correction of high-amplitude signals. The weighted coherent sum of element signals should emphasize element signals of large amplitude in order to achieve this. To what degree high amplitudes should be emphasized over low amplitudes is determined by the L^2 norm used when maximizing the expected energy of $\mathcal{L}_h\mathbf{y}$ in Eq. (4.14).

As described in Sec. IV.A, for each transmit-beam iteration, scattering from twenty new realizations of the scattering region were simulated. The objective of this article was to study iteration of transmit-beam aberration correction. For this purpose, a proper estimate of the cross-spectrum [Eq. (4.6)] was desired. For practical purposes, using twenty transmit-beams for each estimate is unfeasible in a real-time scanning environment. However, if only a time-delay and amplitude aberration correction filter is sought, appropriate model-based averaging of the cross-spectrum over a wider frequency band will yield a similar effect to acquiring independent realizations. In this situation the number of independent realizations may therefore be greatly reduced. An important issue for implementation will be to determine the number of receive-signals necessary to obtain an adequate estimate.

The transmit-focus of an ultrasound beam may be quantified by measuring the width of the transmit-beam profile. The beam profiles shown in Fig. 4.2 display a significant improvement

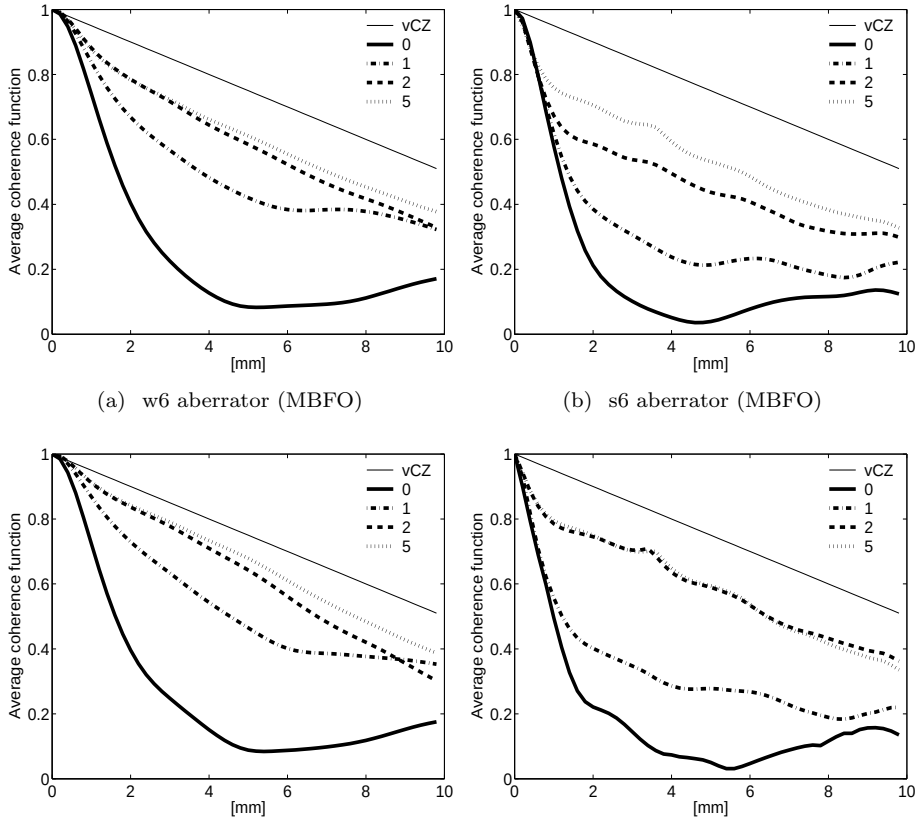

(a) w6 aberrator (MBFO)

(b) s6 aberrator (MBFO)

(c) w6 aberrator (EFE)

(d) s6 aberrator (EFE)

Figure 4.7: Absolute value of the average coherence function for the w6 and s6 aberrators. The numbering of the curves corresponds to the iteration number, *i.e.* coherence functions for the received signals obtained using a transmit-beam with the same number in Fig 4.2. The curve denoted vCZ indicates the theoretical upper bound for the coherence based on the van Cittert-Zernike theorem for a homogeneous medium. All received signals were corrected using the estimated arrival-time fluctuations prior to calculating the coherence function.

in focus quality as a result of the iterative transmit-beam correction process. Furthermore, the convergence towards an almost-ideal beam profile width is rapid. There is, however, a slight offset in the peak of the beam profiles.

This shift, particularly noticeable for the s6 aberrator, is produced by a refraction of the transmitted beam. In this two-way imaging system, where reciprocity implies that the back-scattered beam will experience the same refraction as the transmitted beam, the associated shift of the beam profile is not observed from the transducer array. Dealing with refraction of the beam due to aberration through the body wall remains an issue for further research.

For the w6 aberrator, both estimation methods yield transmit-beams with the same degree of focus after two transmit-beam iterations as those obtained using the point source reference for aberration correction. Beyond two iterations, no significant improvement of the beam profiles is achieved. In the case of the s6 aberrator, three iterations are required for the MBFO estimate to achieve as good a correction as the point source reference. Beyond this point, no significant

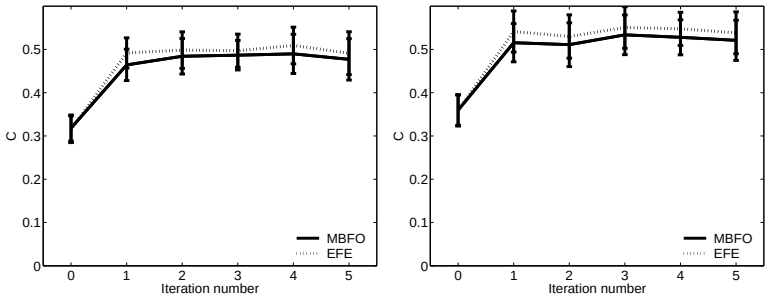

(a) w2 aberrator

(b) w4 aberrator

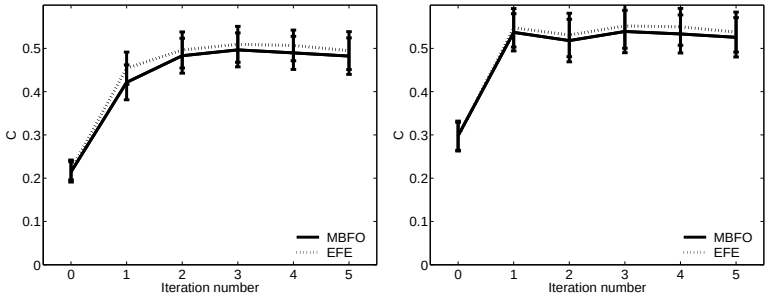

(c) w6 aberrator

(d) w8 aberrator

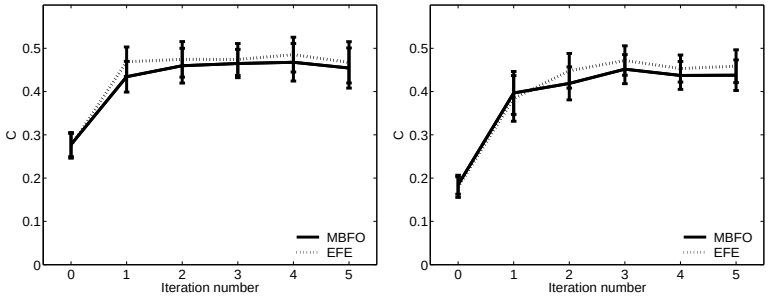

(e) s2 aberrator

(f) s4 aberrator

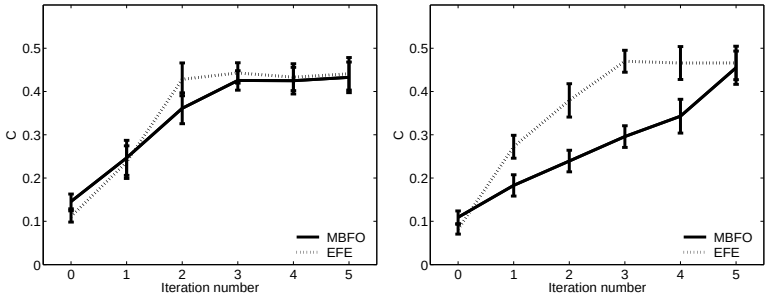

(g) s6 aberrator

(h) s8 aberrator

Figure 4.8: Mean value and standard deviation of the focus quality parameter C computed for all wall models. The horizontal axis shows the iteration number as explained in Fig. 4.7. The error bars display the standard deviation. All received signals were corrected using estimated arrival-time fluctuations prior to calculation of the focusing criterion.

improvement can be found in the transmit-beam profiles. The EFE estimate does not improve the beam profile significantly after the second iteration.

Convergence for the beam profiles is accompanied by an apparent convergence also for the time-delays and amplitudes shown in Figs. 4.3 and 4.4. After approximately two iterations, no essential change occurs in the phase estimates for either method. Amplitude estimates are improved with further iteration for the MBFO algorithm, but for the EFE estimate more than two iterations are not required.

In the weakly aberrated case, the time-delays obtained using both estimation methods are very close to the point source reference. For the s6 aberrator, the estimated arrival-times exhibit discontinuities, while the pointsource reference does not. The discontinuities are linked to waveform deformation in the received signals for the s6 aberrator.[15]

Waveform deformation results in low signal amplitudes, and causes discontinuities in the arrival times between adjacent element signals.[4,5]

The MBFO algorithm produces amplitude estimates which are close to the point source reference both for the w6 and s6 aberrators. For the s6 aberrator the corrected beam profile is improved significantly for the third iteration using MBFO, even if the time-delay estimate does not change much from the second to the third. This improvement must therefore be the result of the improved amplitude estimate.

This observation is in accordance with the predicted amplitude error as a result of omitting the phase of F_{pn} in Eq. (4.12). Transmitting with a correct phase filter will, according to Eq. (4.4) produce an F_{pn} which is real. The amplitude error will therefore not be introduced in the MBFO estimate based on the corrected backscatter, resulting in a good amplitude estimate.

Due to the discontinuities of the arrival-time estimates, and the apodization of the EFE amplitude relative to the screen, the L^2 distance remains large also after iteration (see Fig. 4.5). Therefore, the L^2 distance does not adequately reflect the aberration correction capabilities of the associated correction filter.

Rigby *et al.*[9] obtained convergence after three or four iterations, but the convergence quality of the estimates is not certain as no reference could be provided for the subjects used in the study.

The number of independent signals used for estimating covariance or cross-spectrums will influence the accuracy with which arrival-times and amplitudes are estimated. This will affect the convergence rate. In Ref. 5 it was shown that introducing amplitude correction in addition to time-delay correction was of vital importance for the side-lobe level of the beam profiles. Proper amplitude correction will thus increase the spatial coherence in the received signal, and reduce the number of iterations required for the aberration correction algorithm to converge. Both of the aforementioned issues could be the catalyst for the overall improved convergence rates in this work compared to the results obtained in Ref. 9.

Based on the van Cittert-Zernike theorem, the width of the coherence function for the receive signal may be used to determine the width of the associated focus. Figure 4.7 clearly shows an increasing overall width of the coherence functions as a result of iteration for both aberrators and both estimation methods. The visual impression is that performing two iterations is sufficient to obtain almost maximum coherence widths. Beyond this, only minor improvements occur. Thus the coherence functions do give the correct impression of the converging beam profiles for the iteration process. However, the difficulty herein is determining at which level the width of the coherence function should be measured. As seen in Fig. 4.6, the choice impacts on the width curves dramatically. This renders the coherence width less attractive for determining the point of convergence.

The parameter C was originally introduced as a measure to quantify the degree of focusing for a given transmit-beam based on the backscatter signal. When applied to the iterative transmit-

beam correction procedure, the value for C is observed to increase initially, and then level off at the point beyond which no practical improvement of the beam profile is achieved. (See Figs. 4.2 and 4.8.) The point of convergence can therefore be found by identifying the point where this curve levels off. Furthermore, the theoretical upper bound for this parameter may be used as an indication of how close the corrected beam profile is to an ideal transmit-beam profile. The iteration may therefore be set to terminate when a given threshold for C has been reached.

Based on the beam profiles presented for the w6 and s6 aberrator, it is clear, from the focus quality parameter, that the beam profiles for the rest of the aberrators were very well corrected. This was confirmed by visual inspection of the profiles. Further, the results indicate that for $C > 0.4$, aberration correction of the transmit beam is close to the correction obtained with the point source reference for these aberrators.

An added advantage of using the parameter C to determine convergence, is the relatively low computational complexity involved. This, combined with the fact that it is computed from information readily available in the backscatter signal, without requiring knowledge of a point source/scatterer, may therefore enable the parameter C to be implemented in an aberration correction procedure without much additional effort.

For the s8 wall, the MBFO algorithm requires five iterations for proper convergence. For this aberrator, the uncorrected beam profile had very high side-lobe levels, where one side-lobe was higher than the main lobe. This caused the MBFO algorithm, initially, to focus on this side-lobe. Through transmit-beam iteration, the beam profile was improved and a linear slope was detected at iteration 3. Removing the linear component of the arrival time estimate then focused the beam correctly (observed from the point source simulations). For the EFE, this effect is avoided by choosing the eigenvector associated with the second largest eigenvalue because this had a smaller linear component in the phase.[16]

In the presented results the acoustic scatterers are δ-correlated. This ensures that the acoustic backscatter is a Gaussian stochastic process, at least asymptotically, and is a natural assumption in many imaging situations. Furthermore, the scattering intensity was the same everywhere. This is a good approximation when imaging homogeneous organs such as liver and spleen. The derivation of the MBFO shows that a spatially variable scattering intensity will affect the estimate in the form of a different cross-spectrum for the unaberrated backscatter, F_{pn}. In this situation an estimate for F_{pn} may not be obtained using the van Cittert-Zernike theorem unless the scattering intensity is known. An alternative approach would be to utilize the fact that, according to the signal model, the magnitude of the coherence is proportional to $|F_{pn}|$. The EFE will focus the corrected beam also in the situation with spatially variable scattering intensity. However, the focus will be determined by a product of the scattering intensity and the intensity of the transmit-beam, and not the transmit-beam alone. A combination of selecting the eigenvector with lowest linear component and removing the remaining linear slope will focus the aberration-corrected transmit-beam at the right location. An aberration correction filter may therefore be obtained by either estimation method also in the case of variable scattering intensity. As a consequence of iterative transmit-beam correction the focal zone will narrow. The assumption of a constant scattering intensity will thus be increasingly better.

In this article, theory and simulations have been presented for ultrasound propagation in a non-absorbing medium. If the medium exhibits absorption which is homogeneous, *i.e.*, the absorption is the same everywhere in the medium, it can still be shown that a match filter is ideal for aberration correction [Ref. 17 (Ch. 11)]. In the presence of heterogeneous absorption, however, the aberration contributed by the absorption should be corrected using an inverse filter.[25,26] In a practical situation, where both heterogeneous absorption and heterogeneous speed of sound are contributing factors, a combination of an inverse filter and a match filter, *e.g.* a Wiener filter, would probably result in best overall performance.

The results presented here were obtained by simulating sound propagation in 2D. This represents a simplification in that out-of-plane aberration/scattering effects are not included. However, combined experimental and simulation studies of wavefront aberration through the abdominal wall have concluded that important aspects of wavefront aberration are observed also in 2D simplified models.[27] Although details may vary, the qualitative aspects of the results are expected to hold, also in a real-world situation.

Although 2D simulations are assumed to give an accurate picture of the aberration correction process, in order to perform aberration correction in a real-world setting certain issues such as element size and directivity must be taken into account.

The array elements must be smaller than the correlation length of the aberration. In the azimuth direction this requirement will generally be much weaker than standard beamforming requirements. However, the same requirement must also hold in the elevation direction. In practice, this means that either 1.75D or 2D arrays are needed.

For large apertures, element directivity could reduce the signal-to-(electronic)-noise ratio (SNR) along the edges of the array.[14] This will, in turn, lead to a reduced spatial coherence in the measured signal, and thus a less accurate estimate of the correction filter. Since the correlation length of the aberration generally is much larger than the standard beamforming requirement, element signals may be combined in subapertures prior to aberration correction, thereby increasing the SNR. It is also noted that standard apodization will reduce the contribution from the elements along the edges of the array. The reduced accuracy of the filter estimate will therefore only have a limited impact.

Noise was not introduced to the signals used in this study. Both algorithms used here average an aberration corrected signal over a subaperture, or the entire aperture, to create a stable reference for the correlation process. Since electronic noise is uncorrelated between elements, averaging over a subaperture will reduce the noise level in the reference signal.[12] Furthermore, the SNR in standard ultrasound imaging is generally high. Walker and Trahey[28,29] showed that an SNR greater than 15 dB had little effect on the error of correlation-based phase estimates.

The effect of acoustic reverberation noise also represents a challenge, mainly because it is highly correlated both in the temporal and spatial directions. It is beyond the scope of this article to study reverberation noise.

VII Conclusion

Iteration of transmit-beam aberration correction with a time-delay and amplitude filter has been investigated. Two correlation-based algorithms for estimating arrival-time and amplitude fluctuations from random scatterers were employed. The resulting estimates were used to construct a time-delay and amplitude filter for aberration correction.

Results from simulations using eight aberrators, emulating the human abdominal wall, indicate overall convergence for both estimation methods after 1-3 iterations. Corrected beam profiles obtained after convergence were close to the unaberrated profiles. Transmit-beam iteration thus produced substantial improvements for all investigated aberrators.

In order to quantify the convergence, the focusing criterion C developed by Mallart and Fink,[11] and the width of the average coherence function[14] were calculated for the acoustic backscatter at each iteration.

Both the focusing criterion C and the coherence functions gave the correct impression of convergence for the transmit-beam profiles. However, there is an inherent problem of selecting an appropriate level at which to measure the width of the coherence function.

The focusing criterion C, on the other hand, is not associated with such difficulties. It is shown

to determine accurately when convergence of the aberration correction procedure is achieved. The theoretical upper bound for C may be used as a criterion for termination of the transmit-beam iteration process. It is therefore the most attractive criterion for studying transmit-beam iteration. Furthermore, as it is inexpensive to compute, C may readily be implemented in an aberration correction scheme without much additional overhead.

Acknowledgments

This work was, in part, supported by the Medicine and Health program of the Research Council of Norway, and partly by the Norwegian University of Science and Technology (NTNU). Professor Harald Krogstad and Dr. Tonni Johansen at NTNU are thanked for useful discussions and comments. The reviewers are thanked for constructive comments that improved this article.

References

[1] S. W. Flax and M. O'Donnell, "Phase-aberration correction using signals from point reflectors and diffuse scatterers: Basic principles," *IEEE Trans. Ultrason. Ferroelectr. Freq. Control*, vol. 35, no. 6, pp. 758–767, November 1988.

[2] M. O'Donnell and S. W. Flax, "Phase-aberration correction using signals from point reflectors and diffuse scatterers: Measurements," *IEEE Trans. Ultrason. Ferroelectr. Freq. Control*, vol. 35, no. 6, pp. 768–774, November 1988.

[3] L. Hinkelman, T. D. Mast, L. A. Metlay, and R. C. Waag, "The effect of abdominal wall morphology on ultrasonic pulse distortion. part i. measurements," *J. Acoust. Soc. Am.*, vol. 104, no. 6, pp. 3635–3649, December 1998.

[4] T. D. Mast, L. M. Hinkelman, M. J. Orr, and R. C. Waag, "The effect of abdominal wall morphology on ultrasonic pulse distortion. part ii. simulations," *J. Acoust. Soc. Am.*, vol. 104, no. 6, pp. 3651–3664, December 1998.

[5] S.-E. Måsøy, T. F. Johansen, and B. Angelsen, "Correction of ultrasonic wave aberration with a time delay and amplitude filter," *J. Acoust. Soc. Am.*, vol. 113, no. 4, pp. 2009–2020, April 2003.

[6] M. Karaman, A. Atalar, H. Köymen, and M. O'Donnell, "A phase aberration correction method for ultrasound imaging," *IEEE Trans. Ultrason. Ferroelectr. Freq. Control*, vol. 40, no. 4, pp. 275–282, July 1993.

[7] S. Krishnan, K. W. Rigby, and M. O'Donnell, "Improved estimation of phase aberration profiles," *IEEE Trans. Ultrason. Ferroelectr. Freq. Control*, vol. 44, no. 3, pp. 701–713, May 1997.

[8] S. Krishnan, K. W. Rigby, and M. O'Donnell, "Efficient parallel adaptive aberration correction," *IEEE Trans. Ultrason. Ferroelectr. Freq. Control*, vol. 45, no. 3, pp. 691–703, May 1998.

[9] K. W. Rigby, C. L. Chalek, B. H. Haider, R. S. Lewandowski, M. O'Donnell, L. S. Smith, and D. G. Wildes, "Improved in vivo abdominal image quality using real-time estimation and correction of wavefront arrival time errors," *IEEE Ultrasonics Symposium*, vol. 2, pp. 1645–1653, October 2000.

[10] D.-L. Liu and R. C. Waag, "Correction of ultrasonic wavefront distortion using backpropagation and a reference waveform method for time-shift compensation," *J. Acoust. Soc. Am.*, vol. 96, no. 2, pp. 649–660, August 1994.

[11] R. Mallart and M. Fink, "Adaptive focusing in scattering media through sound-speed inhomogeneities: The van Cittert Zernike approach and focusing criterion," *J. Acoust. Soc. Am.*, vol. 96, no. 6, pp. 3721–3732, December 1994.

[12] G. C. Ng, S. S. Worrel, P. D. Freiburger, and G. E. Trahey, "A comparative evaluation of several algorithms for phase aberration correction," *IEEE Trans. Ultrason. Ferroelectr. Freq. Control*, vol. 41, no. 5, pp. 631–643, September 1994.

[13] A. P. Berkhoff and J. Thijssen, "Correction of concentrated and distributed aberrations in medical ultrasound imaging," *1996 IEEE Ultrasonics Symp. Proc.*, vol. 2, pp. 1405–1410, 1996.

[14] J. C. Lacefield and R. C. Waag, "Spatial coherence analysis applied to aberration correction using a two-dimensional array system," *J. Acoust. Soc. Am.*, vol. 112, no. 6, pp. 2558–2566, December 2002.

[15] S.-E. Måsøy, T. Varslot, and B. Angelsen, "Estimation of ultrasound wave aberration with signals from random scatterers," *J. Acoust. Soc. Am.*, vol. 115, no. 6, pp. 2998–3009, June 2004.

[16] T. Varslot, E. Mo, H. Krogstad, and B. Angelsen, "Eigenfunction analysis of stochastic backscatter for characterization of acoustic aberration in medical ultrasound imaging," *J. Acoust. Soc. Am.*, vol. 115, no. 6, pp. 3068–3076, June 2004.

[17] B. Angelsen, *Ultrasound imaging. Waves, signals and signal processing.* Trondheim: Emantec, 2000, vol. II, http://www.ultrasoundbook.com.

[18] R. Mallart and M. Fink, "The van Cittert-Zernike theorem in pulse echo measurements," *J. Acoust. Soc. Am.*, vol. 90, no. 5, pp. 2718–2727, November 1991.

[19] T. Varslot, B. Angelsen, and R. C. Waag, "Spectral estimation for characterization of acoustic aberration," *J. Acoust. Soc. Am.*, vol. 116, no. 1, pp. 97–108, July 2004.

[20] M. B. Priestley, *Spectral Analysis and Time Series.* Academic Press, 1988.

[21] T. K. Moon and W. C. Stirling, *Mathematical Methods and Algorithms for Signal Processing.* Upper Saddle River, New Jersey 07458: Prentice Hall, 2000.

[22] L. F. Nock, G. E. Trahey, and S. W. Smith, "Phase aberration correction in medical ultrasound using speckle brightness as an image quality factor," *J. Acoust. Soc. Am.*, vol. 85, no. 5, pp. 1819–1833, May 1989.

[23] L. M. Hinkelman and D.-L. Liu, L. A. Metlay, and R. C. Waag, "Measurements of ultrasonic pulse arrival time and energy level variations produced by propagation through abdominal wall," *J. Acoust. Soc. Am.*, vol. 95, no. 1, pp. 530–541, January 1994.

[24] S. D. Silverstein and D. P. Ceperley, "Autofocusing in medical ultrasound: The scaled covariance matrix algorithm," *IEEE Trans. Ultrason. Ferroelectr. Freq. Control*, vol. 50, no. 7, pp. 795–804, July 2003.

[25] Q. Zhu and B. Steinberg, "Deaberration of incoherent wavefront distortion: An approach toward inverse filtering," *IEEE Trans. Ultrason. Ferroelectr. Freq. Control*, vol. 44, no. 3, pp. 575–589, May 1997.

[26] M. Tanter, J.-L. Thomas, and M. Fink, "Time reversal and the inverse filter," *J. Acoust. Soc. Am.*, vol. 108, no. 1, pp. 223–234, July 2000.

[27] T. Douglas Mast, Laura M. Hinkelman, and Michael J. Orr, V. W. Sparrow, and R. C. Waag, "Simulation of ultrasonic pulse propagation through the abdominal wall," *J. Acoust. Soc. Am.*, vol. 102, no. 2, pp. 1177–1190, August 1997.

[28] W. F. Walker and G. E. Trahey, "A fundamental limit on the performance of correlation based phase correction and flow estimation techniques," *IEEE Trans. Ultrason. Ferroelectr. Freq. Control*, vol. 41, no. 5, pp. 644–654, September 1994.

[29] W. F. Walker and G. E. Trahey, "A fundamental limit on delay estimation using partially correlated speckle signals," *IEEE Trans. Ultrason. Ferroelectr. Freq. Control*, vol. 42, no. 2, pp. 301–308, March 1995.

Chapter 5

Variance analysis of arrival time and amplitude fluctuation estimates from random speckle signal

S. Måsøy[1], T. Varslot[2], B. Angelsen[1]
1)Department of Circulation and Imaging, NTNU
2)Department of Mathematical Sciences, NTNU.

An aberration estimation algorithm, previously developed in the frequency domain, is implemented in the time domain. The algorithm is used to estimate arrival time and amplitude fluctuations with signals from random scatterers. The method is based on a correlation process. The correlation is averaged using signals from independent realizations of the scatterers.
Simulations have been performed to investigate the variance of the estimates. Stability differences between the frequency and time domain implementation are also explored. Eight body wall models, emulating the human abdominal wall, were used for this purpose. The variance was investigated as a function of the number of independent scatterer realizations, used to obtain an estimate. Such signals may be acquired by imaging moving scatterers, *e.g.* blood or contrast agent. Alternatively they can be obtained by using different non-overlapping beams from a sector/linear scan.
The results show only minor differences between the two implementations with respect to stability. The standard deviation of arrival time and amplitude fluctuation estimates decrease, when the number of independent signals increase. Using only one signal for estimation produces a relatively high standard deviation, but an iterative transmit-beam aberration correction scheme still converges to a properly corrected focus.

I Introduction

The back-scattered signal in ultrasound medical imaging is dependent on the scatterers spatial position. The scatterers are randomly distributed in space, and the distribution changes for each direction of the beam. Tissue contains smaller or larger structures, and the received signal is therefore correlated between each direction of the transmitted beam. The degree of correlation varies in different types of tissue due to variation in size of the tissue structures.

In Ref. 1, a method for estimating arrival time and amplitude fluctuations using backscatter from random scatterers was developed. The estimated arrival time and amplitude fluctuations were used in a time-delay and amplitude aberration correction filter. The method used cross-spectrum information to perform the estimation. The cross-spectrum estimate was obtained by averaging a number of statistically independent receive signals. The signals were acquired from independent realizations of the insonified scattering region. The result of this study indicated that for a distributed aberrator, using twenty independent signals did not produce satisfactory estimates of the aberration. The results indicated that an iterative transmit-beam aberration correction process was necessary to obtain proper aberration correction of the ultrasound beam.

Iteration of transmit-beam aberration correction (transmit-beam iteration) was studied in Ref. 2. Here, the same estimation method as in Ref. 1 was investigated. Results showed that using a sufficient number (20) of independent receive signals in order to estimate the cross-spectrum, the transmit-beam iteration process converged for eight different aberrators representing cases of weak and strong aberration. After convergence, the quality of corrected focus beam profiles were close to the correction with estimates obtained from a point source.

Employing a transmit-beam iteration process using twenty receive signals for correction of each transmit beam, is unfeasible for real-time imaging. It is therefore important to investigate the number of independent signals necessary, to obtain a stable and adequate estimate for a transmit-beam iteration process to converge. How the stability affects the quality of the converged aberration corrected transmit beam profile, is also important.

There are two main objectives of the work presented in this article:

1. Introduce a time domain implementation of the aberration estimation algorithm presented in Ref. 1, and explore the difference between the time and frequency domain implementation.

2. Investigate the variance of arrival time and amplitude fluctuation estimates as a function of the number of independent receive signals used for averaging cross-correlations (time domain) and cross-spectra (frequency domain).

Necessary assumptions made in the time domain implementation make the algorithm different from the frequency domain implementation, and a sub-goal of the presented work is to study how these differences affect the variance in the obtained estimates.

In a practical situation, statistically independent signals can be obtained by scanning a region containing moving scatterers, *e.g.*, the heart or a large blood vessel. When ensuring all blood cells to be replaced for each transmitted beam, the received signal can be assumed to be spatially totally incoherent (δ-correlated) due to the small size of blood cells. Ultrasound contrast agents can be used to enhance such a signal.

Alternatively, it is possible to use signals from different regions in a sector scan.[3–5] By choosing beams which do not overlap, each received signal can be assumed to be independent. If the beams are overlapping, *e.g.*, if neighboring beams are used, the signals will not be totally independent, and some correlation will exist between them.

In Ref. 3, a sum of absolute differences (SAD) method was developed for estimating relative phase errors between adjacent array elements. The variance of the estimator was investigated by using signals from 5 different nonadjacent scan angles, and two different focusing depths, in a scattering phantom. The obtained estimates were used in an iterative adaptive aberration correction scheme, and the variance of the estimates decreased sharply between the first and second iteration. Only smaller changes were observed when more iterations were performed.

Walker and Trahey[6,7] derived the Cramér-Rao lower bound for correlation based time-delay estimation from speckle signals. They investigated the limit as a function of several parameters

such as correlation coefficient, window length, signal to noise ratio, bandwidth, and frequency. Their results showed that the lower bound for the variance of a time-delay estimate increased rapidly with a reduced correlation coefficient.

Ng *et al.* [8] compared the neighbor correlation method introduced by Flax and O'Donnell[9] with a partial array reference correction method, and showed that the latter method was more stable in the presence of noise. Overall the partial array reference correction method performed better than neighbor correlation and had a lower variance in the estimates as a function of signal to noise ratio.

Rigby *et al.* [4] performed *in vivo* adaptive aberration correction with a time-delay filter using a 1.75D array. In order to reduce image artifacts due to strong off-axis scatterers, they averaged time-delay estimates over 5 transmit-beams in a linear array scan. The beamsum channel-correlation method used for estimating time-delays proved to adaptively converge to a stable estimate, producing improved image quality in most of the investigated subjects.

Lacefield and Waag[10] investigated estimates of the coherence using a 2D array. They found that the coherence of data acquired on neighboring elements was not changed by time-delay correction of transmit and receive beams. On the other hand, time-delay correction improved the coherence in signals received over larger element separation, supporting the use of several array elements for correlation estimation. Coherence is an important measure of the accuracy of correlation-based time-delay estimation methods. It is directly linked to the lower bound of the variance of such an estimate,[11] and to the variance of the magnitude and phase of the cross-spectrum.[12]

Varslot *et al.* [5] estimated cross-spectra using independent measurements obtained from different focal points inside the isoplanatic patch with a 2D array. The purpose was to use the estimated frequency dependent phase and magnitude of the cross-spectrum for aberration correction. Increasing the number of independent measurements from 13 to 75 gave a significant improvement of the spectral estimates. It reduced the 95% confidence intervals, thus improving the stability of the estimate. Their results also showed that the major part of the frequency dependent phase constituted of a pure time-delay, corroborating the results from simulations performed by Måsøy *et al.*[13]

Viola and Walker[14] investigated eight commonly used time-delay estimators used in medical ultrasound, and compared their variance to the Cramér-Rao lower bound for the same parameters as in Refs. 6 and 7. Their simulations showed that correlation methods outperformed all other methods with respect to stability (variance).

In the present article a variance analysis of estimated arrival time and amplitude fluctuations is performed in order to quantify the number of independent receive signals needed to obtain an adequate and stable estimate. As stated earlier, this information is important when using a method which is dependent upon several transmit and receive signals. In addition, transmit-beam iteration is also necessary. This is time consuming and will lower the frame rate in a real-time imaging system. High frame rate is very important for imaging of moving objects like the heart. When imaging stationary objects like the liver, a lower frame rate is acceptable.

A stable estimate can be defined as an estimate that provide some correction of the retransmitted aberration-corrected beam, compared to the aberrated beam. If iterative transmit-beam aberration correction is to be used, the first corrected transmit beam needs to provide some correction (compared to the aberrated beam) for this process to converge. If the variance is high, the initial correction could in some cases increase the aberration, making the correction scheme unstable.

The variance analysis is performed by simulating scattering of ultrasound waves from a random scattering region, uniformly distributed in space and with a Gaussian intensity distribution. Absorption or electronic noise is not included in the simulations.

II Theory

In Ref. 1 the modified beamformer output (MBFO) method was developed for estimating arrival time and amplitude fluctuations from random signals.

The MBFO estimator was developed in the frequency domain. It was based on calculating the cross-spectrum between all elements on the receiving array and a modified beamformer output, in order to determine the time-delay and amplitude of the received signal. The beam former output b of the received signal is simply defined as

$$b = \sum_{n=1}^{N} y_n \tag{5.1}$$

where y_n is the received signal on element n, and N represents the total number of elements on the array. Frequency dependence has been dropped for notational convenience.

In general, the MBFO estimation can be performed for each frequency component of the signal, thus determining the specific aberration of each frequency. In Ref. 13, it was shown that, if correctly estimated, a time-delay and amplitude for each array element produced approximately ideal aberration correction of the retransmitted beam. The MBFO algorithm was thus only implemented at the center angular frequency of the received signal, in order to determine a time-delay and amplitude in the received signal for each array element.

When calculating the MBFO, correlation information between all elements on the receiving array is used. The correlation information is weighted with the coherence of the cross-spectrum squared, a measure of the variance in the estimate of the cross-spectrum. An important issue is to obtain a reliable estimate of the cross-spectrum. This was done, as explained in the introduction, by averaging the estimated cross-spectrum from several realizations of the scattering region, that is, from several statistically independent receive signals.

The current aim is to investigate how the stability of the estimator is affected by varying the number of independent realizations.

II.A Time domain implementation of the MBFO algorithm

The MBFO algorithm is based on cross-correlation estimation. In addition, a model of the received signal is used. In Ref. 1, the received signal y was written in the frequency domain as

$$y(\mathbf{r}_a;\omega) = s(\mathbf{r}_a;\omega)\ f(\mathbf{r}_a;\omega)\ , \tag{5.2}$$

where $\mathbf{r}_a$ is the array coordinate, and $f(\mathbf{r}_a;\omega)$ represents the unaberrated receive signal. The function $f(\mathbf{r}_a;\omega)$ thus contains transmit aberration, but not receive aberration. The function $s(\mathbf{r}_a;\omega)$ is the frequency response of a filter producing distortion of the amplitude and phase of the signal as it propagates through the heterogeneous medium. This filter is denoted the *generalized frequency-dependent screen.*

In Eq. (5.2), aberration of the received signal on a specific array element, is assumed to be independent of the spatial position of the scatterer. This is a general assumption for aberration correction as it is performed at the array surface as a filter process, and is here denoted *scatterer independent aberration.* In this situation, the generalized frequency-dependent screen is denoted the *scatterer independent screen.*

In Ref. 1, a thorough discussion of the generalized frequency-dependent screen, and the basis and limitations of the receive scatterer independent aberration assumption is given.

Transforming Eq. (5.2) to the time domain yields

$$y(\mathbf{r}_a,t) = \int s(\mathbf{r}_a,t-\xi)f(\mathbf{r}_a,\xi)\mathrm{d}\xi\ , \tag{5.3}$$

where ξ is a convolution variable and the integration is taken over all time. This type of model can be solved with a blind system identification method,[15] but a different approach is chosen here.

Based on the investigations in Ref. 13 described above, the scatterer independent screen filter is modeled as a simple time-delay and amplitude screen at the array. The scatterer independent screen is then approximated as

$$s(\mathbf{r}_a, t) \approx a(\mathbf{r}_a)\delta(t - \tau(\mathbf{r}_a)) \ , \tag{5.4}$$

where $a(\mathbf{r}_a)$ is an amplitude and $\tau(\mathbf{r}_a)$ is a time-delay, both only a function of the array coordinate. This approximation introduces a loss of generality compared to the frequency implementation of the MBFO algorithm as described in Ref. 1.

Using Eq. (5.4) in (5.3) gives

$$y(\mathbf{r}_a, t) = a(\mathbf{r}_a) f(\mathbf{r}_a, t - \tau(\mathbf{r}_a)) \ . \tag{5.5}$$

It is convenient to introduce the analytic signal defined as

$$\hat{y}(\mathbf{r}_a, t) = y(\mathbf{r}_a, t) + i \ \mathrm{H}\{y(\mathbf{r}_a, t)\} \ , \tag{5.6}$$

where $\mathrm{H}\{\cdot\}$ denotes the Hilbert transform. For a band limited signal, the analytic signal can also be written as [Ref. 16 (p. AII.40)]

$$\hat{y}(\mathbf{r}_a, t) = y_e(\mathbf{r}_a, t) e^{i\omega_0 t} \ , \tag{5.7}$$

where $y_e(\mathbf{r}_a, t)$ represents the complex envelope, and ω_0 is the center angular frequency.

Introducing the narrow-band approximation,

$$\hat{y}(\mathbf{r}_a, t - \tau) \approx y_e(\mathbf{r}_a, t) e^{i\omega_0 (t-\tau)} = \hat{y}(\mathbf{r}_a, t) e^{-i\omega_0 \tau} \ , \tag{5.8}$$

a time-delay τ of the envelope is assumed to be negligible compared to the same time-delay of the carrier signal. Using this approximation in Eq. (5.5) gives

$$\hat{y}_p(t) = a_p \hat{f}_p(t - \tau_p) = a_p e^{-i\omega_0 \tau_p} \hat{f}_p(t) \equiv s_p \hat{f}_p(t) \ , \tag{5.9}$$

where the signals are written in spatial discrete form with p indicating the element number on the array. Here, s_p is the complex equivalence of the simple model of the scatterer independent screen in Eq. (5.4).

The signal model in the time domain as given by Eq. (5.9), is analogous to the frequency model in Eq. (5.2). The derivation of the estimation method in the time domain thus equals the derivation in the frequency domain as given in Ref. 1. It is briefly revised here for the purpose of continuity.

The definition of the spatial cross-correlation between signals on elements p and n is

$$R_{pn} = \mathrm{E}[\hat{y}_p \ \hat{y}_n^*] \ , \tag{5.10}$$

where $\mathrm{E}[\cdot]$ denotes an expectation operator and time-dependence has been dropped for notational convenience. Inserting Eq. (5.9) gives

$$R_{pn} = s_p s_n^* F_{pn} \ , \tag{5.11}$$

where $F_{pn} = \mathrm{E}[\hat{f}_p \ \hat{f}_n^*]$.

Solving for s_p gives

$$s_p = \frac{R_{pn}}{F_{pn}} \frac{1}{s_n^*} \equiv \frac{R_{pn}}{|F_{pn}|} \frac{1}{s_n^*} \ . \tag{5.12}$$

Now, F_{pn} can have a phase due to refraction or aberration of the transmitted beam. Assuming that $F_{pn} = |F_{pn}|$ introduces an error in the estimates as discussed in Ref. 2.

In order to use all correlation information in the signal, a weighted mean estimate of s_p is introduced as[1]

$$\tilde{s}_p = \sum_{n=1}^{N} W_{pn} \frac{R_{pn}}{|F_{pn}|} \frac{1}{\tilde{s}_n^*} \ , \tag{5.13}$$

where W_{pn} is a weight function. The average is taken over all elements N on the array.

In Ref. 1, $|F_{pn}|$ was assumed to be a known variable and was calculated using the van Cittert-Zernike theorem for an incoherent homogeneous medium. By defining the weight function W_{pn} properly, this is not necessary and $|F_{pn}|$ is here assumed to be an unknown variable.

The correlation coefficient at zero lag is defined as

$$\rho_{pn} = R_{pn} / \sqrt{R_{pp} R_{nn}}. \tag{5.14}$$

By defining W_{pn} as

$$W_{pn} = |\rho_{pn}|^2 \Big/ \sum_{n=1}^{N} |\rho_{pn}|^2 \equiv |\rho_{pn}|^2 / C_p \ , \tag{5.15}$$

the weight factor removes areas of low correlation, which contains little information of the phase and amplitude estimate. Krishnan *et al.* [17] showed that the variance of the phase estimate between to identical signals with a time shift, is inversely proportional to the magnitude of the correlation coefficient squared. A high correlation coefficient means a low variance in the phase estimate.

Taking the magnitude of the correlation coefficient and inserting the signal model from Eq. (5.9) gives

$$\begin{aligned} |\rho_{pn}| &= \frac{|R_{pn}|}{\sqrt{R_{pp} R_{nn}}} = \frac{|s_p s_n^* F_{pn}|}{\sqrt{|s_p|^2 |s_n|^2 F_{pp} F_{nn}}} \\ &= \frac{|e^{i\omega_0(\tau_n - \tau_p)} F_{pn}|}{\sqrt{F_{pp} F_{nn}}} = \frac{|F_{pn}|}{\sqrt{F_{pp} F_{nn}}} \ . \end{aligned} \tag{5.16}$$

Assuming F_{pn} to be scaled such that $F_{pp} = 1$, and inserting Eq. (5.15) and (5.16) into (5.13) gives

$$\tilde{s}_p = \frac{1}{C_p} \sum_{n=1}^{N} |\rho_{pn}| R_{pn} \frac{1}{\tilde{s}_n^*} \ . \tag{5.17}$$

By choosing the weight factor W_{pn} as in Eq. (5.15), no assumptions need be made on $|F_{pn}|$.

Using the ergodic hypothesis,[12] an unbiased estimate of the cross-correlation is defined as

$$\tilde{R}_{pn} = \frac{1}{K} \sum_k \frac{1}{T} \int_T \hat{y}_{kp}(t) \hat{y}_{kn}^*(t) \ \mathrm{d}t \ , \tag{5.18}$$

where k denotes different realizations of the received signal $\hat{y}$, and K the total number of realizations. Note that the integral part of Eq. (5.18) represents the general cross-correlation

calculated at zero lag. This is sufficient for determining a time-delay in the signal due to the introduction of the complex envelope and the narrow band approximation.

Using the estimate of the cross-correlation $\tilde{R}_{pn}$, the final expression for $\tilde{s}_p$ is

$$\tilde{s}_p = \frac{1}{C_p} \sum_{n=1}^{N} |\tilde{\rho}_{pn}| \tilde{R}_{pn} \frac{1}{\tilde{s}_n^*} \ . \tag{5.19}$$

where $\tilde{\rho}_{pn}$ is an estimate of ρ_{pn} based on $\tilde{R}_{pn}$.

Equation (5.19) is an implicit equation and is solved with an iteration scheme as outlined in Ref. 1. Zero time-delay and unity amplitude across the array is used as initial values for the iteration scheme. Estimates of arrival time and amplitude fluctuations are then calculated from $\tilde{s}_p$ as the magnitude and time-delay of the phase as defined in Eq. (5.9).

II.B Comparison of frequency and time domain implementation

Using Parseval's theorem, the integral in Eq. (5.18) gives

$$\int_{-\infty}^{\infty} \hat{y}_p(t)\hat{y}_n^*(t) \ \mathrm{d}t = \frac{1}{2\pi} \int_{-\infty}^{\infty} \hat{y}_p(\omega)\hat{y}_n^*(\omega) \ \mathrm{d}\omega \ . \tag{5.20}$$

The index k has now been dropped for notational convenience.

The Fourier transform of the analytic signal is given as [Ref. 18 (p. AII.40)]

$$\hat{y}(\omega) = 2h(\omega)y(\omega), \tag{5.21}$$

where $h(\omega)$ is a Heaviside unit step function in the frequency domain. Using Eq. (5.21) in (5.20) gives

$$\int_{-\infty}^{\infty} \hat{y}_p(t)\hat{y}_n^*(t) \ \mathrm{d}t = \frac{2}{\pi} \int_{0}^{\infty} y_p(\omega)y_n^*(\omega) \ \mathrm{d}\omega \ . \tag{5.22}$$

Writing the Fourier transform of $y(t)$ with an amplitude and phase on the form $A(\omega)e^{i\theta(\omega)}$, gives

$$\int_{-\infty}^{\infty} \hat{y}_p(t)\hat{y}_n^*(t) \ \mathrm{d}t = \frac{2}{\pi} \int_{0}^{\infty} A_p(\omega)A_n(\omega)e^{i\{\theta_p(\omega)-\theta_n(\omega)\}} \ \mathrm{d}\omega \ . \tag{5.23}$$

Equation (5.23) shows that the time domain implementation of the MBFO estimation algorithm, produce a weighted estimate of both the phase and amplitude between the signals on elements p and n over all the frequency components. This is different from the frequency domain implementation which only use the phase and amplitude at the center frequency.[1]

As in Ref. 1, by inserting Eq. (5.18) into Eq. (5.19), $\tilde{s}_p$ can be shown to satisfy the relation

$$\tilde{s}_p = \frac{1}{C_p} \frac{1}{K} \sum_{k} \frac{1}{T} \int_{T} \hat{y}_{kp}(t)\hat{b}_{kp}^*(t) \ \mathrm{d}t \ , \tag{5.24}$$

with

$$\hat{b}_{kp}(t) = \sum_{n=1}^{N} \hat{y}_{kn}(t) \ |\tilde{\rho}_{pn}| \frac{1}{\tilde{s}_n}. \tag{5.25}$$

This relation is the time domain MBFO.

By using the magnitude of the correlation coefficient as a weight term in the beamformer output, the estimation process inherently performs an efficient sub-aperture correlation process. The magnitude of the correlation coefficient is unity for $n = p$, and falls quickly in value as the distance between n and p increase. The weight function $|\rho_{pn}|$ thus performs as a sliding window (following the element p where the estimation occurs) selecting a suitable sub-aperture for the beamformer output, from a correlation perspective.

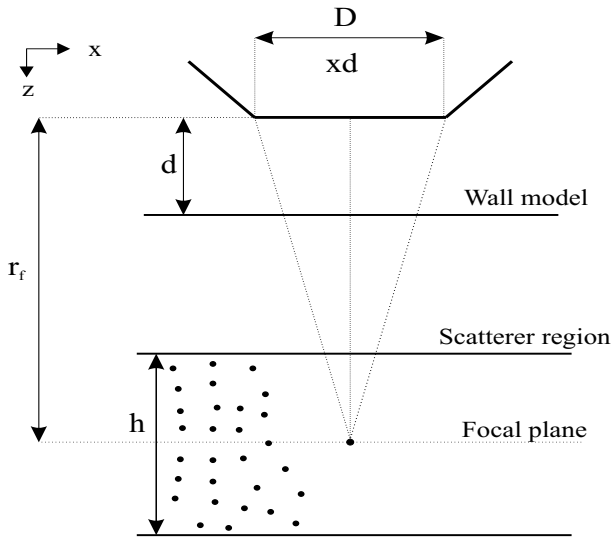

Figure 5.1: Simulation setup.

III Simulations

The same simulation setup as in Ref. 1 was used (see Fig. 5.1). An array of size D was placed onto a body wall model of thickness d. The signal was propagated with an angular spectrum operator[13] through the body wall model and to the scattering region of depth h, centered around the focal plane of the array in the range direction. Here the signal was scattered according to the Born approximation and propagated back to the array through the body wall model.

Eight body wall models, emulating the human abdominal wall, were used. Details of the body wall modelling, properties of the wall models, and a discussion of their validity can be found in Ref. 13. The names of the body wall models are the same as in Ref. 13.

For the purpose of estimating the variance of the arrival time and amplitude fluctuations estimates, 400 realizations of the scattering region was generated. The scatterers were uniformly distributed in the x and z-direction, and had a Gaussian distributed reflection strength. A simulation, as described above, was then performed for all of the scatterer realizations generating 400 statistically independent receive signals.

In order to obtain reference values for arrival time and amplitude fluctuations for both body wall models, one way point source simulations were performed. A point source was simulated in the focus $\mathbf{r}_f$ of the array. A pulse, equal to the transmit pulse from the array, was emitted from $\mathbf{r}_f$ and propagated through the body walls to the array.

III.A Simulation parameters and data processing

The simulation setup is the same as in Ref. 1 and is reiterated here for the convenience of the reader.

The simulations were implemented in MATLAB. The simulation area was 10.24 cm in the lateral direction (x-direction in Fig. 5.1) with a resolution of 0.2 mm. To avoid reflections at the edges of the spatial FFT-region (x-direction), the signal was tapered to zero over 2.54 cm at each edge with a raised cosine window. The tapering was performed for a sufficient number of

propagation steps in order to keep the noise level low.

The sampling frequency was 35.1 MHz providing a time window of 58.3 μs. The center frequency of the pulse was 2.5 MHz with a -6 dB bandwidth of 1.5 MHz. The transmitted pulse was filtered with a 50% fractional bandwidth bandpass filter, centered around the center frequency of the pulse. An array aperture size of 20 mm with point-like elements was chosen. The focal depth $\mathbf{r}_f$ of the array was 60 mm. The thickness of the body walls was 20 mm. The medium through which the signals were propagated had a speed of sound equal to that of water (1523 m/s).

The scattering area had a range depth h of 30.5 mm (time window of 20 μs), 15.25 mm to each side of the focal plane (see Fig. 5.1). This range was chosen to be well inside the -3 dB focal depth of the array.[1] The scatterer density was approximately 1600 scatterers per square centimeter.

Geometric focusing was removed from all received signals prior to processing of results.

For the time domain implementation, the cross-correlation was calculated according to Eq. (5.18). Trapezoid integration was used to calculate the integral.

The cross-spectrum for an element p was estimated by averaging the spectrum from overlapping segments of the signal (Welch's method). The element signal was separated into 64 segments (0.9 μs) with 50% overlap. Each segment was weighted with a Hanning window before calculation of the FFT.

A wavefront tracking method[13] was used to estimate arrival time fluctuations of the wavefront from the point source simulations. This method proved to give accurate description of the time-delay variation of the received wavefront. Arrival amplitude fluctuations for each array element from the point source simulations were calculated as the arithmetic mean of the magnitude of the frequency spectrum over a band of frequencies ranging from 2-3 MHz. This band was chosen empirically.

Beam profiles in the focal plane of the array were calculated as the rms value in time of each spatial position. These profiles were used for the visual evaluation of the effect of the different aberration correction filters.

To analyze the variance of estimated arrival time and amplitude fluctuations, the standard deviation σ of the estimate for an array element p was calculated as

$$\sigma_p = \sqrt{\frac{1}{M-1}\sum_{m=1}^{M}(x_{mp} - \bar{x}_p)^2} \ , \tag{5.26}$$

where x denotes either an arrival time or amplitude fluctuation estimate, $\bar{x}$ is the mean value of the estimate, and M is total number of estimates used for calculating the standard deviation. In all the simulations, twenty estimates ($M = 20$) were used to calculate the mean and standard deviation. Thus when the number of independent measurements K varied, M remained constant equal to twenty. The simulations were carried out for $K = \{1, 3, 5, 10, 15, 20\}$.

In addition, the average value of the standard deviation (average standard deviation) across the array was also calculated. This is defined as

$$\bar{\sigma} = \frac{1}{N}\sum_{p=1}^{N}\sigma_p \ , \tag{5.27}$$

where N is the total number of array elements.

To evaluate the mean value of obtained estimates, as a function of the number of independent measurements used to obtain an estimate, the normalized L^2 difference between this value and the reference was calculated.[2]

IV Results

For estimates of arrival time and amplitude fluctuations, and beam profiles, only selected data for the w6 and s6 aberrator are presented for $K = 1$ and $K = 3$. These data are representative for all aberrators in the simulation study.

Average standard deviation curves, as a function of the number of independent receive signals (K) used for estimation, are presented for all aberrators.

In all the figures presented here, t-domain denotes the time domain implementation and f-domain represents the frequency domain implementation.

Figure 5.2 shows mean arrival time fluctuation estimates with standard deviation for the w6 and s6 aberrators. The curves are plotted both for the time and frequency domain implementation of the MBFO algorithm. The mean value of estimates in the time and frequency domain are quite similar for both aberrators. There is clearly a higher standard deviation for the s6 aberrator compared to w6. The standard deviation is reduced when the number of independent signals is increased from $K = 1$ to $K = 3$. There is also a minor improvement in the mean estimate compared to the reference when K is increased. There are very small differences in the standard deviation between the time and frequency implementation.

Mean arrival amplitude fluctuation estimates with standard deviation are shown in Fig. 5.3. Here the standard deviation also decrease when K increase, but this does not seem to improve the mean value of the estimates. The mean estimate is poor compared to the reference. The above comments are valid for all aberrators investigated here. Here also, there are marginal differences between the time and frequency domain implementation.

Figure 5.4 shows the mean value of aberration corrected beam profiles, with standard deviation, in the focal plane of the array. As for the arrival time fluctuation estimates, there is some improvement in the corrected beam profiles for the w6 aberrator when K is increased. This is mainly due to the small improvement in the mean value of the arrival time fluctuation estimates. There are also minor improvements for the s6 aberrator. Note that for the s6 aberrator and $K = 1$, the side-lobe level of the standard deviation curve is higher than the uncorrected beam in some parts of the profile.

In Fig. 5.5 the normalized L^2 difference between the mean estimate and the reference is presented. The figure shows that for the arrival time fluctuations, there is a small improvement in the mean estimate when K is increased from 1 to 3, and then the difference stabilizes. For the amplitude fluctuations, this improvement is less visible. For the other aberrators, such an improvement was not observed, and the L^2 difference remained approximately constant as a function of K.

Figure 5.6 presents the average standard deviation as a function of the number of independent signals for the w6 and s6 aberrators. The results for both arrival time and amplitude fluctuation estimates are given. The average standard deviation for amplitude estimates is normalized with the mean value of the amplitude estimate for the point source reference. For the arrival time fluctuation estimates, the difference in average standard deviation between the w6 and s6 aberrator is approximately a factor two. For both aberrators, there is little difference between the time and frequency implementation. In the case of arrival amplitude fluctuation estimates, there is also a substantial difference in average standard deviation between the aberrators. There is almost no difference between the implementations. In general (and as expected) for both arrival time and amplitude fluctuation estimates, the average standard deviation decreases with increasing K.

Figures 5.7 and 5.8 presents the average standard deviation for the rest of the aberrators. These are only been presented for $K = \{1, 3, 5\}$, since this is where the major changes occur. The general trend is that the average standard deviation decreases with increasing K, and that there

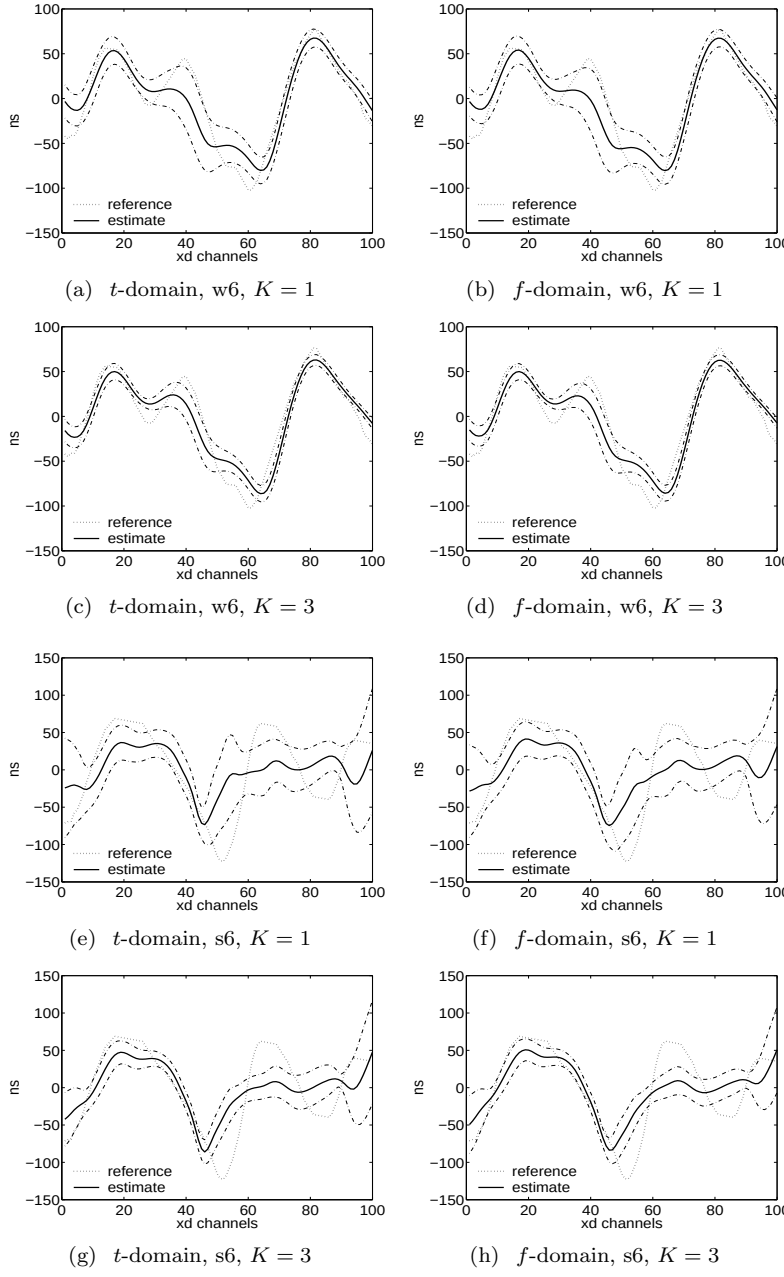

(a) t-domain, w6, $K = 1$ (b) f-domain, w6, $K = 1$

(c) t-domain, w6, $K = 3$ (d) f-domain, w6, $K = 3$

(e) t-domain, s6, $K = 1$ (f) f-domain, s6, $K = 1$

(g) t-domain, s6, $K = 3$ (h) f-domain, s6, $K = 3$

Figure 5.2: Mean arrival time-delay fluctuation estimates with standard deviation for the w6 and s6 aberrators. Here, K measurements per estimate are used. The reference curve denotes the arrival time fluctuations estimate from the point source. The solid line is the mean value of the estimate, and the dashed-dotted line shows the standard deviation of the estimates.

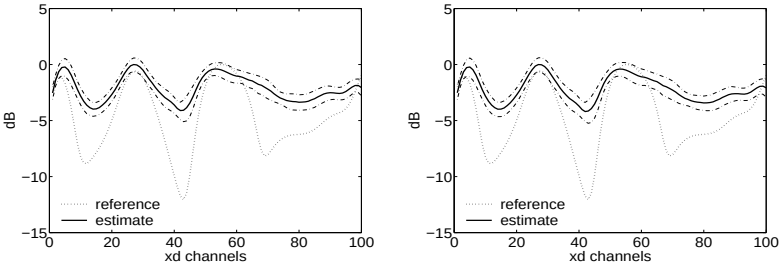

(a) t-domain, w6, $K = 1$

(b) f-domain, w6, $K = 1$

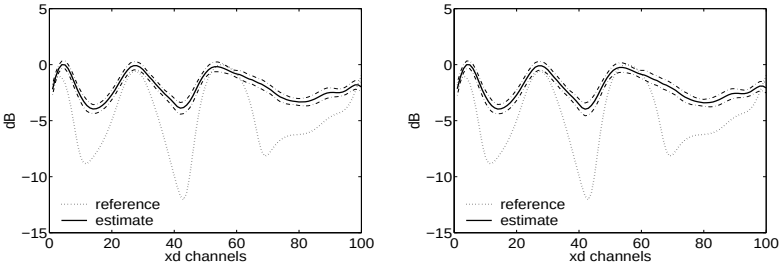

(c) t-domain, w6, $K = 3$

(d) f-domain, w6, $K = 3$

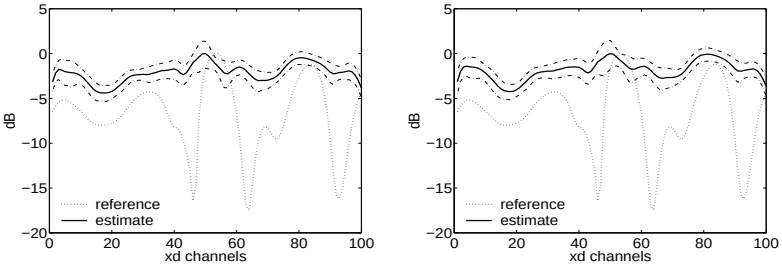

(e) t-domain, s6, $K = 1$

(f) f-domain, s6, $K = 1$

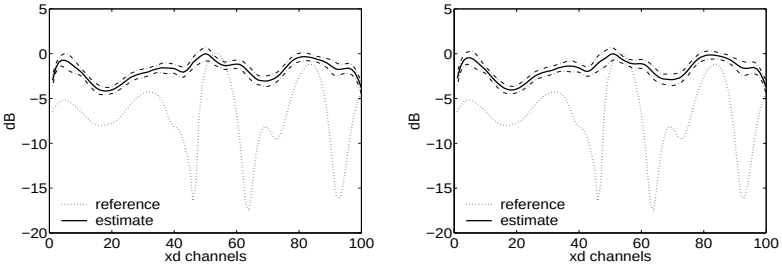

(g) t-domain, s6, $K = 3$

(h) f-domain, s6, $K = 3$

Figure 5.3: Mean arrival amplitude fluctuation estimates with standard deviation for the w6 and s6 aberrators. Same notation as in Fig. 5.2.

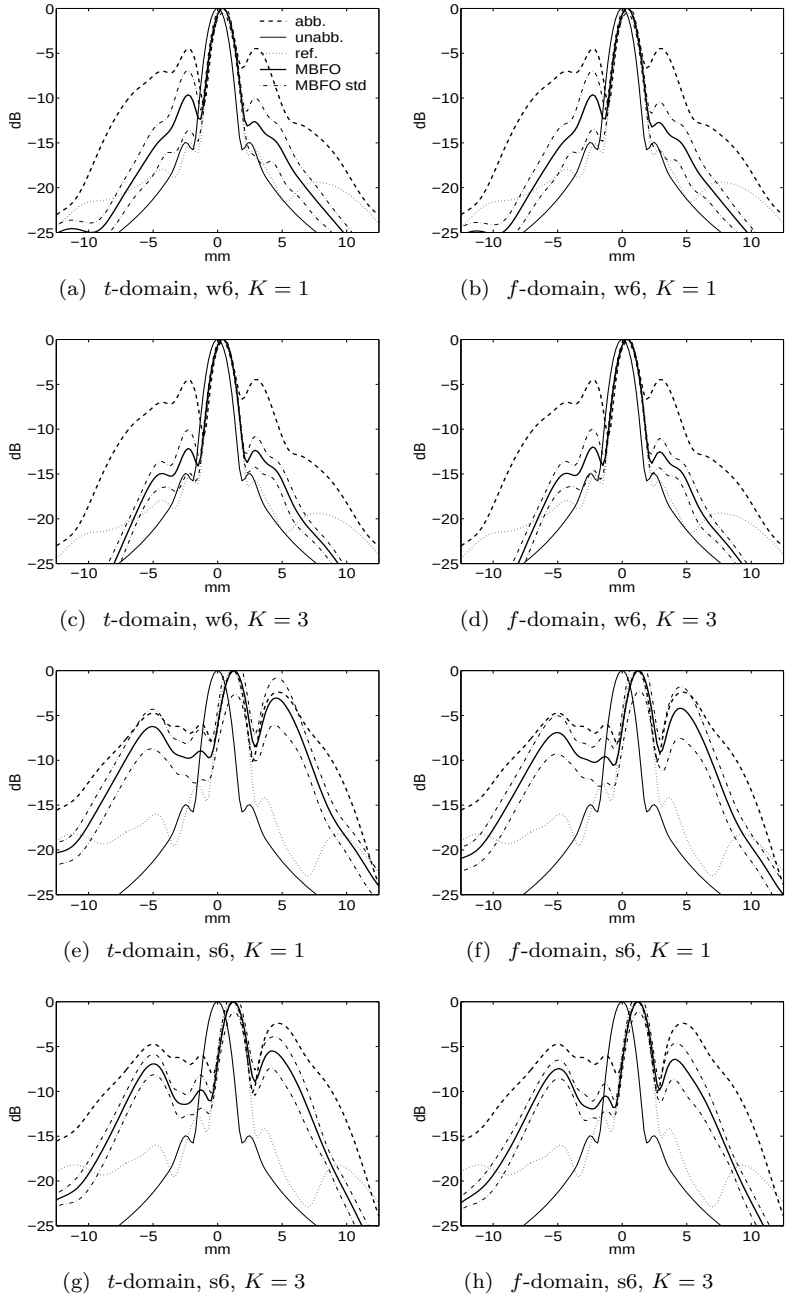

(a) t-domain, w6, $K = 1$

(b) f-domain, w6, $K = 1$

(c) t-domain, w6, $K = 3$

(d) f-domain, w6, $K = 3$

(e) t-domain, s6, $K = 1$

(f) f-domain, s6, $K = 1$

(g) t-domain, s6, $K = 3$

(h) f-domain, s6, $K = 3$

Figure 5.4: Mean value of beam profiles in the focal plane of the array, with standard deviation, for the w6 and s6 aberrators. The vertical axis displays energy in decibels, and the horizontal axis displays the focal plane in millimeters. The curve *abb.* denotes the uncorrected transmit-beam, *unabb.* denotes the unaberrated transmit-beam, *ref.* is the transmit-beam corrected with the point source reference, *MBFO* shows the mean value of the beam profiles corrected with the MBFO estimator, and the dashed-dotted line *MBFO std* represents the standard deviation. The legend is the same for all figures as for figure (a).

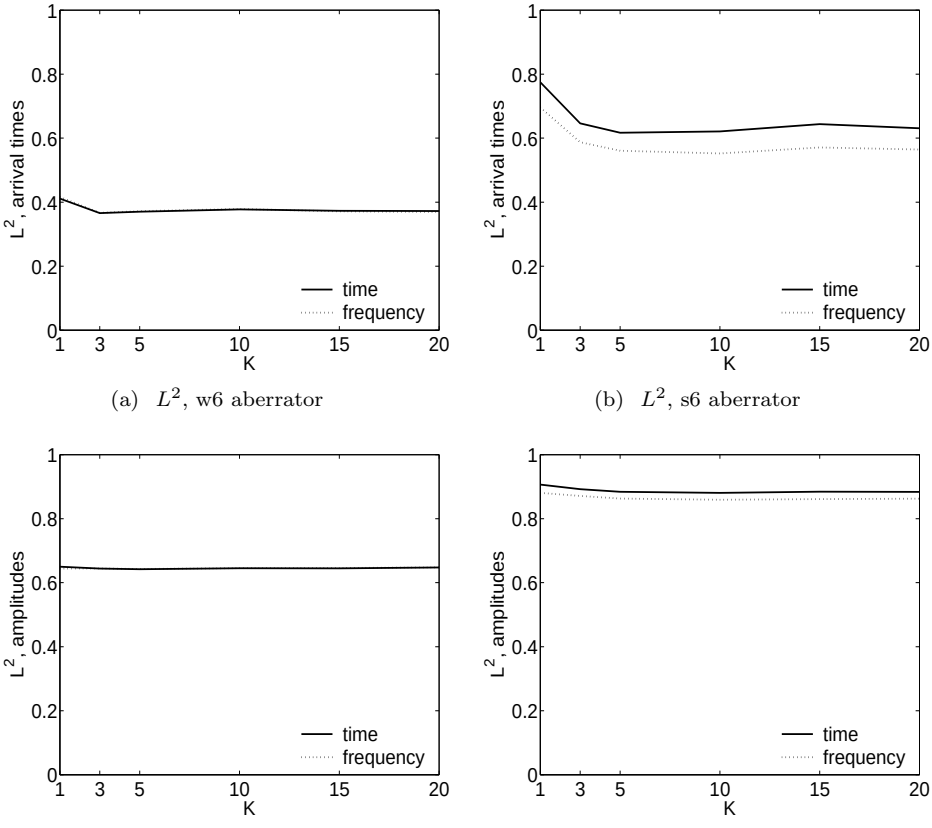

(a) L^2, w6 aberrator (b) L^2, s6 aberrator

(c) L^2, w6 aberrator (d) L^2, s6 aberrator

Figure 5.5: Normalized L^2 difference between mean value of estimated arrival time and amplitude fluctuations, and the point source reference. The L^2 difference is plotted as a function of K for the time and frequency domain implementation. The top row displays the difference for arrival times, and the bottom row for amplitudes.

exists only smaller differences between the two implementations. For the s8 aberrator, there are some differences visible for the arrival time fluctuation estimates.

V Discussion

As seen from the results in the previous section, there are only small differences between the time and frequency domain implementation. In general, the mean value and standard deviation of arrival times and amplitude fluctuations are approximately equal for all investigated aberrators.

As expected, the average value of the standard deviation across the array is reduced when increasing the number of independent measurements K. Increasing this number from $K = 1$ to $K = 3$, reduced the average standard deviation of arrival time fluctuation estimates by $42.1 \pm 3.8\,\%$ for the time domain implementation, and for all aberrators. For the amplitude estimates the reduction is $39.1 \pm 3.7\,\%$. The reduction from $K = 3$ to $K = 5$ is approximately $20\,\%$ for both arrival time and amplitude fluctuation estimates. This very closely matches a

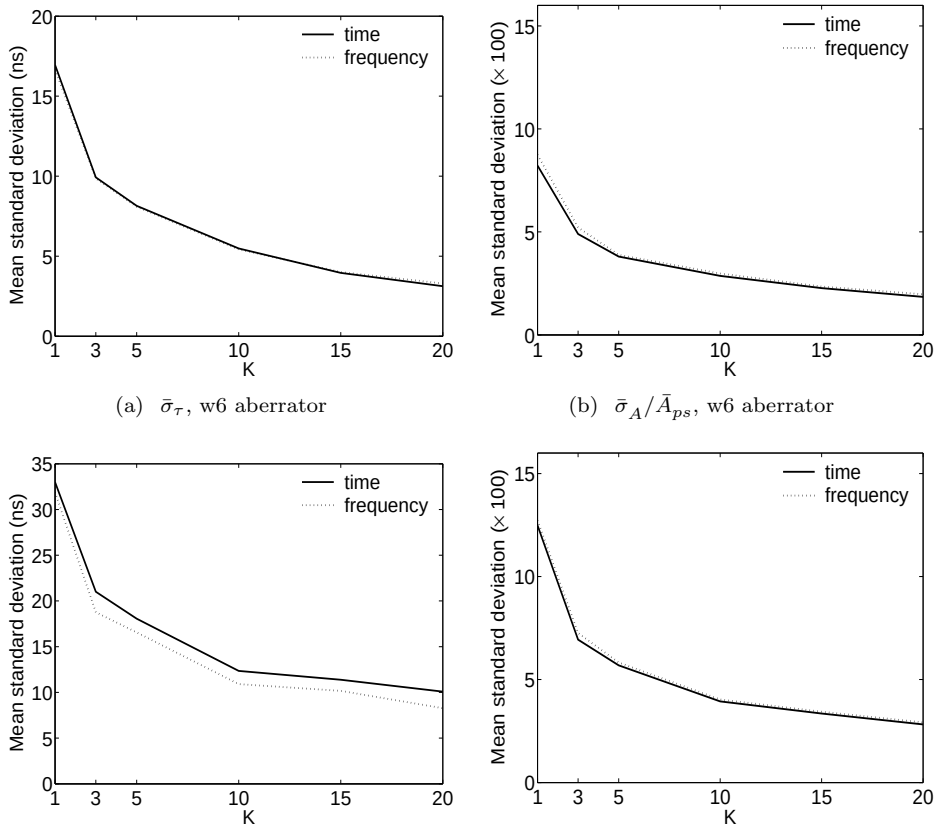

(a) $\bar{\sigma}_\tau$, w6 aberrator

(b) $\bar{\sigma}_A/\bar{A}_{ps}$, w6 aberrator

(c) $\bar{\sigma}_\tau$, s6 aberrator

(d) $\bar{\sigma}_A/\bar{A}_{ps}$, s6 aberrator

Figure 5.6: Average standard deviation for arrival time ($\bar{\sigma}_\tau$) and amplitude ($\bar{\sigma}_A/\bar{A}_{ps}$) fluctuations as a function of the number of independent measurements (K) used in the estimation for the w6 and s6 aberrator. The average standard deviation for the amplitude is normalized with the mean value of the amplitude estimate ($\bar{A}_{ps}$) from the point source simulation.

$1/\sqrt{K}$ reduction, which is 42.3 % for K increasing from 1 to 3, and 22.5 % for 3 to 5.

There is a small improvement in the L^2 difference between the mean arrival time fluctuation estimate, and the point source reference for the w6 and s6 aberrators as K was increased from 1 to 3. For $K > 3$, no change was observed. This shows that sufficient averaging of the estimates was performed for $K = 1$.

An important point is that the standard deviation varies quite strongly between the aberrators. For $K = 1$, using the time domain implementation, the variation in average standard deviation for arrival time fluctuations between the eight investigated aberrators ranged from approximately 8-43 ns. For amplitude fluctuations, there is a 42 % difference between the maximum and minimum average standard deviation. These results show that the stability of the estimation is highly dependent on the aberration. The aberration corrected beam profile for each estimate was therefore investigated for all aberrators. The general trend showed that all estimates produced an improvement of the corrected beam profile. This result was independent of K.

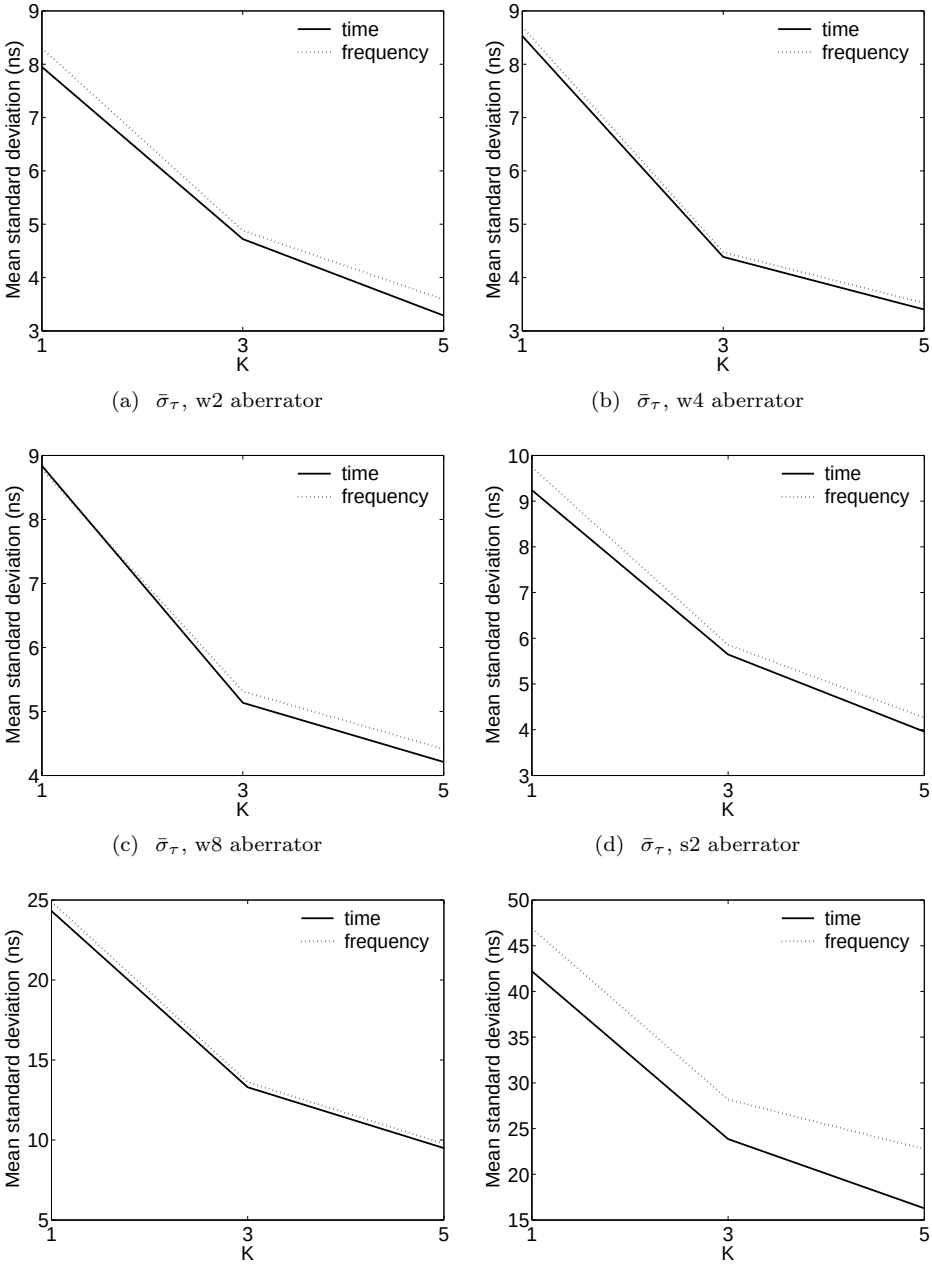

(a) $\bar{\sigma}_\tau$, w2 aberrator

(b) $\bar{\sigma}_\tau$, w4 aberrator

(c) $\bar{\sigma}_\tau$, w8 aberrator

(d) $\bar{\sigma}_\tau$, s2 aberrator

(e) $\bar{\sigma}_\tau$, s4 aberrator

(f) $\bar{\sigma}_\tau$, s8 aberrator

Figure 5.7: Average standard deviation ($\bar{\sigma}_\tau$) for arrival time fluctuations as a function of the number of independent measurements (K) used in the estimation for the w2, w4, w8, s2, s4, and s8 aberrator.

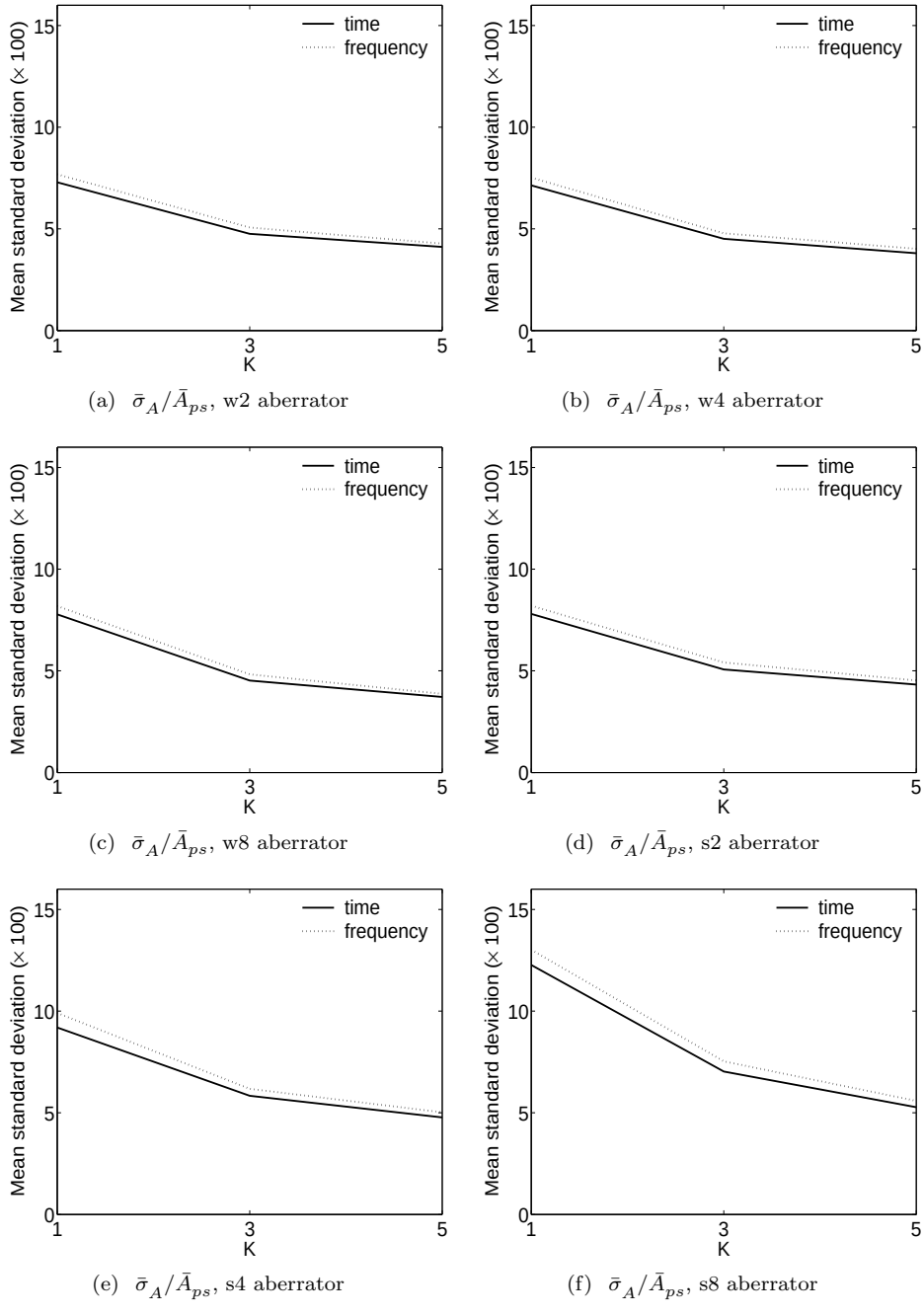

(a) $\bar{\sigma}_A/\bar{A}_{ps}$, w2 aberrator

(b) $\bar{\sigma}_A/\bar{A}_{ps}$, w4 aberrator

(c) $\bar{\sigma}_A/\bar{A}_{ps}$, w8 aberrator

(d) $\bar{\sigma}_A/\bar{A}_{ps}$, s2 aberrator

(e) $\bar{\sigma}_A/\bar{A}_{ps}$, s4 aberrator

(f) $\bar{\sigma}_A/\bar{A}_{ps}$, s8 aberrator

Figure 5.8: Average standard deviation ($\bar{\sigma}_A/\bar{A}_{ps}$) for amplitude estimates as a function of the number of independent measurements (K) used in the estimation for the w2, w4, w8, s2, s4, and s8 aberrator. The average standard deviation is normalized with the mean value of the amplitude estimate ($\bar{A}_{ps}$) from the point source simulation.

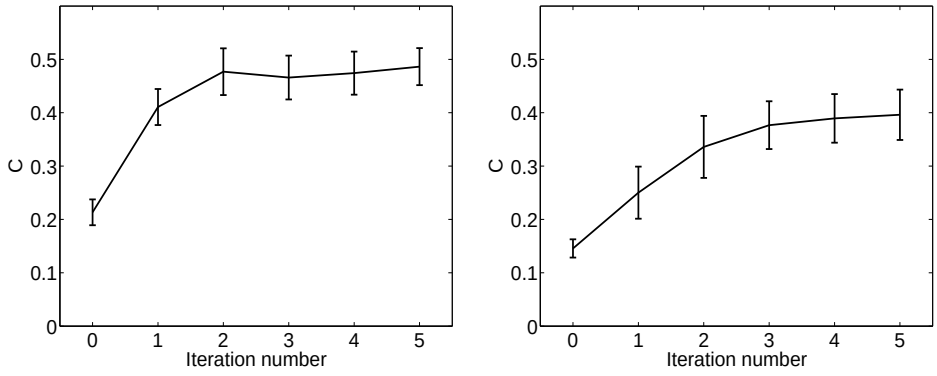

(a) C parameter, w6 aberrator (b) C parameter, s6 aberrator

Figure 5.9: Mean value of the focus quality parameter C as a function of iteration number, using the time domain implementation with $K = 1$. The solid line represents the mean value of C for the twenty different estimates of arrival time fluctuations. The error bars are standard deviation.

For the s6 aberrator, using $K = 1$, many of the estimates yielded very little correction of the beam profile. This is clearly demonstrated by the standard deviation of the beam profiles in Fig. 5.4 (e) and (f). If the transmit-beam is not sufficiently corrected, an iterative transmit-beam aberration correction process may not converge, and such a process was investigated for the w6 and s6 aberrator for $K = 1$. The simulations were only carried out for the time domain implementation since there exists only minor differences between the two. Note that a new independent realization of the scattering region was generated for each iteration. In Ref. 2, it was shown that using the frequency domain implementation and $K = 20$, the transmit-beam iteration process converged to properly corrected focus beam profile for both these aberrators.

The quality, and convergence, of the correction was quantified by the focus quality parameter C introduced by Mallart and Fink.[19] This parameter has proven to be suitable for this purpose.[2] The mean value of C for the twenty different estimates, with standard deviation, is plotted as a function of iteration number in Fig. 5.9. Iteration number 0 refers to the initial uncorrected transmit beam. The figure shows that for the w6, convergence is obtained after two iterations. This is the same result obtained in Ref. 2 using $K = 20$. For the s6 aberrator, the process converged after three iterations, which is the same result as obtained in Ref. 2 using $K = 20$. The results suggest that only minor improvements of the first corrected beam profile is necessary for a transmit-beam iteration process to converge rapidly with good quality. Also, the results indicate that using one receive signal is sufficient.

For the frequency domain implementation, a Welch method with 50 % overlap of segments was used to estimate the cross-spectrum. Each segment was windowed with a Hanning window. The number of segments used was 64, which corresponds to a segment kernel length of 0.9 μs. The transmit signal was a 2.5 period pulse with 2.5 MHz center frequency, which gives a pulse length of 1 μs. The kernel length of each segment then corresponds to approximately 2.25λ, where λ represents the wavelength. This is a relatively small kernel length. In Ref. 14, the Cramér-Rao lower bound of a neighbor correlation estimation method was investigated as a function of different parameters. A small kernel length produced a relatively high lower bound on the standard deviation. In order to investigate the dependency of the estimates on the kernel length of the segment, additional simulations were carried out using 32 and 16 segments. This corresponds to 4.5λ and 9λ respectively. For the s6 aberrator and $K = 1$, increasing the segment length from

2.25λ to 4.5λ produced minor improvements in the mean value of both arrival time and amplitude fluctuations. The average standard deviation, on the other hand, was increased by 31 % for the arrival time fluctuations and 14 % for amplitude fluctuations. Examining aberration corrected beam profiles, showed a marginal improvement of the mean value of the profiles. The standard deviation increased, yielding an overall poorer result. For the w6 aberrator there were minor changes in the mean value of the estimates. The average standard deviation increased by 4 % for arrival time fluctuations, and 17 % for amplitudes. Since estimates of amplitude fluctuations are poor, the increased kernel length had no visible effect on the corrected beam profiles. Using 9λ increased the same results by 53 % and 56 % for the s6 aberrator, and 48 % and 46 % for the w6 aberrator. The MBFO algorithm averages the correlation between several elements selected by the correlation coefficient or the coherence function. Averaging the correlation over a number of coherent elements reduces the variance in the estimate. The results presented here then shows that a smaller kernel length is tolerated, and is preferable, due to the total reduction of variance in the estimates.

The cross-correlation in the time domain [Eq. (5.18)] proved to yield an average of the cross-spectrum over all frequency components. For the frequency implementation, arrival times and amplitude fluctuations were estimated at the center frequency of the signal.[1] With a narrow band signal, and a linearly varying phase with frequency, the obtained estimates with the time domain implementation should yield approximately the same result. In Ref. 13, it was shown that using a time-delay and amplitude aberration correction filter estimated from a point source, produced close to ideal aberration correction for the w6 and s6 aberrator. This is also true for the rest of the aberrators. Therefore, the phase of the aberration is adequately modeled with a pure time-delay for the presented results, and both implementations produced the same results. If the phase of the aberration [as described by the generalized frequency-dependent screen in Eq. (5.2)] varies non-linearly with frequency, the two implementations may produce different results due to the averaging process.

The difference in computational cost between the time and frequency implementation, may be explored by identifying the number of complex multiplications necessary to calculate an estimate. The iterative solution scheme used to solve the MBFO equations, is assumed to converge equally fast for both implementations. Assume further an element signal with P time samples. By dividing the signal into L segments, each of length J, the Welch method with 50 % overlap gives

$$2L\,\frac{J}{2}\log_2(J) = P\log_2(J) \tag{5.28}$$

number of complex multiplications for one element signal. Here, $L = P/J$, $2L$ is the number of Fourier transforms, and $J/2\log_2(J)$ is the number of complex multiplications in an FFT of length J (assuming the radix-2 FFT algorithm). In addition to the $2L$ number of Fourier transforms, there are $J\ 2L = 2P$ additional multiplications required for windowing the data. The MBFO algorithm then calculates the correlation between each element signal and a modified beam former output for a single frequency component. Assuming the number of independent realizations $K = 1$, this gives one additional complex multiplication for each element on the array. The total number of multiplications for the frequency implementation is then

$$N[2P + P\log_2(J)]\ , \tag{5.29}$$

where N is the total number of elements on the array.

In the time domain, the analytic signal is used and a Hilbert transform is required. Such a transform can be approximated with a $\pi/2$ phase shift of the time signal, and may in hardware be implemented by a simple time shift. As seen in Eq. (5.24), the time domain implementation of the MBFO algorithm calculates an auto-correlation of the element signal and the modified

beamformer output. This gives P complex multiplications per element and NP in total for the whole array. The relative difference between the frequency and time implementation is thus given as

$$2 + \log_2(J) \ . \tag{5.30}$$

The difference is only determined by the segment length used in the Welch averaging method. As an example, in the presented simulations the segment length was 32 time samples, which means that using the time domain implementation reduces the number of complex multiplications by a factor of 7. If a transmit-beam iteration process is required, the computational savings are multiplied with the number of iterations necessary for convergence.

The simulations presented here were performed using scatterers with a spatial uniform distribution. Averaging over a sufficient number of independent scatterer realizations (receive signals), produce a totally incoherent medium. This will not be the case in practical ultrasound imaging. Here, tissue structures of different size are present in the receive signal which introduce regions (of varying size) with high spatial correlation. This may render the correlation estimation less efficient than for uniform scatterers. To study this is beyond the scope of this article.

As shown by Rigby *et al.*,[4] image artifacts due to strong off-axis scatterers may be a problem in a transmit-beam iteration procedure. A strong off-axis scatterer can dominate the receive signal and affect the estimation of arrival time and amplitude fluctuations. The result is that the corrected retransmitted beam "locks" on to the strong scatterers, producing image artifacts. For the purpose of the analysis presented in this article, such cases were not studied.

VI Conclusions

In this article the MBFO algorithm,[1] previously developed in the frequency domain, is implemented in the time domain. The MBFO method use an average of cross-spectrum components (frequency domain), or cross-correlations (time domain) between neighboring elements. The number of neighbor elements used in the averaging process is determined by the spatial coherence function in the frequency domain, and the cross-correlation coefficient in the time domain.

The time domain implementation introduce a loss of generality. In the frequency domain, individual frequency dependent amplitude and phase correction could be performed on each frequency component in the signal. In the time domain implementation presented here, only a simple time-delay and amplitude correction (independent of frequency) is possible. On the other hand, the time domain implementation reduce the computational cost of estimation. This is important for fast implementations.

In order to improve the cross-spectrum or cross-correlation estimates, a method of averaging the correlation over independent receive signals was proposed in Ref. 1. The number K of independent signals used in the averaging process, affects the stability of arrival time and amplitude fluctuation estimates. How this stability varied for $K = \{1, 3, 5, 10, 15, 20\}$ was investigated for eight different aberrators, emulating the human abdominal wall.

The results show that the time and frequency domain implementation of the MBFO algorithm yields close to equal estimates of arrival time and amplitude fluctuations, independent of K. The standard deviation of these estimates is approximately the same for both implementations. Increasing K reduce the standard deviation with approximately $1/\sqrt{K}$.

There is a strong variation in standard deviation between the different investigated aberrators. Still, aberration corrected beam profiles are improved for all aberrators and all K.

Iterative transmit-beam aberration correction converged using just one receive signal for the w6 and s6 aberrators. The convergence rate, and quality, was approximately equal compared to

using 20 independent signals for averaging the correlation process.

Acknowledgments

The work presented in this article was supported by the Medicine and Health program of the Research Council of Norway.

References

[1] S.-E. Måsøy, T. Varslot, and B. Angelsen, "Estimation of ultrasound wave aberration with signals from random scatterers," *J. Acoust. Soc. Am.*, vol. 115, no. 6, pp. 2998–3009, June 2004.

[2] S.-E. Måsøy and T. Varslot and B. Angelsen, "Iteration of transmit-beam aberration correction in medical ultrasound imaging," 2004, accepted for publication in JASA.

[3] M. Karaman, A. Atalar, H. Köymen, and M. O'Donnell, "A phase aberration correction method for ultrasound imaging," *IEEE Trans. Ultrason. Ferroelectr. Freq. Control*, vol. 40, no. 4, pp. 275–282, July 1993.

[4] K. W. Rigby, C. L. Chalek, B. H. Haider, R. S. Lewandowski, M. O'Donnell, L. S. Smith, and D. G. Wildes, "Improved in vivo abdominal image quality using real-time estimation and correction of wavefront arrival time errors," *IEEE Ultrasonics Symposium*, vol. 2, pp. 1645–1653, October 2000.

[5] T. Varslot, B. Angelsen, and R. C. Waag, "Spectral estimation for characterization of acoustic aberration," *J. Acoust. Soc. Am.*, vol. 116, no. 1, pp. 97–108, July 2004.

[6] W. F. Walker and G. E. Trahey, "A fundamental limit on the performance of correlation based phase correction and flow estimation techniques," *IEEE Trans. Ultrason. Ferroelectr. Freq. Control*, vol. 41, no. 5, pp. 644–654, September 1994.

[7] W. F. Walker and G. E. Trahey, "A fundamental limit on delay estimation using partially correlated speckle signals," *IEEE Trans. Ultrason. Ferroelectr. Freq. Control*, vol. 42, no. 2, pp. 301–308, March 1995.

[8] G. C. Ng, S. S. Worrel, P. D. Freiburger, and G. E. Trahey, "A comparative evaluation of several algorithms for phase aberration correction," *IEEE Trans. Ultrason. Ferroelectr. Freq. Control*, vol. 41, no. 5, pp. 631–643, September 1994.

[9] S. W. Flax and M. O'Donnell, "Phase-aberration correction using signals from point reflectors and diffuse scatterers: Basic principles," *IEEE Trans. Ultrason. Ferroelectr. Freq. Control*, vol. 35, no. 6, pp. 758–767, November 1988.

[10] J. C. Lacefield and R. C. Waag, "Spatial coherence analysis applied to aberration correction using a two-dimensional array system," *J. Acoust. Soc. Am.*, vol. 112, no. 6, pp. 2558–2566, December 2002.

[11] G. C. Carter, "Coherence and time delay estimation," *Proc. IEEE*, vol. 75, no. 2, pp. 236–255, 1987.

[12] M. B. Priestley, *Spectral Analysis and Time Series.* Academic Press, 1988.

[13] S.-E. Måsøy, T. F. Johansen, and B. Angelsen, "Correction of ultrasonic wave aberration with a time delay and amplitude filter," *J. Acoust. Soc. Am.*, vol. 113, no. 4, pp. 2009–2020, April 2003.

[14] F. Viola and W. F. Walker, "A comparison of the performance of time-delay estimators in medical ultrasound," *IEEE Trans. Ultrason. Ferroelectr. Freq. Control*, vol. 50, no. 4, pp. 392–401, April 2003.

[15] F. Lin and R. C. Waag, "Estimation and compensation of ultrasonic wavefront distortion using a blind system identification method," *IEEE Trans. Ultrason. Ferroelectr. Freq. Control*, vol. 49, no. 6, pp. 739–755, June 2002.

[16] B. Angelsen, *Ultrasound imaging. Waves, signals and signal processing.* Trondheim: Emantec, 2000, vol. II, http://www.ultrasoundbook.com.

[17] S. Krishnan, K. W. Rigby, and M. O'Donnell, "Improved estimation of phase aberration profiles," *IEEE Trans. Ultrason. Ferroelectr. Freq. Control*, vol. 44, no. 3, pp. 701–713, May 1997.

[18] B. Angelsen, *Ultrasound imaging. Waves, signals and signal processing.* Trondheim: Emantec, 2000, vol. I, http://www.ultrasoundbook.com.

[19] R. Mallart and M. Fink, "Adaptive focusing in scattering media through sound-speed inhomogeneities: The van Cittert Zernike approach and focusing criterion," *J. Acoust. Soc. Am.*, vol. 96, no. 6, pp. 3721–3732, December 1994.

Appendix A

Aberration as a function of frequency

Very little is known about the frequency dependence of aberration. But since aberration is an interference phenomenon, which is inherently frequency dependent, physical reasoning suggests that aberration also is frequency dependent.

In this thesis, the heterogeneous Green's function has been modelled as

$$g(\mathbf{r}, \mathbf{r}_s; \omega) = s(\mathbf{r}, \mathbf{r}_s; \omega)\ g_h(\mathbf{r} - \mathbf{r}_s; \omega)\ , \tag{A.1}$$

where $\mathbf{r}$ is a field-coordinate and $\mathbf{r}_s$ represents a source coordinate. The generalized frequency dependent screen $s(\mathbf{r}, \mathbf{r}_s; \omega)$ is expressed as

$$s(\mathbf{r}, \mathbf{r}_s; \omega) = a(\mathbf{r}, \mathbf{r}_s; \omega)\ e^{i\theta(\mathbf{r}, \mathbf{r}_s; \omega)}\ . \tag{A.2}$$

The representation of aberration through the generalized screen, incorporates a frequency dependent aberration amplitude and phase. In Chapter 2 it was shown that aberration correction, using the complex conjugate of the frequency dependent screen as a correction filter, gave very close to ideal aberration correction. It was also shown that a simple time-delay and amplitude filter, independent of frequency, gave approximately equal correction even when strong waveform deformation was observed in the received signal. Based on these results, the investigations in Chapter 3 and 4 was performed with a time-delay and amplitude filter.

In the frequency domain implementation of the MBFO algorithm, the receive signal is written as

$$y(\mathbf{r}_a; \omega) = s(\mathbf{r}_a; \omega)\ f(\mathbf{r}_a; \omega)\ , \tag{A.3}$$

where $\mathbf{r}_a$ represents the array coordinate. Here, the generalized frequency dependent screen is approximated with the scatterer independent screen, given as

$$s(\mathbf{r}_a; \omega) = a(\mathbf{r}_a; \omega)\ e^{i\theta(\mathbf{r}_a; \omega)}\ . \tag{A.4}$$

Now, a pure time-delay as a function of the array coordinate is expressed in the frequency domain as $e^{-i\omega\tau(\mathbf{r}_a)}$, where τ is a time-delay. The phase of the screen, for a specific array coordinate, may be written as an L-order orthogonal basis on the form

$$\theta(\omega) = \sum_{l}^{L} \tau_l \phi_l(\omega) \tag{A.5}$$

Table A.1: The parameter β as a function of center frequency f_0 for τ =100 ns.

f_0	1.25 MHz	2.5 MHz	5.0 MHz	7.5 MHz	10.0 MHz	12.5 MHz
β	0.125	0.25	0.5	0.75	1	1.25

where τ_l represents the coefficients of the basis functions $\phi_l(\omega)$.

The results from Chapter 2 and from Ref. 1 indicate that the higher order coefficients in the basis representation of the phase θ are small, and contribute little to the aberration correction of the signal. For both of these studies, the center frequency of the signal has been relatively low (2.5 MHz and 3.0 MHz), and the question is how the magnitude of the higher order coefficients change with increasing center frequency.

A simple exercise can be performed to illustrate this. Let

$$y_1(t) \tag{A.6}$$

$$y_2(t) = \alpha \; y_1(t - \tau) \; , \tag{A.7}$$

represent two typical ultrasound pulse signals as a function of time. Here, α is a scaling amplitude factor and τ is a time-delay, that is, y_2 is a scaled and time-delayed version of y_1.

Now, the period of the pulse is given as

$$T = 1/f_0 \; , \tag{A.8}$$

where f_0 is the center frequency. Let

$$\tau = \beta \; T \; , \tag{A.9}$$

where β is a scaling factor of the period. Then

$$\beta = \frac{\tau}{T} = \tau f_0 \; . \tag{A.10}$$

For a given time-delay τ, the value of β will increase with increasing center frequency of the pulse. That is, as the frequency increases the two signals are shifted a larger and larger portion of the period.

Assume $y(t) = y_1(t) + y_2(t)$. This constitutes the simplest form of interference and the task is to investigate the phase of $y(t)$ as a function of frequency for a specific τ.

Using reported values of arrival time fluctuations for the abdominal wall,[2] a typical time-delay difference at the array in ultrasound aberration could be in the order of 100 ns (average time-delay difference at the array in Ref. 2 is 131.5 ns). Table A.1 shows β as a function of center frequency for typical ultrasound frequencies, and for τ =100 ns.

The table shows that *e.g.* at 7.5 MHz, y_2 is shifted three quarters of a period from y_1. This constitutes a rather dramatic shift, and will have a drastic consequence for the phase of y.

Frequencies ranging from 7.5 to 12.5 MHz are typical frequencies for female breast imaging. The breast is highly heterogeneous giving time-delay differences in the order of 200 ns.[3]

Figure A.1 (c) shows y for $\tau = T/4$ and $\alpha = 0.7$. The pulses y_1 and y_2 are 2.5 period pulses with $f_0 = 2.5$ MHz, bandpass filtered to a -6 dB bandwidth of 1.45 MHz. Very little inference is observed in y. In Fig. A.2, the magnitude and phase of the frequency spectrum of y is given. The left column shows the spectrum over a relatively wide band, and the right column shows the spectrum in the -6 dB band. For the phase, a linear fit has been subtracted in order to show the non-linear variations of the phase with frequency. The figure shows that for $\beta = 1/4$ there

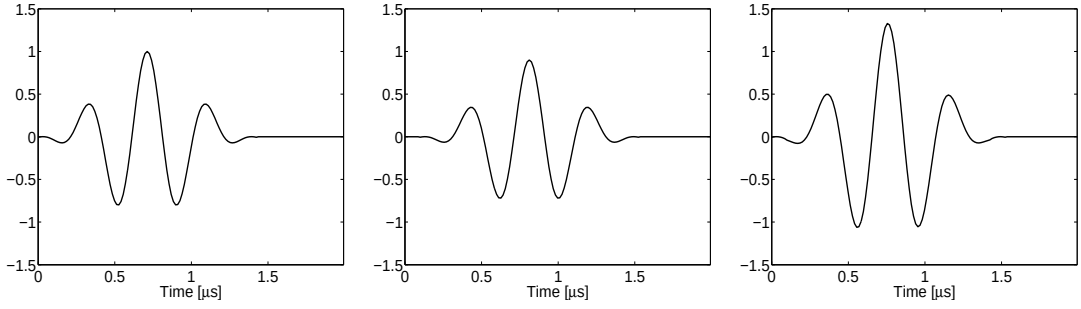

(a) $y_1(t)$ (b) $y_2(t) = \alpha\ y_1(t - T/4)$ (c) $y(t) = y_1(t) + \alpha\ y_1(t - T/4)$

Figure A.1: Pulse with 2.5 MHz center frequency. The time delay between y_1 and y_2 is $T/4$, and $\alpha = 0.7$.

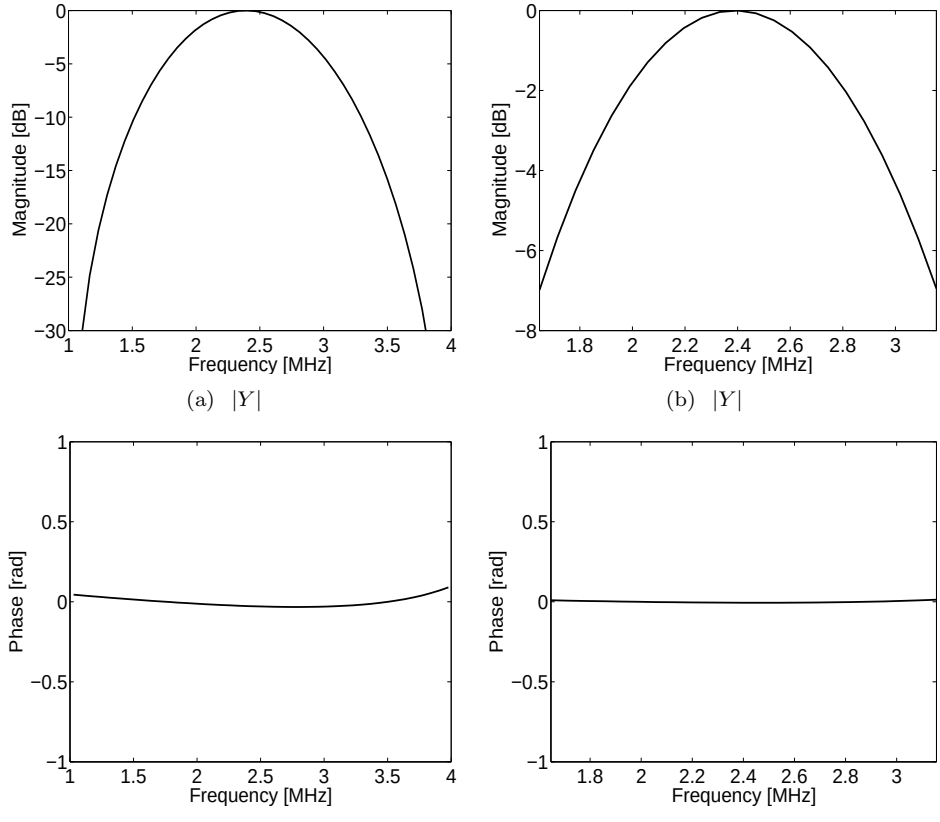

(a) $|Y|$ (b) $|Y|$

(c) $\angle Y$ (d) $\angle Y$

Figure A.2: Magnitude and phase of the Fourier-transform of y. For the phase, a linear fit has been subtracted. The time delay between y_1 and y_2 is $T/4$, and $\alpha = 0.7$. The left column shows the specter in the frequency band from 1-4 MHz. The right column shows the specter within the -6 dB band.

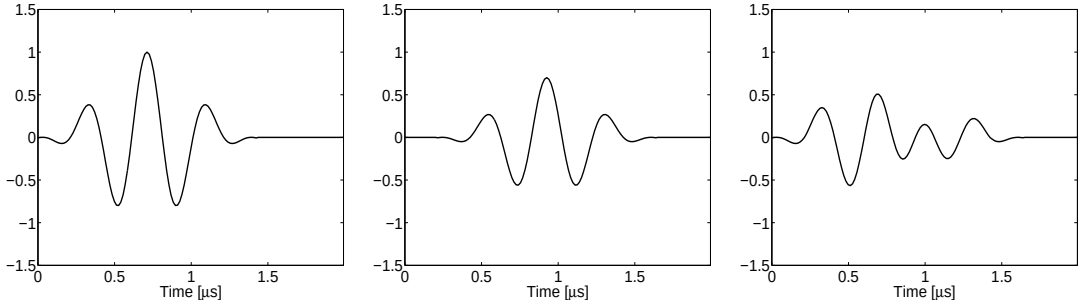

(a) $y_1(t)$ (b) $y_2(t) = \alpha\, y_1(t - T/2)$ (c) $y(t) = y_1(t) + \alpha\, y_1(t - T/2)$

Figure A.3: Pulse with 2.5 MHz center frequency. The time delay between y_1 and y_2 is $T/2$, and $\alpha = 0.7$.

is a very weak non-linear component in the phase. Within the -6 dB bandwidth it is almost not detectable.

In Figs. A.3 and A.4, β is increased to 1/2. Now there is a strong interference in y, there is dramatic change in the spectrum around the center frequency of the pulse giving a highly non-linear phase. Within the -6 dB bandwidth, the maximum deviation in the phase is close to 1 radians.

Figures A.5 and A.6 shows y for $\beta = 3/4$. Here also, the phase is highly non-linear, but in the -6 dB band is approximately linear. There is a shift in the maximum value of the magnitude of the spectrum, and it is now centered around 2.7 MHz.

Reducing or increasing the factor α, reduce or increase the non-linearity of the phase respectively. This is shown in the figures below. For $\alpha = 0.9$, there is a strong non-linearity in the region where the magnitude of the spectrum drops. Inside the -6 dB bandwidth, the phase is approximately linear.

As this simple example show, different values of β produce different non-linear effects of the phase of the signal y. This means that the higher order coefficients in the orthogonal basis will vary with the degree of interference. In addition, the degree of interference yields a different weighting of the phase as the peak of the spectrum is shifted to lower or higher values.

In a real situation, the receive ultrasound signal will be a sum of many signals with time delay differences and different amplitudes, and the effects explained here will then be more complex. Nonetheless, the presented example illustrates some challenges for future research, to understand the relation between frequency and aberration, and how to efficiently correct for it.

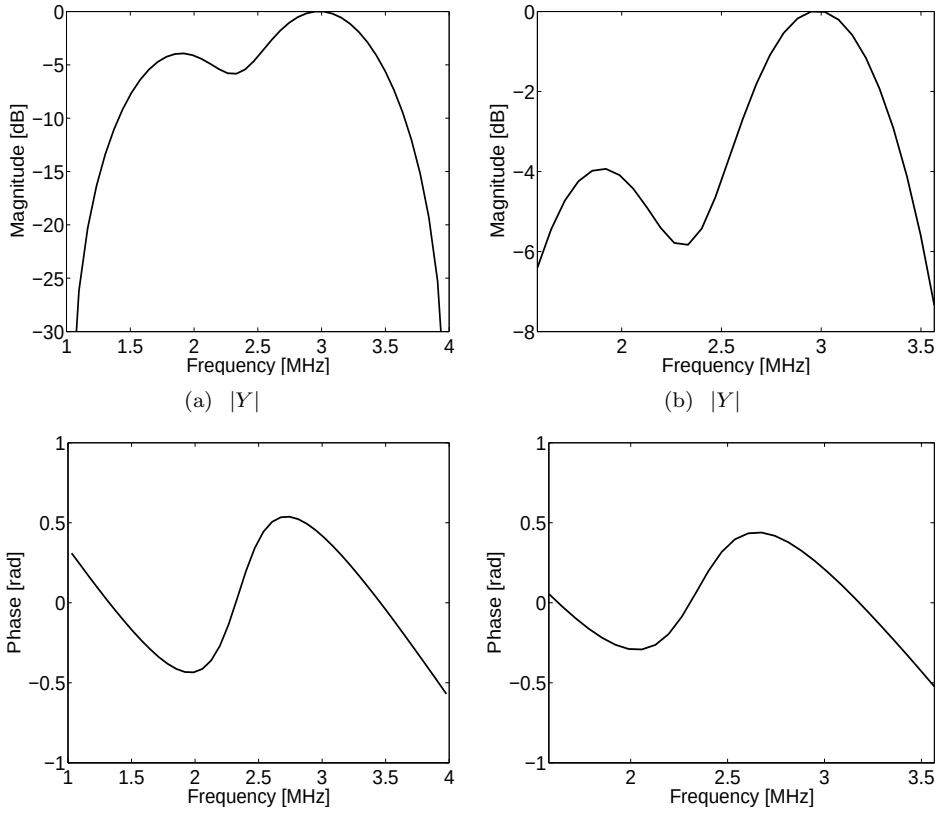

(a) $|Y|$ (b) $|Y|$

(c) $\angle Y$ (d) $\angle Y$

Figure A.4: Magnitude and phase of the Fourier-transform of y. For the phase, a linear fit has been subtracted. The time delay between y_1 and y_2 is $T/2$, and $\alpha = 0.7$. The left column shows the specter in the frequency band from 1-4 MHz. The right column shows the specter within the -6 dB band.

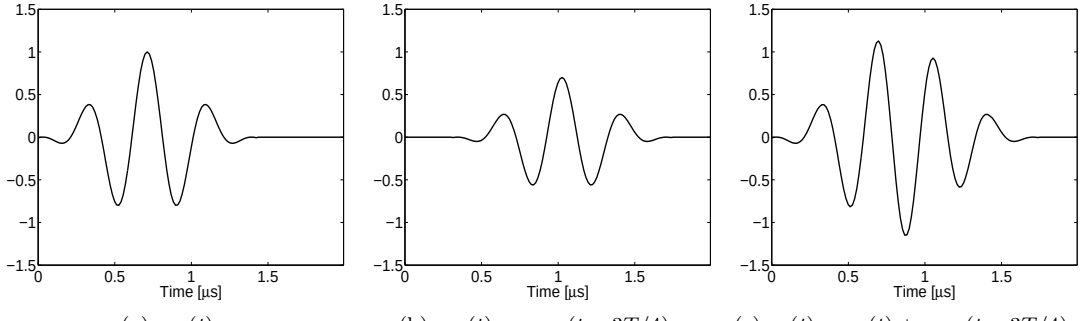

(a) $y_1(t)$ (b) $y_2(t) = \alpha\ y_1(t - 3T/4)$ (c) $y(t) = y_1(t) + \alpha\ y_1(t - 3T/4)$

Figure A.5: Pulse with 2.5 MHz center frequency. The time delay between y_1 and y_2 is $3T/4$, and $\alpha = 0.7$.

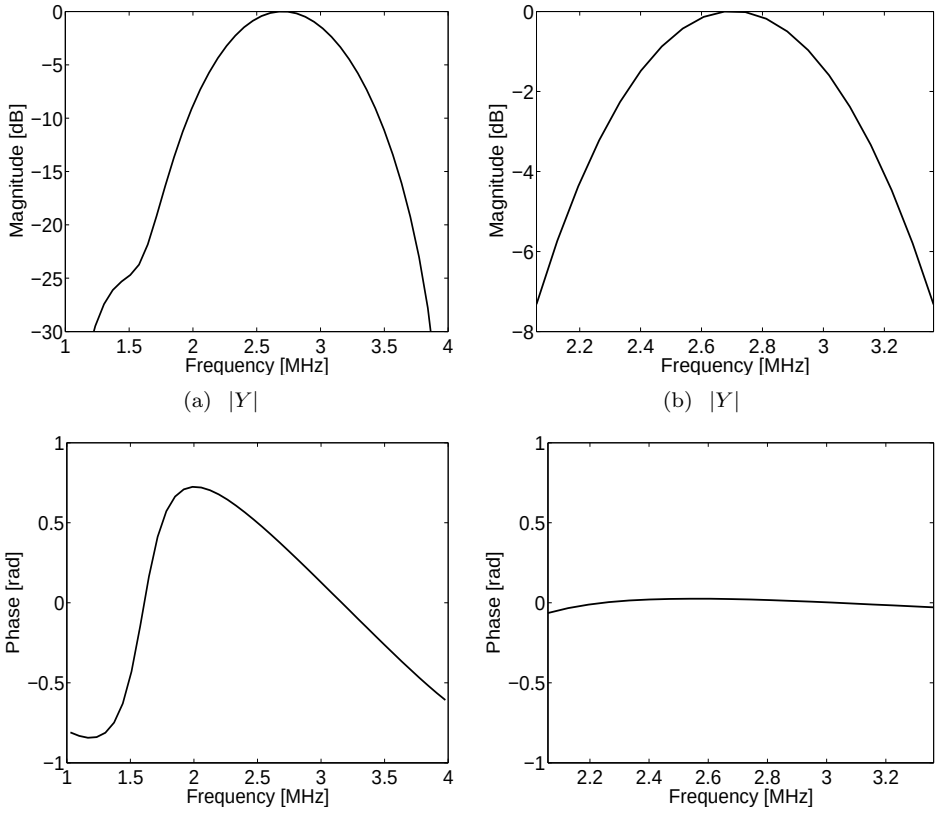

(a) $|Y|$ (b) $|Y|$

(c) $\angle Y$ (d) $\angle Y$

Figure A.6: Magnitude and phase of the Fourier-transform of y. For the phase, a linear fit has been subtracted. The time delay between y_1 and y_2 is $3T/4$, and $\alpha = 0.7$. The left column shows the specter in the frequency band from 1-4 MHz. The right column shows the specter within the -6 dB band.

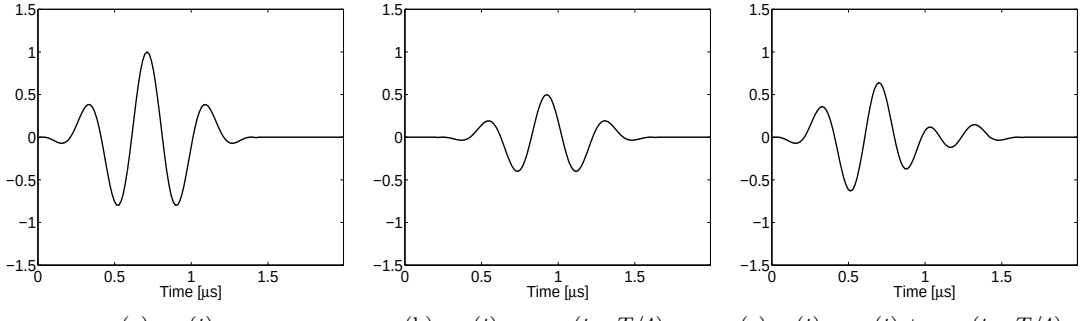

(a) $y_1(t)$ (b) $y_2(t) = \alpha\ y_1(t - T/4)$ (c) $y(t) = y_1(t) + \alpha\ y_1(t - T/4)$

Figure A.7: Pulse with 2.5 MHz center frequency. The time delay between y_1 and y_2 is $T/4$, and $\alpha = 0.5$.

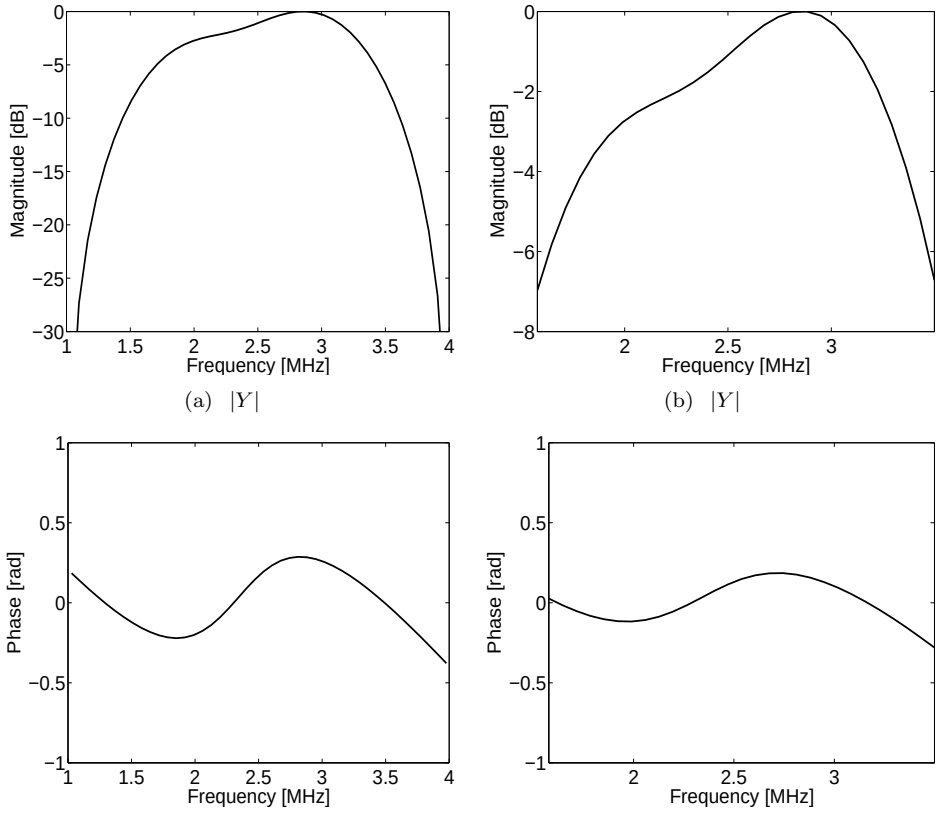

(a) $|Y|$ (b) $|Y|$

(c) $\angle Y$ (d) $\angle Y$

Figure A.8: Magnitude and phase of the Fourier-transform of y. For the phase, a linear fit has been subtracted. The time delay between y_1 and y_2 is $T/2$, and $\alpha = 0.5$. The left column shows the specter in the frequency band from 1-4 MHz. The right column shows the specter within the -6 dB band.

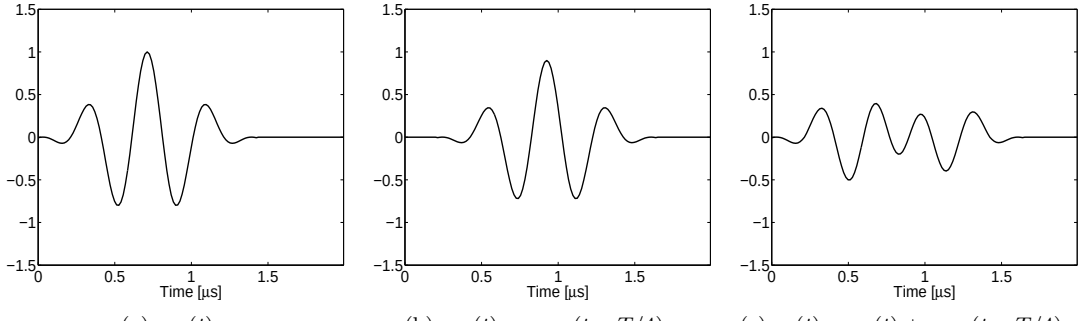

(a) $y_1(t)$ (b) $y_2(t) = \alpha\ y_1(t - T/4)$ (c) $y(t) = y_1(t) + \alpha\ y_1(t - T/4)$

Figure A.9: Pulse with 2.5 MHz center frequency. The time delay between y_1 and y_2 is $T/4$, and $\alpha = 0.9$.

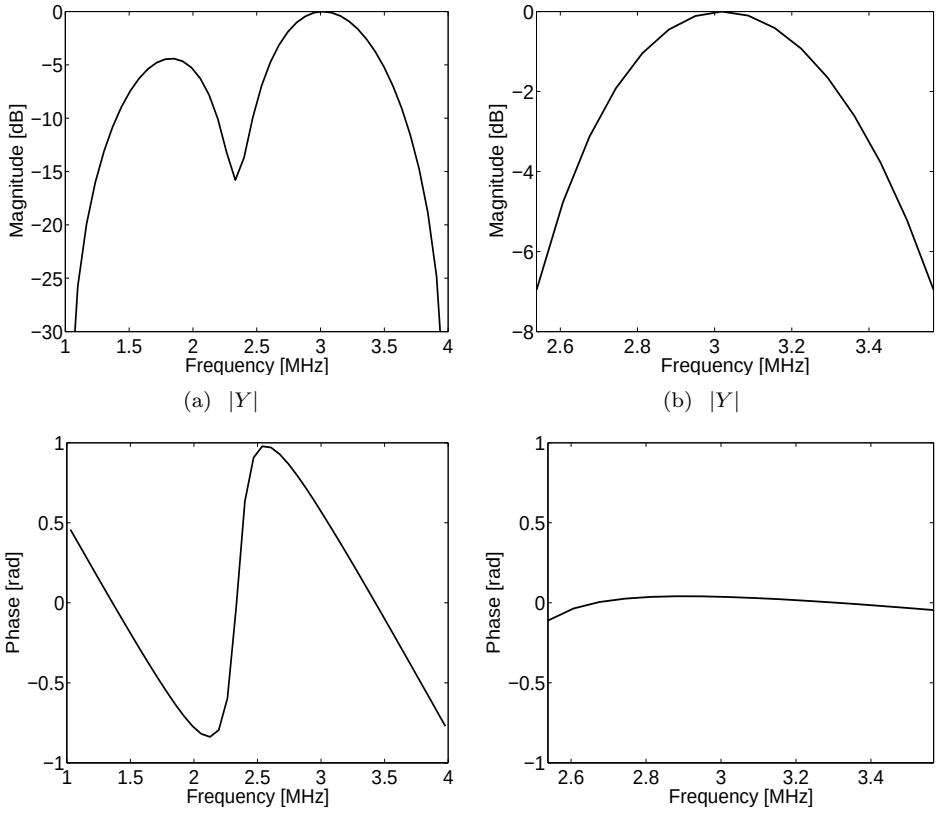

(a) $|Y|$ (b) $|Y|$

(c) $\angle Y$ (d) $\angle Y$

Figure A.10: Magnitude and phase of the Fourier-transform of y. For the phase, a linear fit has been subtracted. The time delay between y_1 and y_2 is $T/2$, and $\alpha = 0.9$. The left column shows the specter in the frequency band from 1-4 MHz. The right column shows the specter within the -6 dB band.

Appendix B

The MBFO estimator in the frequency and time domain: A comparison

In this appendix, a summary of the MBFO estimator in the time and frequency domain implementation is given.

Frequency domain

In the frequency domain implementation of the MBFO algorithm, the receive signal was written as

$$y(\mathbf{r}_a;\omega) = s(\mathbf{r}_a;\omega)\ f(\mathbf{r}_a;\omega)\ , \tag{B.1}$$

where $\mathbf{r}_a$ represents the array coordinate. Here, the generalized frequency dependent screen is given as a frequency dependent amplitude and phase:

$$s(\mathbf{r}_a;\omega) = a(\mathbf{r}_a;\omega)\ e^{i\theta(\mathbf{r}_a;\omega)}\ . \tag{B.2}$$

Writing the receive signal as a function of array element p, dropping frequency dependence for notational convenience gives

$$y_p = s_p f_p\ . \tag{B.3}$$

The definition of the cross-spectrum between element p and n is defined as

$$R_{pn} = \mathrm{E}[y_p\ y_n^*]\ , \tag{B.4}$$

By using the correlation information between all elements on the receiving array, the MBFO algorithm was developed to be

$$\tilde{s}_p = \sum_{n=1}^{N} W_{pn}\ \frac{\tilde{R}_{pn}}{|F_{pn}|}\frac{1}{\tilde{s}_n^*}\ ,\ p = 1,\ldots,N\ . \tag{B.5}$$

The estimate $\tilde{R}_{pn}$ of the cross-spectrum was enhanced by averaging the cross-spectrum over K independent realizations of the received signal. In a general form, this may be written as

$$\tilde{R}_{pn} = \frac{1}{K}\sum_{k=1}^{K}\ y_{kp}\ y_{kn}^*\ , \tag{B.6}$$

where y_{kp} denotes the frequency spectrum of receive signal k.

The coherence is defined as

$$w_{pn} = \frac{R_{pn}}{\sqrt{R_{pp}\ R_{nn}}} \ . \tag{B.7}$$

This gives

$$|w_{pn}| = \frac{|R_{pn}|}{\sqrt{R_{pp}\ R_{nn}}} = \frac{|F_{pn}|}{\sqrt{F_{pp}\ F_{nn}}} \ . \tag{B.8}$$

Based on the above results, the weight function W_{pn} was chosen as

$$W_{pn} = \frac{|w_{pn}|^2}{\sum_{n=1}^{N} |w_{pn}|^2} = \frac{|w_{pn}|^2}{C_p} = \frac{|w_{pn}||F_{pn}|}{C_p} \ , \tag{B.9}$$

where F_{pp} has been set to identity.
Inserted into Eq. (B.5) this finally gives

$$\tilde{s}_p(\omega) = \sum_{n=1}^{N} |\tilde{w}_{pn}(\omega)|\ \tilde{R}_{pn}(\omega) \frac{1}{\tilde{s}_n^*(\omega)} \ , \ p = 1, \ldots, N \ . \tag{B.10}$$

where $\tilde{w}_{pn}$ is an estimate of w_{pn} using $\tilde{R}_{pn}$. The frequency dependence has here been reintroduced.

Time domain

Taking the inverse Fourier transform of Eq. (B.1) gives the time domain receive signal as

$$y(\mathbf{r}_a, t) = \int_{-\infty}^{\infty} s(\mathbf{r}_a, t - \lambda) f(\mathbf{r}_a, \lambda) d\lambda \ , \tag{B.11}$$

Now, approximating the generalized screen as a simple time-delay and amplitude filter on the form

$$s(\mathbf{r}_a, t) \approx a(\mathbf{r}_a)\delta(t - \tau(\mathbf{r}_a)) \ , \tag{B.12}$$

and inserting this into Eq. (B.11), gives

$$y(\mathbf{r}_a, t) = a(\mathbf{r}_a) f(\mathbf{r}_a, t - \tau(\mathbf{r}_a)) \ . \tag{B.13}$$

This approximation assumes a linearly varying phase and a real valued amplitude.
Using the narrow band approximation this filter was given as

$$s(\mathbf{r}_a) = a(\mathbf{r}_a)\ e^{-i\omega\tau(\mathbf{r}_a)} \ . \tag{B.14}$$

The narrow band approximation also lead to a signal model in the same form as in the frequency domain

$$\hat{y}_p = s_p \hat{f}_p \ , \tag{B.15}$$

where the $\hat{y}$ now denotes the complex analytic signal, and time dependence has been omitted. Using these approximations the derivation of the MBFO time domain algorithm is equivalent to the frequency domain derivation and is given as

$$\tilde{s}_p = \sum_{n=1}^{N} W_{pn}\ \frac{\tilde{R}_{pn}}{|F_{pn}|} \frac{1}{\tilde{s}_n^*} \ , \ p = 1, \ldots, N \ . \tag{B.16}$$

The basic difference is in the estimation of the cross-correlation $\tilde{R}_{pn}$. Using the ergodic hypothesis, a non-biased estimate of the cross-correlation at zero lag is defined as

$$\tilde{R}_{pn} = \frac{1}{K} \sum_k \frac{1}{T} \int_T \hat{y}_{kp}(t) \hat{y}^*_{kn}(t) \, \mathrm{d}t \ . \tag{B.17}$$

The correlation coefficient at zero lag is defined as

$$\rho_{pn} = \frac{R_{pn}}{\sqrt{R_{pp} R_{nn}}}, \tag{B.18}$$

which equivalent to Eq. (B.8) yields

$$|\rho_{pn}| = \frac{|R_{pn}|}{\sqrt{R_{pp} R_{nn}}} = \frac{|F_{pn}|}{\sqrt{F_{pp} F_{nn}}}, \tag{B.19}$$

The weight function is now chosen as

$$W_{pn} = \frac{|\rho_{pn}|^2}{\sum_{n=1}^{N} |\rho_{pn}|^2} = \frac{|\rho_{pn}||F_{pn}|}{C_p} \ , \tag{B.20}$$

and the MBFO algorithm in the time domain becomes

$$\tilde{s}_p = \sum_{n=1}^{N} \ |\tilde{\rho}_{pn}| \ \tilde{R}_{pn} \frac{1}{\tilde{s}^*_n} \ , \ p = 1, \ldots, N \ . \tag{B.21}$$

Since all time dependence is integrated, this equation is not dependent on time.
Parseval's theorem states

$$\int_{-\infty}^{\infty} \hat{y}_p(t) \hat{y}^*_n(t) \ dt = \frac{1}{2\pi} \int_{-\infty}^{\infty} \hat{y}_p(\omega) \hat{y}^*_n(\omega) \ \mathrm{d}\omega \ . \tag{B.22}$$

The signal can be assumed to be infinite in time (*e.g.* a windowed part of an infinite signal). Dropping the integration period, and using the result from Parseval's theorem in Eq. (B.17) yields

$$\begin{aligned} \tilde{R}_{pn} &= \frac{1}{K} \sum_k \frac{1}{2\pi} \int_{-\infty}^{\infty} \hat{y}_{kp}(\omega) \hat{y}^*_{kn}(\omega) \ \mathrm{d}\omega \\ &= \frac{1}{2\pi} \int_{-\infty}^{\infty} \frac{1}{K} \sum_k \hat{y}_{kp}(\omega) \hat{y}^*_{kn}(\omega) \ \mathrm{d}\omega \\ &= \frac{1}{2\pi} \int_{-\infty}^{\infty} \tilde{R}_{pn}(\omega) \ \mathrm{d}\omega \ . \end{aligned} \tag{B.23}$$

The time domain implementation uses the integral of the cross-spectrum estimate over all frequency components.

References

[1] T. Varslot, B. Angelsen, and R. C. Waag, "Spectral estimation for characterization of acoustic aberration," *J. Acoust. Soc. Am.*, vol. 116, no. 1, pp. 97–108, July 2004.

[2] L. M. Hinkelman and D.-L. Liu, L. A. Metlay, and R. C. Waag, "Measurements of ultrasonic pulse arrival time and energy level variations produced by propagation through abdominal wall," *J. Acoust. Soc. Am.*, vol. 95, no. 1, pp. 530–541, January 1994.

[3] L. M. Hinkelman and D.-L. Liu, R. C. Waag, and Q. Zhu and B. D. Steinberg, "Measurement and correction of ultrasonic pulse distortion produced by the human breast," *J. Acoust. Soc. Am.*, vol. 97, no. 3, pp. 1958–1969, March 1995.

Bibliography

B. Angelsen. *Ultrasound imaging. Waves, signals and signal processing*, volume I. Emantec, Trondheim, 2000. http://www.ultrasoundbook.com.

B. Angelsen. *Ultrasound imaging. Waves, signals and signal processing*, volume II. Emantec, Trondheim, 2000. http://www.ultrasoundbook.com.

A. P. Berkhoff and J. Thijssen. Correction of concentrated and distributed aberrations in medical ultrasound imaging. *1996 IEEE Ultrasonics Symp. Proc.*, 2:1405–1410, 1996.

W. C. Black and H. G. Welch. Advances in diagnostic imaging and overestimations of disease prevalence and the benefits of therapy. *New England J. Med.*, 328:1237–1243, April 1993.

G. C. Carter. Coherence and time delay estimation. *Proc. IEEE*, 75(2):236–255, 1987.

M. Fink, C. Prada, F. Wu, and D. Cassereau. Self focusing in inhomogeneous media with "Time Reversal" acoustic mirrors. *Ultrasonics Symposium, 1989 Proceedings, IEEE 1989*, pages 681–686, 1989.

S. W. Flax and M. O'Donnell. Phase-aberration correction using signals from point reflectors and diffuse scatterers: Basic principles. *IEEE Trans. Ultrason. Ferroelectr. Freq. Control*, 35(6):758–767, November 1988.

A. Gelet, J. Chapelon, R. Bouvier, O. Rouvière, Y. Lasne, D. Lyonnet, and J. M. Dubernard. Transrectal high-intensity focused ultrasound: Minimally invasive therapy of localized prostate cancer. *Journal of Endourology*, 14(6), August 2000.

L. Hinkelman, T. D. Mast, L. A. Metlay, and R. C. Waag. The effect of abdominal wall morphology on ultrasonic pulse distortion. part i. measurements. *J. Acoust. Soc. Am.*, 104(6):3635–3649, December 1998.

L. M. Hinkelman, T. L. Szabo, and R. C. Waag. Measurements of ultrasonic pulse distortion produced by human chest wall. *J. Acoust. Soc. Am.*, 101(4):2365–2373, April 1997.

M. Karaman, A. Atalar, H. Köymen, and M. O'Donnell. A phase aberration correction method for ultrasound imaging. *IEEE Trans. Ultrason. Ferroelectr. Freq. Control*, 40(4):275–282, July 1993.

E. Kreyzig. *Advanced Engineering Mathematics.* Wiley, Singapore, 8 edition, 1999.

S. Krishnan, P.-C. Li, and M. O'Donnell. Adaptive compensation of phase and magnitude aberrations. *IEEE Trans. Ultrason. Ferroelectr. Freq. Control*, 43(1):44–55, January 1996.

S. Krishnan, K. W. Rigby, and M. O'Donnell. Improved estimation of phase aberration profiles. *IEEE Trans. Ultrason. Ferroelectr. Freq. Control*, 44(3):701–713, May 1997.

S. Krishnan, K. W. Rigby, and M. O'Donnell. Efficient parallel adaptive aberration correction. *IEEE Trans. Ultrason. Ferroelectr. Freq. Control*, 45(3):691–703, May 1998.

L. M. Hinkelman and D.-L. Liu, L. A. Metlay, and R. C. Waag. Measurements of ultrasonic pulse arrival time and energy level variations produced by propagation through abdominal wall. *J. Acoust. Soc. Am.*, 95(1):530–541, January 1994.

L. M. Hinkelman and D.-L. Liu, R. C. Waag, and Q. Zhu and B. D. Steinberg. Measurement and correction of ultrasonic pulse distortion produced by the human breast. *J. Acoust. Soc. Am.*, 97(3):1958–1969, March 1995.

J. C. Lacefield and R. C. Waag. Evaluation of backpropagation methods for transmit focus compensation. *Ultrasonics Symposium, 2001 IEEE*, 2:1495–1498, 2001.

J. C. Lacefield and R. C. Waag. Spatial coherence analysis applied to aberration correction using a two-dimensional array system. *J. Acoust. Soc. Am.*, 112(6):2558–2566, December 2002.

F. Lin and R. C. Waag. Estimation and compensation of ultrasonic wavefront distortion using a blind system identification method. *IEEE Trans. Ultrason. Ferroelectr. Freq. Control*, 49(6):739–755, June 2002.

D.-L. Liu and R. C. Waag. Correction of ultrasonic wavefront distortion using backpropagation and a reference waveform method for time-shift compensation. *J. Acoust. Soc. Am.*, 96(2):649–660, August 1994.

D.-L. Liu and R. C. Waag. Time-shift compensation of ultrasonic pulse focus degradation using least-mean-square error estimates of arrival time. *J. Acoust. Soc. Am.*, 95(1):542–555, January 1994.

R. Mallart and M. Fink. The van Cittert-Zernike theorem in pulse echo measurements. *J. Acoust. Soc. Am.*, 90(5):2718–2727, November 1991.

R. Mallart and M. Fink. Adaptive focusing in scattering media through sound-speed inhomogeneities: The van Cittert Zernike approach and focusing criterion. *J. Acoust. Soc. Am.*, 96(6):3721–3732, December 1994.

S.-E. Måsøy, T. F. Johansen, and B. Angelsen. Correction of ultrasonic wave aberration with a time delay and amplitude filter. *J. Acoust. Soc. Am.*, 113(4):2009–2020, April 2003.

S.-E. Måsøy, T. Varslot, and B. Angelsen. Estimation of ultrasound wave aberration with signals from random scatterers. *J. Acoust. Soc. Am.*, 115(6):2998–3009, June 2004.

T. D. Mast, L. M. Hinkelman, M. J. Orr, and R. C. Waag. The effect of abdominal wall morphology on ultrasonic pulse distortion. part ii. simulations. *J. Acoust. Soc. Am.*, 104(6):3651–3664, December 1998.

T. K. Moon and W. C. Stirling. *Mathematical Methods and Algorithms for Signal Processing.* Prentice Hall, Upper Saddle River, New Jersey 07458, 2000.

G. C. Ng, S. S. Worrel, P. D. Freiburger, and G. E. Trahey. A comparative evaluation of several algorithms for phase aberration correction. *IEEE Trans. Ultrason. Ferroelectr. Freq. Control*, 41(5):631–643, September 1994.

L. F. Nock, G. E. Trahey, and S. W. Smith. Phase aberration correction in medical ultrasound using speckle brightness as an image quality factor. *J. Acoust. Soc. Am.*, 85(5):1819–1833, May 1989.

L. A. Ødegaard. Using signals scattered from diffuse inhomogeneities to correct for phase aberrations caused by a phase-screen far from the transducer. *IEEE Ultrasonics Symp. Proc.*, 2:1443–1447, 1995.

M. O'Donnell and W. E. Engeler. Real-time phase aberration correction system for medical ultrasound imaging. *Annual International Conference of the IEEE Engineering in Medicine and Biology Society*, 12, 1990.

M. O'Donnell and S. W. Flax. Phase-aberration correction using signals from point reflectors and diffuse scatterers: Measurements. *IEEE Trans. Ultrason. Ferroelectr. Freq. Control*, 35(6):768–774, November 1988.

M. Pernot, J.-F. Aubry, M. Tanter, M. Fink, A.-L. Boch, and M. Kujas. Ultrasonic brain therapy: First trans-skull in vivo experiments on sheep using adaptive focusing. *J. Acoust. Soc. Am.*, 115:2524, 2004.

M. B. Priestley. *Spectral Analysis and Time Series.* Academic Press, 1988.

K. W. Rigby, C. L. Chalek, B. H. Haider, R. S. Lewandowski, M. O'Donnell, L. S. Smith, and D. G. Wildes. Improved in vivo abdominal image quality using real-time estimation and correction of wavefront arrival time errors. *IEEE Ultrasonics Symposium*, 2:1645–1653, October 2000.

S.-E. Måsøy and T. Varslot and B. Angelsen. Iteration of transmit-beam aberration correction in medical ultrasound imaging. Accepted for publication in JASA, 2004.

S. D. Silverstein and D. P. Ceperley. Autofocusing in medical ultrasound: The scaled covariance matrix algorithm. *IEEE Trans. Ultrason. Ferroelectr. Freq. Control*, 50(7):795–804, July 2003.

T. Douglas Mast, Laura M. Hinkelman, and Michael J. Orr, V. W. Sparrow, and R. C. Waag. Simulation of ultrasonic pulse propagation through the abdominal wall. *J. Acoust. Soc. Am.*, 102(2):1177–1190, August 1997.

M. Tanter, J.-L. Thomas, and M. Fink. Time reversal and the inverse filter. *J. Acoust. Soc. Am.*, 108(1):223–234, July 2000.

T. Varslot, B. Angelsen, and R. C. Waag. Spectral estimation for characterization of acoustic aberration. *J. Acoust. Soc. Am.*, 116(1):97–108, July 2004.

T. Varslot, E. Mo, H. Krogstad, and B. Angelsen. Eigenfunction analysis of stochastic backscatter for characterization of acoustic aberration in medical ultrasound imaging. *J. Acoust. Soc. Am.*, 115(6):3068–3076, June 2004.

F. Viola and W. F. Walker. A comparison of the performance of time-delay estimators in medical ultrasound. *IEEE Trans. Ultrason. Ferroelectr. Freq. Control*, 50(4):392–401, April 2003.

W. F. Walker and G. E. Trahey. A fundamental limit on the performance of correlation based phase correction and flow estimation techniques. *IEEE Trans. Ultrason. Ferroelectr. Freq. Control*, 41(5):644–654, September 1994.

W. F. Walker and G. E. Trahey. A fundamental limit on delay estimation using partially correlated speckle signals. *IEEE Trans. Ultrason. Ferroelectr. Freq. Control*, 42(2):301–308, March 1995.

W. F. Walker and G. E. Trahey. Aberrator integration error in adaptive imaging. *IEEE Trans. Ultrason. Ferroelectr. Freq. Control*, 44(4):780–791, July 1997.

P.-H. Zahl, B. Heine, and J. Mæhle. Incidence of breast cancer in norway and sweden during introduction of nationwide screening: prospective cohort study. *British Medical Journal*, 328:921–924, April 2004.

Q. Zhu and B. Steinberg. Deaberration of incoherent wavefront distortion: An approach toward inverse filtering. *IEEE Trans. Ultrason. Ferroelectr. Freq. Control*, 44(3):575–589, May 1997.